IAEA-TECDOC-1676

Role of Nuclear Based Techniques in Development and Characterization of Materials for Hydrogen Storage and Fuel Cells

IAEA
International Atomic Energy Agency

Role of Nuclear Based Techniques in Development and Characterization of Materials for Hydrogen Storage and Fuel Cells

The following States are Members of the International Atomic Energy Agency:

AFGHANISTAN
ALBANIA
ALGERIA
ANGOLA
ARGENTINA
ARMENIA
AUSTRALIA
AUSTRIA
AZERBAIJAN
BAHRAIN
BANGLADESH
BELARUS
BELGIUM
BELIZE
BENIN
BOLIVIA
BOSNIA AND HERZEGOVINA
BOTSWANA
BRAZIL
BULGARIA
BURKINA FASO
BURUNDI
CAMBODIA
CAMEROON
CANADA
CENTRAL AFRICAN REPUBLIC
CHAD
CHILE
CHINA
COLOMBIA
CONGO
COSTA RICA
CÔTE D'IVOIRE
CROATIA
CUBA
CYPRUS
CZECH REPUBLIC
DEMOCRATIC REPUBLIC OF THE CONGO
DENMARK
DOMINICA
DOMINICAN REPUBLIC
ECUADOR
EGYPT
EL SALVADOR
ERITREA
ESTONIA
ETHIOPIA
FINLAND
FRANCE
GABON
GEORGIA
GERMANY
GHANA
GREECE
GUATEMALA
HAITI
HOLY SEE
HONDURAS
HUNGARY
ICELAND
INDIA
INDONESIA
IRAN, ISLAMIC REPUBLIC OF
IRAQ
IRELAND
ISRAEL
ITALY
JAMAICA
JAPAN
JORDAN
KAZAKHSTAN
KENYA
KOREA, REPUBLIC OF
KUWAIT
KYRGYZSTAN
LAO PEOPLE'S DEMOCRATIC REPUBLIC
LATVIA
LEBANON
LESOTHO
LIBERIA
LIBYA
LIECHTENSTEIN
LITHUANIA
LUXEMBOURG
MADAGASCAR
MALAWI
MALAYSIA
MALI
MALTA
MARSHALL ISLANDS
MAURITANIA
MAURITIUS
MEXICO
MONACO
MONGOLIA
MONTENEGRO
MOROCCO
MOZAMBIQUE
MYANMAR
NAMIBIA
NEPAL
NETHERLANDS
NEW ZEALAND
NICARAGUA
NIGER
NIGERIA
NORWAY
OMAN
PAKISTAN
PALAU
PANAMA
PARAGUAY
PERU
PHILIPPINES
POLAND
PORTUGAL
QATAR
REPUBLIC OF MOLDOVA
ROMANIA
RUSSIAN FEDERATION
SAUDI ARABIA
SENEGAL
SERBIA
SEYCHELLES
SIERRA LEONE
SINGAPORE
SLOVAKIA
SLOVENIA
SOUTH AFRICA
SPAIN
SRI LANKA
SUDAN
SWEDEN
SWITZERLAND
SYRIAN ARAB REPUBLIC
TAJIKISTAN
THAILAND
THE FORMER YUGOSLAV REPUBLIC OF MACEDONIA
TUNISIA
TURKEY
UGANDA
UKRAINE
UNITED ARAB EMIRATES
UNITED KINGDOM OF GREAT BRITAIN AND NORTHERN IRELAND
UNITED REPUBLIC OF TANZANIA
UNITED STATES OF AMERICA
URUGUAY
UZBEKISTAN
VENEZUELA
VIETNAM
YEMEN
ZAMBIA
ZIMBABWE

The Agency's Statute was approved on 23 October 1956 by the Conference on the Statute of the IAEA held at United Nations Headquarters, New York; it entered into force on 29 July 1957. The Headquarters of the Agency are situated in Vienna. Its principal objective is "to accelerate and enlarge the contribution of atomic energy to peace, health and prosperity throughout the world''.

IAEA-TECDOC-1676

ROLE OF NUCLEAR BASED TECHNIQUES IN DEVELOPMENT AND CHARACTERIZATION OF MATERIALS FOR HYDROGEN STORAGE AND FUEL CELLS

INTERNATIONAL ATOMIC ENERGY AGENCY
VIENNA, 2012

For further information on this publication, please contact:

Physics Section
International Atomic Energy Agency
Vienna International Centre
PO Box 100
1400 Vienna, Austria
email: Official.Mail@iaea.org

Printed by the IAEA in Austria
February 2012

IAEA Library Cataloguing in Publication Data

Role of nuclear based techniques in development and characterization of materials for hydrogen storage and fuel cells. – Vienna : International Atomic Energy Agency, 2012.
p. ; 30 cm. – (IAEA-TECDOC series, ISSN 1011-4289 ; no. 1676)
ISBN 978-92-0-125410-8
Includes bibliographical references.

1. Nuclear physics – Research. 2. Hydrogen as fuel. – 3. Hydrogen - Storage. 4. Fuel cells. I. International Atomic Energy Agency. II. Series.

IAEAL 12-00725

FOREWORD

Hydrogen and fuel cells can greatly contribute to a more sustainable less carbon-dependent global energy system. The major components in a hydrogen economy are expected to include production, storage, transportation and conversion of hydrogen, e.g. in fuel cells. All these components present considerable technological challenges, in particular as they relate to materials development. The research efforts required to solve these challenges will need new materials and solutions, and not simply, incremental improvements of current technologies.

Nuclear methods are poised to play an important role in the improvement and development of materials by providing a major tool with which to characterize their properties and performance. A consultants meeting on application of 'Role of Nuclear Techniques in Development of Materials for Hydrogen Storage and Fuel Cells' was held by the International Atomic Energy Agency (IAEA) in Vienna, Austria, on 14-16 May 2008. The usefulness and importance of nuclear techniques to support materials oriented R&D for hydrogen storage in solid state materials and its conversion in fuel cells was recognised.

Two technical meetings on 'Role of Nuclear-based Techniques in Development of Materials for Hydrogen Storage and Fuel Cells were organized by the IAEA. The first was hosted by the International Energy Agency (IEA) in Paris, France, on 16–20 March 2009 and the second by University Trois-Rivières Quebec (UTRQ), Canada, from 23 to 26 August 2010. The meetings participants discussed the broad spectrum of nuclear techniques that can be effectively used for characterization of materials for hydrogen storage and conversion technologies.

This publication summarizes the outputs of the above meetings and selected contributions of the participants. The manuscript could be used by researchers planning to utilize nuclear techniques for the development of hydrogen storage and fuel cell materials. It also aims to disseminate knowledge and information to material scientists, physicists and chemists working towards characterizing and developing new materials.

The IAEA wishes to thank the participants for their contributions. An additional acknowledgment for the experts who helped to review this manuscript, specifically, S. Barroso from the Atomic Energy Research Institute (AEKI), Hungary, M. Steen from Joint Research Centre of European Commission, The Netherlands, J. Huot from Université du Québec à Trois-Rivières, Canada and S. Skinner from Imperial College London, United Kingdom. The IAEA officers responsible for this publication were A. Zeman and P. Salame of the Division of Physical and Chemical Sciences.

EDITORIAL NOTE

The papers in these proceedings are reproduced as submitted by the authors and have not undergone rigorous editorial review by the IAEA.

The views expressed do not necessarily reflect those of the IAEA, the governments of the nominating Member States or the nominating organizations.

The use of particular designations of countries or territories does not imply any judgement by the publisher, the IAEA, as to the legal status of such countries or territories, of their authorities and institutions or of the delimitation of their boundaries.

The mention of names of specific companies or products (whether or not indicated as registered) does not imply any intention to infringe proprietary rights, nor should it be construed as an endorsement or recommendation on the part of the IAEA.

The authors are responsible for having obtained the necessary permission for the IAEA to reproduce, translate or use material from sources already protected by copyrights.

CONTENTS

1. SUMMARY OF CONTRIBUTIONS

Today various materials for fuel cell applications are urgently needed, including potential electrodes for the molten carbonate fuel cells. Identification of appropriate storage concepts are also urgently needed in order to initiate necessary steps for implementation of such technologies in daily life. Recent progress in nuclear analyses and observation/imaging techniques can significantly contribute to a successful achievement of ongoing research challenges. Primary importance is given to areas of characterization and *in-situ* testing of materials and/or components of hydrogen storage and fuel cell systems. Dedicated attention is addressed to issues related to hydrogen storage concepts, such as metal hydrides and other systems(e.g. fullerene structures) as well as their stability and the changes induced by hydrogen sorption process.

In total 14 papers report on various scientific and research issues related to hydrogen storage and conversion technologies. Based on presented results, it can be concluded that nuclear-based techniques, specifically those involving neutrons, X rays and particle beams, play very important roles in ongoing research activities among many IAEA Member States. A short overview of individual reports is summarized below. The presented papers give an overview of typical applications of such techniques and their experimental setups based either on X ray or neutron sources, which can be used effectively to study specific properties of materials for hydrogen storage as well as microstructural features and hydrogen interaction with solid matter. The papers presented by Canadian, Dutch, Italian and Norwegian groups, report on research results related to application of thermal neutron scattering and neutron diffraction in studies of hydrogen containing materials, particularly *in situ* characterization as a means to study metal hydrides' structure and their modification upon hydrogen sorption. The investigation on solid state hydrogen storage materials studied by a combination of complementary methods was presented by a team from the Joint Research Centre of European Commission, which was in charge of coordination work among various research groups from France, Germany and the United Kingdom. They reported effective combination of neutron, X ray and other analytical nuclear techniques as well as a brief comparison of the advantages and limitations of individual methods. Special emphasis was given to characterization of the microstructural changes and thin films made by available nuclear methods, such as positron annihilation spectroscopy and neutron reflectometry. The following report by Chinese researchers, gave a short update on hydrogen absorption properties of lanthanum and zirconium- based hydrogen storage materials. Argentinean and Croatian scientists reported on the degradation of a PEM, fuel cell, platinum-based catalyst by PIXE and application of ERDA methods for imaging of hydrogen-implanted silicon, respectively. The investigation of irradiation effects on oxygen, water and CO_2 desorption, and the identification of phase-transformation behavior on increasing temperature were also discussed. A short overview of structural transformations in Fullerite C_{60} due to hydrogenation was reported by Ukrainian researchers. Finally, the study of proton conductors, irradiated by neutrons was presented by the Kazakhstani research team. Briefly discussed was the problem of proton conducting ceramics and the hydrogen concentration profile using ion beam analysis to probe the relationship between microstructure and hydrogen diffusion.

Generally, this publication aims to contribute to the dissemination of information regarding practical application of nuclear based techniques in research related to R & D initiatives on hydrogen based energy systems, in particular conversion and storage technologies.

2. INTRODUCTION

Significant challenges remain to be overcome if deployment is to be achieved of an economy with hydrogen as energy vector and fuel cells as highly efficient energy converters for stationary and transport applications. These challenges largely relate to optimizing the inclusion of different production, storage, transportation and conversion technologies in an efficient integrated chain from source to end use and to reduce costs for investments, operation and maintenance. It is widely accepted that incremental improvement of existing technologies will not be able to provide the required progress, and that innovative technologies are needed.

The use of hydrogen coupled with fuel cells offers considerable advantages in terms of the reduction of CO_2 emissions, security of supply and access to energy for all people. This particularly applies to hydrogen produced from renewable energy sources. Because of this characteristic, efforts have been deployed world-wide to support the transition of the current mostly fossil fuel-based, centralized energy system into one based on renewable energy sources, where hydrogen and electricity are complementary energy carriers for both centralized and distributed generation systems.

Hydrogen gas (H_2) does not naturally occur in significant quantities, consequently for its use as an energy carrier or other purposes it must first be extracted from a primary source. Today, hydrogen can be obtained using electrical energy (via water electrolysis) generated from hydroelectric, geothermal and photovoltaic sources as well as from fossil fuel and nuclear power plants. Fuel cells are electrochemical devices in which hydrogen (in some cases hydrogen containing compounds) and oxygen are converted with high efficiency, into electricity, producing water and heat as by-products. The electricity produced can be used directly (stationary applications) or converted into motion (transport applications). When hydrogen feedstock is produced from renewable sources, an emission-free and truly environmentally sustainable energy system is obtained that is based on the closed H_2-H_2O cycle, as opposed to the open C-CO_2 cycle. In addition to the clear environmental benefits, hydrogen and fuel cells can also contribute significantly to energy supply security through both diversification (hydrogen can be produced from a variety of primary energy sources that are not concentrated in a limited number of specific regions) and enhanced conversion efficiency.

Nuclear technologies and methods will continue to contribute towards the transition to an increasingly hydrogen-based energy system in two main areas: (i) hydrogen production from nuclear assisted thermal/chemical dissociation of water and (ii) contribution of nuclear methods and techniques to improve understanding and allow subsequent tailoring of materials to better meet the requirements for hydrogen storage and conversion. Conventional non-nuclear methods do not provide accurate and/or direct information about light elements. Therefore nuclear methods are crucial for the development and better understanding of materials for fuel cell and hydrogen cycle technologies. They are very effective tools for the characterization of structural parameters that have direct impact on the performance of the materials (position of light atoms in a lattice, particularly hydrogen atoms, their concentration, dynamics and interaction with other structural components). A significant benefit of these techniques is the ability to perform in situ characterization as a function of temperature, partial pressure, etc., thus providing direct information regarding device operation. The sheer scale of the scientific challenges in this sector is overwhelming. The list of the potential applications is diverse and includes nanomaterials, materials for catalysis and hydrogen storage, ceramic electrodes and the efficient and economic conversion of fuels to energy. In

addition, combinations of diverse experimental techniques very often including nuclear methods, X ray scattering and spectroscopy; sometimes in association with advanced theoretical modelling (for example by use of density functional theory). Such multi-pronged approaches are key to the investigation and characterization of promising materials under consideration for a hydrogen based economy.

2.1 Challenges in hydrogen storage and conversion

All aspects related to the development of a hydrogen economy face considerable technological challenges, in particular as they relate to the development of effective materials for hydrogen storage and fuel cells. Nuclear methods will continue to have an important role related to the development of new/improved materials, but most importantly as a major tool to characterize the properties and performance of these materials. Both hydrogen storage and fuel cell technology have their own particular challenges, as discussed below.

2.2. Hydrogen storage

Hydrogen storage remains an undisputed problem, particularly for mobile applications and is considered by many to be the most technologically challenging aspect of achieving a hydrogen-based economy. For practical applications a transport storage system should fulfil several requirements including, but not limited to high gravimetric and volumetric densities, appropriate thermodynamics (release of hydrogen at relatively low temperatures), good kinetics, acceptable safety, low cost.

Many forms of hydrogen storage have been proposed but practically the main competitors are compressed hydrogen, liquefied hydrogen and storage in solid compounds. Compressed and liquefied hydrogen will never have acceptable performance for most practical applications. The main problems for these systems are the energy consumption involved in liquefaction and compression, and low volumetric and gravimetric densities (the latter points being most relevant for compressed hydrogen). One acceptable long term solution for transport applications is hydrogen storage in solid compounds. Recently a number of new promising hydrogen storage materials have been identified, although there are none that currently meet all the requirements for most practical applications. Materials development has addressed both metal hydrides, in which hydrogen atoms are bonded to the metals by chemical bonding, and nanoporous materials, in which H_2 molecules adsorb on the surfaces. Among the metal hydrides under investigation in particular compounds based on; aluminium (alanates and AlH_3), nitrogen (amides/imides), boron (borohydrides), magnesium, low temperature hydrides ($LaNi_5$, BCC), and mixtures of several compounds in so-called ‘destabilized’ systems (MgH_2 + $LiBH_4$). Promising nanoporous materials include carbon-based compounds with metal catalysts and microporous organic-inorganic framework materials (MOFs), and more recently hydrogen storage in clathrates and polymers has also been studied.

The main challenges are the following:

- Total weight of the system, meaning that the hydrogen storage materials should be based on light-weight elements;
- Thermodynamics of the hydrogen uptake/release process (the temperature for release of hydrogen should match the working temperature for the energy conversion system, for example a polymer electrolyte membrane (PEM) fuel cell);
- Kinetics of the hydrogen uptake/release. This involves new and/or optimized catalysts;
- Cost reduction of raw elements and synthesis techniques of alloys and their hydrides.

A detailed understanding of the materials and storage processes is of the utmost importance for future progress. The use of advanced nuclear characterization tools, including in situ experiments, will be crucial.

2.3. Fuel cells

Fuel cells convert the chemical energy contained within a fuel into electricity and heat. In this process a hydrogen fuel is oxidized to produce protons at the anode, liberating electrons. At the opposite electrode, the cathode, oxygen is reduced. The electrodes are typically electronic conductors, permeable to the reacting gases and are separated from each other by an electrolyte (ionic conductor). The electrolyte can be a liquid, a polymer (generally saturated by a liquid) or a solid.

Electrode reactions in fuel cells primarily involve the breaking of chemical bonds between hydrogen and oxygen atoms. The anode and cathode reactions are heterogeneous and occur at the electrode/electrolyte interface and are catalyzed at the electrode surface. More highly specific catalysts are needed to reduce the energy and material losses that result from parasitic corrosive reactions. The choice of the electrocatalyic system is strongly dependent on the fuel. The type of fuel may also impact on other parameters such as fuel cell lifetime, material corrosion and contaminant production. The most commonly used fuels, besides hydrogen, include natural gas, methanol and ethanol.

The basic fuel cell types span a wide range of operating temperatures, construction materials, and performance specifications, related to the three main application areas: stationary generation, transportation and portable power.

In low-temperature cells (40 to 200°C), polymer electrolyte membrane (PEMFC), direct methanol (DMFC) and phosphoric acid (PAFC), the reactions occur in the gas diffusion layers that consist of an electron-conducting porous structure of the electrode/electrocatalyst system containing platinum and platinum-based alloys. The design of the electrodes should maximize the gas-liquid-solid three-phase interface and therefore considerably increase the electrode process kinetics. For anodic processes, current research activities involve the development of more active and specific electrocatalyic systems both for direct oxidation of alcohols (methanol and ethanol) and hydrogen contaminated by CO. For cathodic processes, where oxygen is reduced, lower cost reduction catalaysts are sought. Finally, there is the development of new electrolytes that permit the operation of these cells above 100°C. Underpinning all of these developments is the requirement to increase cell efficiency and durability (mechanical stability) whilst optimizing the system engineering and reducing costs. In polymer based cells, water management is an important issue in which the development of new in situ nuclear measurement methods will contribute to increased understanding of water distribution issues, thereby assisting with the design of new materials.

The concept of intermediate temperature fuel cells, operating in the 200 to 800 ºC range, is very promising. Research in this area is directed towards reducing the amount of noble- metal catalysts without compromising efficiency. In this case there are two possibilities: raising the temperature in polymer based systems or reducing the operating temperature in ceramic based systems. Each of these possibilities present unique challenges, with the high temperature polymer systems remaining in the early stages of development.

In the high temperature regime (600 to 1000°C) there are two potential technologies: molten carbonate (MCFC) and solid oxide (SOFC), both of which eliminate the need for noble metals

catalysts, In this temperature range the electrode materials are sufficiently active redox catalysts. Development of these cells is focussed on new materials that will allow a decreased operating temperature without sacrificing performance, particularly at the oxygen reduction cathode. Current key research targets include materials that exhibit resilience to thermal cycling, enhanced durability and resistance to corrosion over all temperature ranges.

In addition to the electrochemical performance of fuel cells, their durability is also of major importance. Ageing effects may not only arise due to the intrinsic changes in the properties of materials, but may also be caused by inhomogeneous media distribution across the active area of the fuel cells and stacks. For example, poor water management in PEM fuel cells may lead to enhanced local aging. Furthermore, there is evidence in the literature, that inactive areas may cause high local currents, which are detrimental to the catalysts. Additionally, engineering challenges in the design of electrode assemblies and plant integration are common to all types of fuel cells.

2.4 Overview of applicable nuclear methods

2.4.1. Benefits of nuclear methods

Important properties of nuclear methods/neutrons for studying materials related to fuel cells and the hydrogen cycle are:

- Unlike scattering using X rays or electrons, neutron scattering from light elements such as hydrogen may be similar to that seen from heavier elements. As a result neutron scattering is uniquely able to directly determine hydrogen and light-atom positions and their dynamics. in crystal structures.

- Because of the significant difference in scattering cross-section between hydrogen and deuterium, isotope substitution can be used to provide additional insight into the structure of materials and their interaction with hydrogen.

- The absorption of neutrons is low in most materials. Usually this makes it easier to conduct in-situ experiments using neutron scattering in comparison with other sources such as X rays and electrons. Moreover in some cases neutron scattering is the only technique available for in situ structural measurements.

Important nuclear methods for the study of materials related to fuel cell and hydrogen cycle technologies are outlined in Table 1.

2.4.2. Application of in situ techniques

It is extremely important to be able to study hydrogen storage and fuel cells materials under real working conditions. This is often a challenge because of the complicated sample environments sometimes needed on the neutron beam line to realize the experiment.. *In situ* studies of hydrogen storage materials include hydrogenation/dehydrogenation cycling and experiments as a function of external parameters, such as temperature and pressure. Time resolved *in situ* methods can contribute to monitoring and understanding functional and mechanical degradation of nanomaterials and structures as well as the study the particles sizes and their surfaces in nanoconfined systems.

TABLE 1. OVERVIEW OF NUCLEAR TECHNIQUES AND THEIR APPLICATIONS IN STUDIES OF FUEL CELLS AND HYDROGEN STORAGE MATERIALS

Nuclear technique	Fuel cells	Hydrogen storage
Neutron diffraction (ND)	Crystal structure determination, molten carbonates, including $LiCoO_2$, solid oxides (Ni-Zr,Y).	Crystal structure determination.
Small-angle neutron and X ray scattering (SANS and SAXS)	Gas diffusion electrodes, Structure of ionomer membrane and suspensions (ex-situ), Ni electrode microporosity, metallic cluster distribution in PEFC.	Size/shape morphology and surfaces of nanoparticles and nanopores (e.g. nanostructured Mg hydrides),
Inelastic neutron scattering (INS)	Gas diffusion electrodes and catalyst characterization	Phonons states, hydrogen dynamics
Quasi-elastic neutron scattering (QENS).	Gas diffusion electrodes, Dynamic of water/protons within ionomer.	Hydrogen diffusion and librations.
Neutron reflectivity measurements.	Hydrogen profile in thin films, Swelling properties of thin ionomer films.	Hydrogen profile in thin films
Neutron radiography methods and tomography.	2D and 3D water and gas distribution in fuel cells and stacks	Hydrogen distribution
Total scattering experiments	Local structure determination	Local structure determination
Positron annihilation spectroscopy	Defects of structures and vacancies in HT fuel cell materials	Defects of structures and vacancies
Muon spin rotation (μSR).	Hydrogen dynamics	Hydrogen dynamics
Prompt Gamma Activation Analysis (PGAA)	Determination of trace elements	Determination of trace elements
X ray diffraction (XRD)	Crystal structure determination	Crystal structure determination
Synchrotron radiography and tomography.	Local transport and distribution in gas diffusion electrodes	Dynamics of hydrogenation
Nuclear magnetic spin resonance (NMR)	Water profile in fuel cells and structural analysis	Hydrogen mobility and diffusion, structural analysis
Mössbauer spectroscopy (MS)	Local structure	Local structure
Ion beam analysis	2D and 3D hydrogen and electro catalyst (platinum and other noble metals) profile studies	Hydrogen stoichiometry, elemental profiling in thin films

2.4.3. Sources of neutron and particle beams.

New neutron sources such as accelerator driven systems with nuclear transmutation or nuclear spallation and laser driven systems with nuclear fusion or beam acceleration by ultra-intense lasers are expected to open new avenues in material research for fuel cell technologies. Because of their specifics, such as higher fluxes and short pulses, these new sources could offer higher resolution diagnostics in time and space. This will require developments in image analysis and treatments, such as correlation measurements, high resolution imaging and tomography.

It is important to note that in many cases there is a problem with the availability of beam time at high-flux neutron sources. Many important experiments can be performed using existing sources and even low-flux neutron sources that at present are not being used. Therefore it is important to promote the access to these facilities in order to improve the availability of

experimental opportunities for probing materials relevant to fuel cell and hydrogen-cycle technologies.

2.4.4. Use of ion beam analysis

Methods of ion beam analysis are suitable for the characterization of hydrogen in storage materials or other elements in fuel cell materials, specifically proton induced X ray Emission (PIXE) which can be used for the characterization of the dissolution and reprecipitation of Pt and other metals in the ionomeric membrane of PEM fuel cells (2D mapping). Furthermore, time-of-flight (ToF), particularly elastic recoil detection analysis (ERDA), Rutherford backscattering spectroscopy (RBS) and scanning transmission ion microscopy (STIM). can be used to determine the depth and density distributions of fuel cell components and hydrogen storage materials. Techniques of ion-induced electron emission (IEE) are suitable for the depth profiling of the hydrogen in the hydrogen storage materials (including 3D distribution using nuclear microprobe beam). In case of 3D imaging, lateral resolution of $1\times1\mu m^2$ can be achieved.

THERMAL NEUTRON INVESTIGATION OF MATERIALS FOR HYDROGEN STORAGE

M. Zoppi, M. Celli, D. Colognesi, A. Giannasi, L. Ulivi
Consiglio Nazionale delle Ricerche, Istituto Sistemi Complessi
Via Madonna del Piano 10, 50019 Sesto Fiorentino
Italy
marco.zoppi@isc.cnr.it

Abstract: Thermal neutron scattering is a well-established technique, in the field of hydrogen and hydrogen-storage materials, both from the fundamental and the applied points of view. Thanks to neutron scattering techniques it is possible, in general, to answer two fundamental questions at the microscopic level: 1) where are the hydrogen atoms located? 2) what are the hydrogen atoms doing? Answering to these questions is a task that thermal neutron scattering can do, thanks to their intrinsic properties. In this report, we will review the most relevant characteristics of hydrogen(s) in the framework of thermal neutron scattering techniques, namely diffraction and spectroscopy, and how, from the experimental results, it is possible to gain information on the microscopic structural properties of hydrogen containing materials and their dynamics.

1. INTRODUCTION

The fundamental concepts, necessary for the development of neutron scattering, were first introduced by Enrico Fermi in 1936 [1]. In a celebrated article entitled: *Sul moto dei neutroni nelle sostanze idrogenate* (On the motion of neutrons in hydrogenated substances) published on the CNR magazine *La Ricerca Scientifica*, Fermi introduces the concept of the so-called *Fermi pseudopotential* which represents the basic tool of neutron scattering techniques. Thanks to this conceptual advance, it was established that the interaction between the neutron and the nucleus could be considered point-like and this represented the cornerstone for a quantitative interpretation of the neutron scattering experiments.

Basically, neutrons can be produced in large numbers by means of two physical processes. The first one, nuclear fission, is well known and occurs when, for example, a nucleus of ^{235}U absorbs a neutron and decays into two light nuclei, producing two or three fast neutrons of ≈2 MeV kinetic energy. The second process is more recent and probably less widely known. Here, high-energy protons, produced by a particle accelerator, hit a target made of heavy nuclei, which in turn decay into smaller nuclides and a number of neutrons (15-30 neutrons per event). This process, called *spallation*, is used to produce intense pulsed neutron sources [2, 3]. In both cases, these high-energy neutrons are slowed down by suitable devices and moderated to produce a high flux of thermal neutrons.

Thermal neutron scattering has evolved greatly, in the last decades, allowing to investigate condensed matter systems to such an extent that was probably unforeseeable when Fermi made his first experiments [4]. Here, in the following, we will recall the foundations of thermal neutron scattering, discussing the difference with light and X ray scattering and then concentrating on applications to hydrogen and to hydrogen containing materials.

2. THERMAL NEUTRON PROPERTIES AND SCATTERING CROSS SECTION

Thermal neutrons are conventionally defined as those in equilibrium with a room temperature moderator. Thus, their average kinetic energy is close to 25.8 meV, which turns out to be rather close to the values of elementary excitations, like phonons, that are measured in condensed matter systems. As neutrons are elementary particles, it is easy to calculate their momentum and to associate a wavelength, according to the de Broglie law, which turns out to be around 1.78 Å. Again, we observe that this wavelength is rather close to the interatomic distances in condensed matter systems. To better clarify this concept, it is useful to show a

parallel view between photon scattering and neutron scattering, evidencing similarities and differences.

In a typical scattering experiment, a primary particle, either a neutron or a photon characterized by the three parameters $\{E_0, \mathbf{k}_0, \mathbf{e}_0\}$ (Fig. 1), interacts with a target, composed by N atoms, and a secondary particle $\{E_1, \mathbf{k}_1, \mathbf{e}_1\}$ is scattered. The double differential scattering cross section $\frac{d^2\sigma}{d\Omega dE}$ is defined according to the following equation:

$$dI = N\varphi(E_0)\, dE_0 \frac{d^2\sigma}{d\Omega dE} d\Omega\, dE \tag{1}$$

where: N is the number of scattering centers included in the scattering volume, $E = E_0 - E_1$ represents the energy transfer, I represents the number of detected scattering particles, $\varphi(E_0)$ is the flux distribution of the incident particles at E_0 energy, $d\Omega$ is the collection solid angle, and dE is the energy window around the final energy E_1.

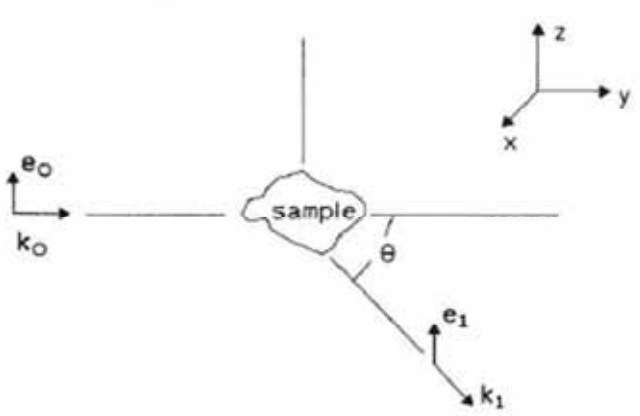

FIG. 1. A typical scattering configuration. The incident particles, either neutrons or photons, are characterized by their energy, E_0, momentum, $\hbar\mathbf{k}_0$, and polarization vector $\mathbf{e}_0$. The same quantities for the scattered particles are denoted by E_1, $\hbar\mathbf{k}_1$, $\mathbf{e}_1$. The scattering angle is denoted by θ.

With this notation, the double differential scattering cross section can be defined by the time-Fourier transform of a **k**-dependent correlation function [5]:

$$\left[\frac{d^2\sigma}{d\Omega dE}\right] = \frac{k_1}{k_0}\frac{1}{2\pi\hbar}\int_{-\infty}^{+\infty} dt\, \exp\{-i\omega t\}\, \Im(\mathbf{k}, t) \tag{2}$$

where $\mathbf{k} = \mathbf{k}_0 - \mathbf{k}_1$ represents the momentum transfer and $\omega = E/\hbar$. The function $\Im(\mathbf{k}, t)$ depends on the microscopic space-time correlations of the sample as well as on the characteristics of the interaction between the probe and the sample.

If optical light scattering is considered, the relevant wavelength of the probe is of the order of λ=5000 Å and the single molecules assume the role of scattering centers. In this case, the

electric dipole approximation applies and the space-time correlation function can be expressed as [6]:

$$\Im_L(\mathbf{k},t) = \frac{1}{N}\sum_{j,l} \left\langle e^{-i\mathbf{k}\cdot\mathbf{r}_j(0)} \left[\mathbf{e}_0 \cdot \vec{\vec{A}}_j(0)\cdot\mathbf{e}_1\right]^* \left[\mathbf{e}_0 \cdot \vec{\vec{A}}_l(t)\cdot\mathbf{e}_1\right] e^{i\mathbf{k}\cdot\mathbf{r}_l(t)} \right\rangle \quad (3)$$

Here, the second-order tensor $\vec{\vec{A}}_j$ represents a molecular polarizability, centered at position $\mathbf{r}_j$, and accounting for the fact that photons interact with the electronic cloud of molecules. If we concentrate on polarized scattering, then $\mathbf{e}_0 = \mathbf{e}_1$ and $\Im_L(\mathbf{k},t)$ reduces to:

$$\Im_L(\mathbf{k},t) = \frac{\alpha^2}{N}\sum_{j,l} \left\langle e^{-i\mathbf{k}\cdot\mathbf{r}_j(0)} \; e^{i\mathbf{k}\cdot\mathbf{r}_l(t)} \right\rangle = \alpha^2 F(\mathbf{k},t) \quad (4)$$

The function $F(\mathbf{k},t)$ is called the intermediate scattering function [5] and contains the information about the space-time correlation between the scattering center $\mathbf{r}_j$, considered at time t=0, and the scattering center $\mathbf{r}_l$, considered at time t. As the index j (as well as l) runs on all scattering centers, $F(\mathbf{k},t)$ contains both the self (j=l) and distinct (j≠l) correlations. We should remember that only if monatomic systems are considered the polarizability tensor can be exactly located on a nuclear position. For molecular systems, the center of mass and the center of electronic charge are rarely coinciding.

Slightly different considerations apply to X rays. In this case, due to the much shorter wavelength of the probe, the electric dipole approximation fails and each single electron becomes a scattering center. Nevertheless, assuming that the adiabatic approximation holds, the final expression for the cross section can be recast in a similar form to that of Eq. 3. In fact, considering again a set of N distinct nuclei, the corresponding expression becomes [7]:

$$\Im_X(\mathbf{k},t) = Z^2 r_c^2 \left|\mathbf{e}_0\cdot\mathbf{e}_1\right|^2 \; f^2(k)\,\frac{1}{N}\sum_{j,l} \left\langle e^{-i\mathbf{k}\cdot\mathbf{R}_j(0)} \; e^{i\mathbf{k}\cdot\mathbf{R}_l(t)} \right\rangle = Z^2 r_c^2 \left|\mathbf{e}_0\cdot\mathbf{e}_1\right|^2 \; f^2(k)\, F(\mathbf{k},t) \quad (5)$$

where Z is the atomic number, r_c is the electron classical radius, and $f(k)$ is the atomic form factor obtained from the space Fourier transform of the atomic electron cloud distribution. Here, $\mathbf{R}_j$ represents the position of the j-th nucleus and coincides with its center of charge. Of course, if molecular systems are considered, this assumption may become approximate. At any rate, this approximation is still considered rather accurate for high atomic number atoms, when many inner core electrons are present.

For neutrons, the overall picture appears rather different. First, we should consider that in a neutron scattering event a nuclear spin transition is involved. This implies that the cross section splits in two different components depending on the intrinsic (coherent or incoherent) nature of the scattering event [8]. Thus, for neutron scattering Eq. 3 becomes:

$$\Im_N(\mathbf{k},t) = \Im_{N,dist}(\mathbf{k},t) + \Im_{N,self}(\mathbf{k},t) \quad (6)$$

and the space-time correlation function $\Im_N(\mathbf{k},t)$ is split into a *distinct*:

$$\Im_{N,dist}(\mathbf{k},t) = \frac{1}{N}\sum_j \sum_{l\neq j} \overline{b}_j^{*}\ \overline{b}_l \left\langle e^{-i\mathbf{k}\cdot\mathbf{R}_j(0)}\ e^{i\mathbf{k}\cdot\mathbf{R}_l(t)} \right\rangle \tag{7}$$

and a *self* component:

$$\Im_{N,self}(\mathbf{k},t) = \frac{1}{N}\sum_j \overline{b_j^2} \left\langle e^{-i\mathbf{k}\cdot\mathbf{R}_j(0)}\ e^{i\mathbf{k}\cdot\mathbf{R}_j(t)} \right\rangle \tag{8}$$

Here, the b_j parameter represents the nuclear scattering length and turns out to be characteristic of the particular nucleus j. The top bars on the scattering lengths represent an average on the nuclear spin states [8]. It is important to point out that a fundamental ingredient of this theoretical derivation resides in the application of the Fermi pseudopotential concept, which allows to rigorously assuming the single nucleus as a point scattering center.

Summing up, we have shown that molecules are the basic scattering centers when using optical photons. The inner core electron distribution of single atoms assumes this role when X ray scattering is considered, while only with neutrons the scattering center can be rigorously assumed as centered on the nuclei. We should now remember that neutron production is quite expensive. A neutron scattering facility, either based on a nuclear fission reactor or a pulsed spallation source, is much more expensive than an X ray factory. In addition, the neutron flux that can be produced on those establishments is orders of magnitude smaller than those obtained at a synchrotron radiation source. Both neutrons and X rays are much more expensive than an optical laser source. However, we have also seen that each probe is characterized by a peculiar interaction with condensed matter samples and the kind of information obtained by each probe is not fully equivalent. Therefore, we should bear in mind that the use of neutrons should be reserved to those problems where all other techniques fail or give insufficiently accurate information.

3. NEUTRON SPECTROSCOPY AND HYDROGEN

As we have seen in Section 2, there is a fundamental difference between neutron and X ray cross section. In spite of the fact that both can probe the atomic distribution of matter, given the similarity in their wavelength, we should remember that some remarkable differences make neutrons special. In Figure 2 we report a comparison between the neutron and X ray scattering cross section for the various elements. According to Eq. 5, the X ray scattering cross section increases with the square of the atomic number, Z^2. This implies that measuring a hydrogen containing sample using X rays may be rather hard task. In fact, almost any metal has a scattering cross section that is orders of magnitude larger than that of hydrogen. In addition, if the electronic cloud of protons is delocalized, in other words if bare protons are diffusing in a solid lattice, hydrogen is virtually transparent to X rays. On the contrary, due to a fortunate circumstance, the neutron scattering cross section of ^{1}H is almost one order of magnitude larger, apart from rare and well-defined exceptions, than that of all the other elements. This implies that hydrogen is well visible by neutrons, even if embedded in a dense lattice of heavy nuclei. This peculiar character of hydrogen provides the basis for an important class of instruments that can be operated at pulsed neutron sources.

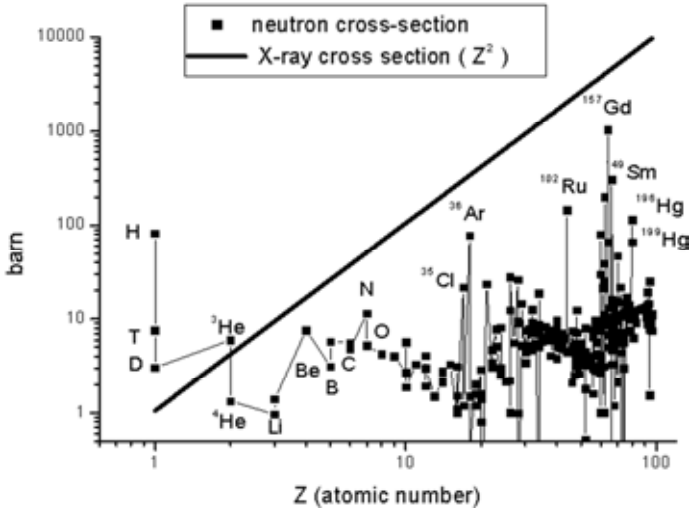

FIG. 2. Total scattering cross section of the elements (squares). The line represents the equivalent cross section for X rays.

If we recall the importance that Raman scattering has assumed for the development of the molecular theory, we can immediately understand what kind of role a neutron Raman-like spectrometer can assume in the investigation of hydrogen containing materials. TOSCA is an inverse geometry neutron spectrometer that was built in a cooperation activity between Italian CNR and CCLRC (UK). Here, a white beam of neutrons impinges on a sample and is diffused at fixed scattering angles. The secondary neutrons are energy selected by a combination of a graphite single crystal and a beryllium filter. Thus, from the knowledge of the neutron Time of Flight (TOF), it is possible to derive the value of the incident neutron energy. This has an important practical consequence, namely the possibility of detecting an inelastic spectrum extending from 0 to ≈ 500 meV (0-4032 cm^{-1}). Unfortunately, due to the kinematic relations between energy and momentum transfer, k is not constant along the spectrum and increases approximately with $E^{\frac{1}{2}}$. This implies that, at higher energy transfer, an intrinsic line broadening due to the increase of the Debye-Waller factor is observed. Nevertheless, the instrument is extremely useful in the low-intermediate region of the observed spectrum, where the resolving power is not too much dissimilar from that of an optical instrument [9-11].

One of the first applications of TOSCA to hydrogen related science was the measurement of the mean translational kinetic energy of molecules in liquid and solid hydrogen [12,13]. Then, we were able to use the inelastic spectra of TOSCA to obtain information on the microscopic dynamics of molecular hydrogen in the liquid state [14,15]. These measurements were further extended to obtain the density of phonon states in solid para-hydrogen [16] and to the measurement of lattice vibrations of para-hydrogen impurities in a matrix of deuterium [17]. In Fig. 3 we show, as an example, the measured spectrum of liquid parahydrogen. Each peak represents a rotational transition starting from the ground level $J = 0$. The transitions to the even levels are weighted by the small ^1H coherent cross section and therefore only the transitions to the odd levels $J' = 1,3,5,7$ are visible.

As we increased our confidence in the instrument capabilities, we also started to pay attention to a more important class of hydrogen compounds: namely the hydrides. We started our experiments with a quantum compound LiH [18] then extending the investigation to the other

compounds of the first [19] and the second [20] group of the periodic table. Further experiments on more complex hydrides are currently under analysis.

In the previous paragraphs we have explained how, taking advantage of the huge neutron scattering cross section of ^{1}H, we could exploit the inelastic scattering to obtain direct information on the hydrogen dynamics. However, what we did not mention, yet, was that this large scattering cross section was mainly due to the incoherent contribution to the total scattering cross section. As a matter of fact, the total neutron scattering cross section of ^{1}H turns out to be 82.02 barn, of which 1.76 barn represents the coherent contribution while the incoherent contribution amounts to 80.26 barn. In fact, the previously described technique is named Incoherent Inelastic Neutron Scattering (IINS) and applies mainly to the investigation of the hydrogen self dynamics. However, when we move our attention to the collective dynamics, or to structural properties, for example using neutron diffraction experiments, this fact should be carefully considered and a totally different point of view should be taken.

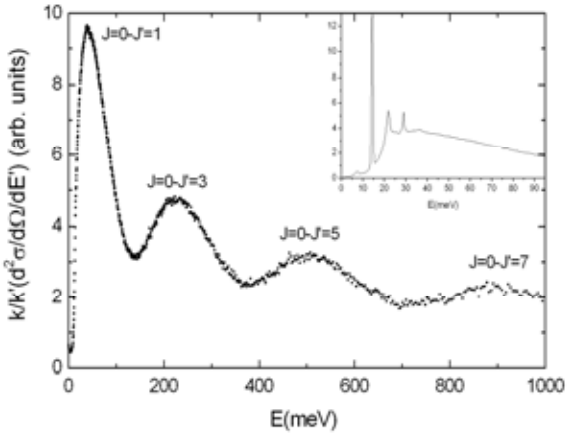

FIG. 3. Experimental IINS spectrum of liquid para-hydrogen at T=17.2 K. The peaks represent the observed molecular rotational transition, broadened and shifter by recoil. In the inset, the spectrum of solid para-hydrogen is shown. Here, the recoil is absorbed by the crystal lattice and the 1st rotational transition appears at its proper value of 14.43 meV.

4. NEUTRON DIFFRACTION AND HYDROGEN

In a neutron diffraction experiment, the nominal scattering cross section is obtained by integrating the double differential cross section over all possible final energies E_1. Namely:

$$dI = N \int_0^\infty dE_1 \; \varphi(E_0)\, dE_0 \frac{d^2\sigma}{d\Omega dE} d\Omega \,. \tag{9}$$

By assuming fixed incident energy, E_0, this implies:

$$dI = N \; \varphi(E_0)\, dE_0 \left[\int_0^\infty dE_1 \; \frac{d^2\sigma}{d\Omega dE} \right] d\Omega = N \; \varphi(E_0)\, dE_0 \frac{d\sigma}{d\Omega} d\Omega \tag{10}$$

and the differential scattering cross section becomes:

$$\frac{d\sigma}{d\Omega} = \int_0^{\infty} dE_1 \, \frac{k_1}{k_0} \, \frac{1}{2\pi\hbar} \int_{-\infty}^{+\infty} dt \, \exp\{-i\omega t\} \, \Im(\mathbf{k}, t) \tag{11}$$

If we assume that the relevant transitions in the sample are well defined, and that the incident neutron energy is so large that a change of variable from E_1 to E allows to extend the integral from $-\infty$ to $+\infty$, then we can also assume that $k_1 \cong k_0$ (static approximation) and the differential scattering cross section becomes:

$$\frac{d\sigma}{d\Omega} = \Im(\mathbf{k}, 0) \tag{12}$$

The static approximation is generally well satisfied with photons, thanks to the relatively high energy of the probe. However, since thermal neutron energies are close to the values of elementary excitations, this approximation should be carefully tested, case by case, in a neutron diffraction experiment. At any rate, assuming that the approximation holds and that the static approximation can be applied, the neutron scattering function becomes:

$$\Im_N(\mathbf{k}, 0) = \Im_{N,dist}(\mathbf{k}, 0) + \Im_{N,self}(\mathbf{k}, 0) \, . \tag{13}$$

Thus, the static *distinct* space correlation function is:

$$\Im_{N,dist}(\mathbf{k}, 0) = \frac{1}{N} \sum_j \sum_{l \neq j} \overline{b}_j^* \, \overline{b}_l \left\langle e^{-i\mathbf{k}\cdot\mathbf{R}_j} \, e^{i\mathbf{k}\cdot\mathbf{R}_l} \right\rangle \tag{14}$$

while the static *self* correlation component reduces to a constant background:

$$\Im_{N,self}(\mathbf{k}, 0) = \frac{1}{N} \sum_j \overline{b_j^2} \tag{15}$$

Thus, it becomes apparent why a diffraction experiment on hydrogen containing materials is a difficult task. In fact, the coherent scattering length weights the space correlations, producing the structural information, and this tiny signal superimposes to a large background, produced by the incoherent scattering cross section. This task, even though difficult, is not impossible. In fact, the structure factor of liquid para-hydrogen has been actually measured in different independent experiments obtaining consistent results [21, 22].

The problem of the large incoherent cross section of hydrogen, with respect to the coherent one, can be eluded using a different isotope. As a matter of fact, deuterium has a coherent cross section of 5.59 barn, which compares with an incoherent one of 2.05 barn. In this case, the expected background is smaller than the amplitude of the coherent signal. In fact, deuterium is frequently used, in place of hydrogen, when performing neutron diffraction experiments on hydrogen storage materials. To give an example, we will report a short description of a neutron diffraction experiment on deuterium adsorbed on carbon nanotubes. The experiment was carried out at the liquid and amorphous diffractometer SANDALS at ISIS (UK). In Fig. 4, we show a typical diffraction spectrum for molecular deuterium adsorbed on single walled carbonnanotubes (SWCN). The difference between the two patterns contains information about the location of molecular deuterium on the surface of the nanotubes.

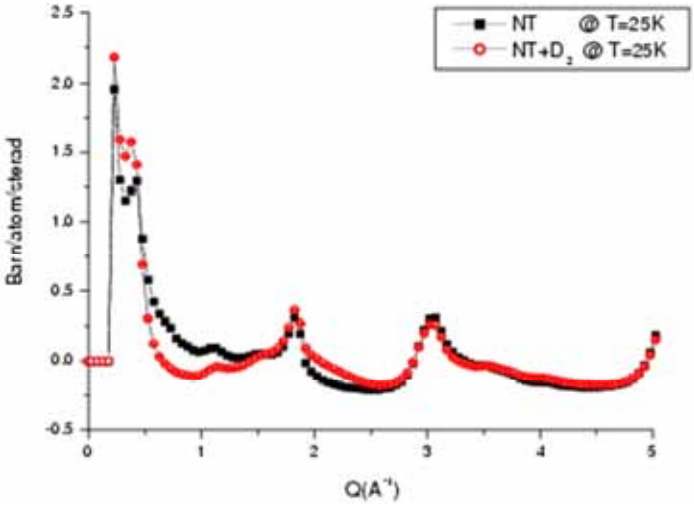

FIG. 4. Coherent contribution to the neutron diffraction scattering cross section of a bare single-walled carbon nanotube sample (full squares). The open circles show the same quantity when the sample is charged with deuterium.

In principle, by a careful analysis of the diffraction pattern, it should be possible to determine accurately the location of the hydrogen (deuterium) molecule in the lattice of the substrate. However, this is only possible if the substrate is well characterized and modeled. In practice, this is not an easy task and even purified samples rarely pass the test of an accurate neutron scattering experiment [23]. Thus a combination of neutron diffraction and spectroscopy can add useful information on these samples. To give an example, we recall two neutron spectroscopy experiments carried out both on TOSCA [24] and on the IN4 spectrometer at ILL (F) [25].

5. COMBINING NEUTRON AND OPTICAL SPECTROSCOPY

In the recent literature, hydrogen clathrates have been proposed as a possible hydrogen storage medium. Structurally, these are composed by a combination of dodecahedral (5^{12}) and exakaidecahedral ($5^{12}6^4$) cages of water molecules to form an overall cubic structure. By assuming a population of two hydrogen molecules in the small cages, and four in the large cages, a theoretical capacity around 5 wt% was evaluated [26]. The only drawback of this compound was its formation pressure, around 2 kbar. However, once formed and cooled down to liquid nitrogen temperature, the compound remains stable indefinitely. Clathrate hydrates are well known solid structures that form spontaneously in water to enclose small molecules. Methane clathrates are known to be present in the ocean depths and in the permafrost. Following this previous paper, an interesting report appeared in the literature showing that hydrogen clathrates could be formed, at much lower pressure, if a mixture of water and tetrahydrofuran (THF) was used [27]. In this case, the THF molecule would be trapped in the large cages stabilizing the clathrate at low pressure. Of course, this would decrease the hydrogen storage capacity but did not actually decrease the scientific interest in these compounds.

Neutron scattering experiments have been carried out on these compounds using the TOSCA spectrometer. Initially, the basic sample was produced using D2O and fully deuterated THF to which gaseous hydrogen was added once the clathrate was formed around 0°C temperature. By a careful selection of the sample, using different ortho-para hydrogen concentrations or HD, we were able to assign the measured spectral bands to rotational and center-of-mass

translational transitions of either para- or ortho-hydrogen. The hydrogen molecule was found to rotate almost freely in the cages while performing a rattling motion in the water cage [28]. In analyzing that experiment, we found extremely useful to combine some information, which we were able to derive from a parallel Raman scattering experiment carried out in our own laboratory. In fact, by means of Raman scattering we were able to calibrate exactly the amount of ortho- and para-hydrogen in each sample and we could use this information to evaluate the neutron spectra of each component, allowing us to correctly assign the neutron spectral bands.

Further Raman scattering experiments were carried out on clathrates with and without THF. In this case, we could compare experimental data where hydrogen was filling either the small cages only (clathrates with THF) or both the large and small cages (clathrates without THF). Interestingly, the rich hydrogen vibrational spectrum, measured by Raman spectroscopy at 4120 cm^{-1} and almost inaccessible to neutron scattering, turned out to contain important information on the cage populations [29]. It should be pointed out that, even in this case, the possibility of substituting hydrogen with deuterium or HD turned out in a better understanding of the spectra shapes and a careful assignment of the spectral features.

6. CONCLUSIONS

Thermal neutron scattering is an extremely powerful technique to investigate hydrogen and hydrogen-storage materials. Thanks to neutron diffraction it is possible to locate the atomic positions and to evaluate spatial correlation functions. However, since real samples are not always perfectly defined, this information may not turn out sufficiently deterministic. Neutron spectroscopy can actually shed light on the hydrogen dynamics that, in turn, add information on the molecular environment. However, one should never forget that a single experimental technique is never able, by itself, to solve all problems arising in the determination of the structural and dynamic features of a real sample. Thus a balanced combination of several experimental techniques can effectively complement neutron scattering experiments on any circumstance, including hydrogen containing materials.

REFERENCES

[1] FERMI, E., La Ricerca Scientifica, **VII**-II (1936) 13.
[2] http://www.isis.rl.ac.uk
[3] http://neutrons.ornl.gov/facilities/facilities_sns.shtml
[4] AMALDI, E., FERMI, E., Phys. Rev. **50** (1936) 899.
[5] VAN HOVE, L., Phys. Rev. **95** (1954) 249.
[6] BALUCANI, U., ZOPPI, M., Clarendon Press, Oxford (1994).
[7] BURKEL, E., Rep. Prog. Phys. **63** (2000) 171.
[8] LOVESEY, S.W., Oxford University Press, Oxford (1987).
[9] BOWDEN, Z.A., et al., Physica B: Condensed Matter **276-278** (2000) 98.
[10] http://www.isis.rl.ac.uk/molecularspectroscopy/tosca/
[11] COLOGNESI, D., et al., Appl. Phys. A **74** (2002) S64.
[12] CELLI, M., COLOGNESI, D., ZOPPI, M., Physica B **276-278** (2000) 814.
[13] CELLI, M., COLOGNESI, D., ZOPPI, M., Eur. Phys. J. B **14** (2000) 239.
[14] ZOPPI, M., COLOGNESI, D., CELLI, M., Europhys. Lett. **53** (2001) 34.
[15] CELLI, M., COLOGNESI, D., ZOPPI, M., Phys. Rev. E **66** (2002) 021202.
[16] COLOGNESI, D., CELLI, M., ZOPPI, M., J. Chem. Phys. **120** (2004) 5657.
[17] COLOGNESI, D., CELLI, RAMIREZ-CUESTA, A.J., M., ZOPPI, M., Phys. Rev. B **76** (2007) 174304.

[18] BORONAT, J., CAZORLA, C., COLOGNESI, D., ZOPPI, M., Phys. Rev. B **69** (2004) 174302.
[19] AUFFERMANN, G., BARRERA G.D, COLOGNESI, D., CORRADI, G., RAMIREZ-CUESTA, A.J., ZOPPI, M., J. Phys.: Condens. Matter **16** (2204) 5731.
[20] COLOGNESI, D., BARRERA, G., RAMIREZ-CUESTA, A.J., ZOPPI, M., J. Alloys Compd. **427** (2007) 18.
[21] DAWIDOWSKI, J., et al., Phys. Rev. B **69** (2004) 014207.
[22] CELLI, M., et al., Phys. Rev. B **71** (2005) 014205.
[23] GIANNASI, A., BOWRON, D.T., CELLI, M., SAUVAJOL, J.L., ZOPPI, M., Carbon **45** (2007) 943.
[24] GEORGIEV, et al., J. Phys.: Condens. Matter **16** (2004) L73.
[25] GEORGIEV, P.A., et al., Chem. Phys. **328** (2006) 318.
[26] MAO, W.L., et al., Science **297** (2002) 2247.
[27] FLORUSSE, L.J., et al., Science **306** (2004) 469.
[28] ULIVI, L., et al., Phys. Rev. B **76** (2007) 161401.
[29] GIANNASI, A., CELLI, M., ULIVI, L., ZOPPI M., J. Chem. Phys. **129** (2008) 084705.

DIFFRACTION STUDIES OF MATERIALS FOR HYDROGEN STORAGE

B.C. HAUBACK
Physics Department, Institute for Energy Technology
P.O. Box 40, 2027 Kjeller
Norway
bjorn.hauback@ife.no

Abstract: An effective and safe method for storage of hydrogen is one of the greatest technologically challenging barriers of widespread introduction of hydrogen in global energy systems. Hydrogen storage in solid materials is the only method that can fulfil international long term goals for the use of hydrogen in vehicles. At present no materials satisfy each of the following targets: high gravimetric and volumetric density, appropriate thermodynamics and good kinetics. However, during the last years a number of promising materials have been developed, and in particular lightweight complex hydrides based on aluminium, nitrogen and boron have the potential to meet the requirements. To reach these goals, research efforts using a combination of advanced modelling, synthesis methods and characterization tools are required. Nuclear methods and in particular neutron diffraction is the only method to determine complete crystal structures of hydrogen storage materials.

1. INTRODUCTION

During the last decade there has been a significantly increased focus on hydrogen as the future energy carrier. Hydrogen storage is a crucial step for providing a ready supply of hydrogen fuel to an end user, such as for mobile applications. Without effective storage systems, a Hydrogen Economy will be difficult to achieve. Hydrogen storage remains an undisputed problem for hydrogen fuelled vehicles, and it is considered by many to be the most technologically challenging aspect. For practical applications, a transport storage system should fulfil several requirements including high gravimetric and volumetric densities, appropriate thermodynamics, good kinetics (for hydrogen uptake and release), acceptable safety, low cost, etc. During the years, several countries have defined targets for hydrogen storage, for example US Department of Energy (DOE), NEDO in Japan and the European Commission like in the FP 6 project NESSHY 'Novel Efficient Solid Storage for Hydrogen'. These targets include a number of parameters important for practical hydrogen storage systems. One example is the targets given by the US DOE. Their two most cited targets are 6 wt% hydrogen system gravimetric capacity and 1.5 kWh/L system volumetric capacity for applications in vehicles (Fig. 1). As shown in the figure compressed or liquid hydrogen are at present not meeting these long term goals for hydrogen storage. Main problems with liquid and compressed hydrogen storage are energy losses during liquefaction (30-40 %) and compression, volumetric and gravimetric densities (most severe for compressed hydrogen) and safety considerations. Thus the only acceptable sustainable long term solution for vehicles is hydrogen storage in solid materials.

In spite of the significant achievements related to hydrogen storage in solid materials during the last years, further progress is still needed to fulfil the international goals. A major challenge is therefore to find materials and hydrogen storage systems fulfilling *all* these requirements. Such research efforts will require new materials and solutions, and not simple, incremental improvements in current technologies. Task 22 of the Hydrogen Implementation Agreement of the International Energy Agency (HIA IEA) (www.ieahia.org) is addressing 'Fundamental and applied hydrogen storage materials development'.

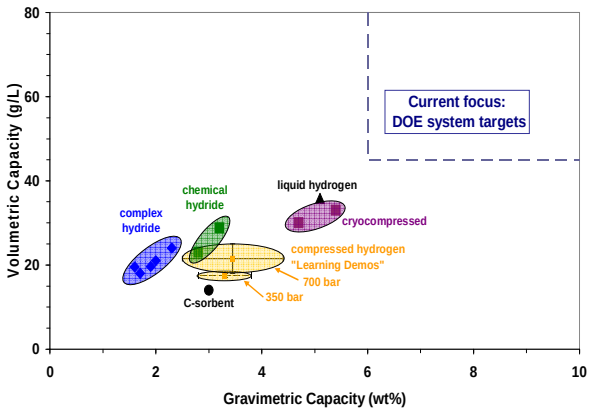

FIG. 1. Volumetric hydrogen density (g/L) versus gravimetric density (wt%) for different hydrogen storage systems related to DoE systems targets.

2. NUCLEAR METHODS FOR STUDIES OF HYDROGEN STORAGE MATERIALS

In order to understand the properties of materials and also to be able to determine new compounds, detailed knowledge about the position of the atoms is of major importance. When Friedrich et al. in 1912 found the direct relationship between the observed diffraction pattern when X rays irradiated a crystalline solid compound and the corresponding arrangement of atoms in the structure, the interdisciplinary field of crystallography started to develop. Today crystallography is very important in many areas of science. Sources for diffraction studies are X rays, neutrons and electrons, and each of these methods has specific properties and challenges. For studies of hydrogen storage materials both neutron and X ray diffraction are important, but in particular neutron scattering techniques play a crucial role because of the significant scattering from hydrogen atoms.

X rays have wavelengths in the range between 0.1 and 100 Å. The wavelengths used for crystallographic studies are typically in the range 0.5 to 2.5 Å. Because of the availability and properties X ray diffraction is the most common technique for phase identification and structural characterization of crystalline materials. X rays are scattered by the electrons of the atoms. The most important consequence is a linearly increased scattering power as a function of the atomic number. In addition X rays interact strongly with matter.

The neutron is an uncharged particle found in all atomic nuclei except the ^{1}H nucleus. Neutrons with wavelength in the typical range 1 – 2.5 Å is available from nuclear reactors or spallation sources. The scattering process with neutrons is different from X rays. Neutrons are scattered by the atomic nuclei in a complex process. Important properties related to scattering by neutrons are:

- There are no correlation between the atomic number and the scattering length. Even scattering from different isotopes of the same element can differ significantly (Fig. 2).
- The neutron scattering lengths do not decrease or change with changing scattering angles.
- Neutrons interact usually weakly with matter (a few elements including boron have a strong absorption). An important effect of this is that complex sample environments like furnaces, cryostats, pressure cells etc can easily be used since neutron beams penetrate the material in such devices.
- Neutrons have a magnetic moment, and neutron scattering is the main method to determine magnetic ordering and magnetic structures.

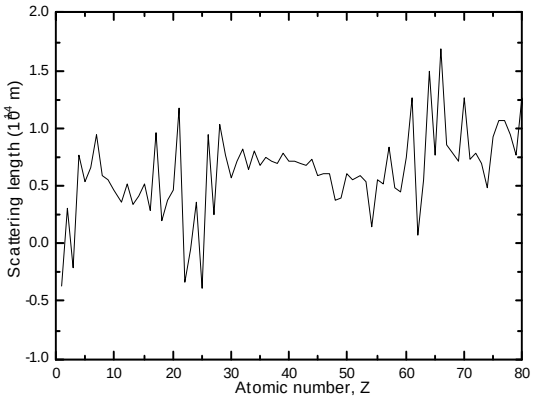

FIG. 2. Neutron scattering lengths as a function of atomic number Z [1].

The difference in the neutron scattering lengths between neighbouring elements and the overall nearly constant value going from light to heavy elements, gives two advantages with neutron diffraction:

- Neighbouring elements in the Periodic Table that are very difficult to distinguish by X ray diffraction may have significant different neutron scattering lengths, and thus they can be individually distinguished by neutrons.
- Opposite to X ray diffraction light and heavy elements often have comparable neutron scattering lengths. This is in particular important for hydrogen containing materials since scattering from hydrogen with neutrons is comparable to scattering from most other elements in the Periodic table.

Figure 3 illustrates the structure of the complex hydride Li_3AlD_6 from X ray and neutron 'views'. The X ray view mostly shows Al and Li with reduced accuracy. Neutron diffraction gives the complete structure including the hydrogen atoms.

The neutron scattering consists both of a coherent and incoherent part. For ^1H isotope, protium, (99.985% of natural hydrogen) gives very strong incoherent scattering, and this gives mainly a big background in the neutron diffraction data. On the other hand the isotope deuterium gives mainly coherent scattering which will contribute to the Bragg scattering. Deuterium is therefore preferred used instead of hydrogen in neutron diffraction studies of hydrides.

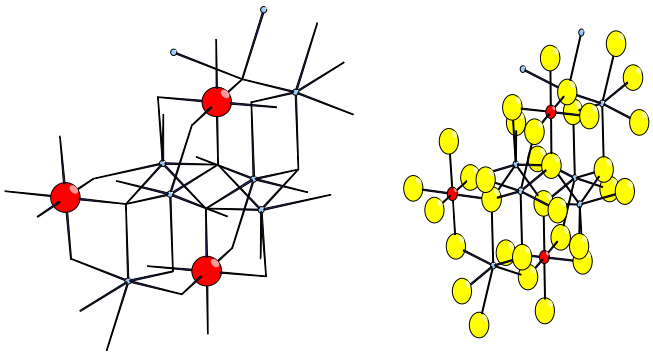

a) b)

FIG. 3. The structures of Li_3AlD_6 seen by (a) X ray diffraction (large red and small blue spheres are Al and Li, respectively); and (b) neutron diffraction (large yellow spheres, small red and small blue are D, Al and Li, respectively).

Laboratory source X ray diffraction equipment, both for single crystal and powder diffraction studies are widely available. Commonly used anode materials are Cu, Mo and Cr with X ray wavelengths corresponding to the $K\alpha_1$ transitions equal to 1.5404, 0.7093 and 2.2896 Å, respectively. During the last decades synchrotron X ray sources have been available in many countries and at present there are more than 50 synchrotrons worldwide. Today such facilities are the most powerful X ray radiation sources. The three most powerful synchrotron X ray sources are the European Synchrotron Radiation Facility (ESRF) in Grenoble, France, the Super Photon Ring (Spring-8) in Hyogo, Japan and the Advance Photon Source (APS) in Argonne, USA with electron energies 6.0, 8.0 and 7.0 GeV, respectively. Both the intensity of the X ray beam from the synchrotron and its divergence is much better than from a conventional X ray tube. The extremely high brilliance gives significantly improved possibilities for both high resolution and time resolved in situ experiments with synchrotrons.

As mentioned above, neutrons are in particular important for studies of hydrogen storage materials. Neutrons can be produced either in nuclear reactors or by pulsed (spallation) neutron sources. One of the advantages of the neutrons is the continuous energy spectrum determined solely by the temperature of the moderator (a Maxwell-Boltzmann distribution). Thermal neutrons are produced for research reactors with water (heavy or light) as the moderator. The available wavelengths are typically in the range 1 to 2.5 Å with a maximum in intensity at about 1.3 Å. Longer wavelengths can be obtained by using a cold moderator (usually a sphere filled with liquid hydrogen at 20 K) in some of the beam tubes. Shorter wavelength can be obtained by for example using a hot moderator using a graphite block. At present there are worldwide about 30 research reactors. Examples of the most intense reactors are ILL (Institut Laue-Langevin) in Grenoble, France, FRM II in Munich, Germany, BENSC (Hahn-Meitner Institut) in Berlin, Germany, NIST in Gaithersburg, USA, HFRI at Oak Ridge National Laboratory, USA, Canadian Neutron Beam Centre at Chalk River, Canada, and ANSTO in Australia. Another method to produce neutrons is by accelerator-based neutron sources usually named spallation sources. The spallation method is the most efficient way to produce neutrons, and the neutron flux is higher than for neutrons produced in reactors. The neutrons can be used in different diffraction studies, and mostly in so-called time-of-flight (TOF) experiments. The most powerful spallation sources at present (2009) are the Spallation Neutron Source (SNS) at Oak Ridge in USA and Proton Accelerator Research Complex (J-PARC) in Tokai, Japan. Other important sources are ISIS in Didcot, UK, LANCE at Los Alamos National Laboratory, USA and IPNS at Argonne National Laboratory, USA. An important planned spallation source is the European Spallation Source (ESS).

JEEP II at Institute for Energy Technology is a 2 MW heavy-water moderated research reactor that has been in operation since 1967. JEEP II is classified as a low-flux reactor. The powder neutron diffractometer PUS has been used to study many new light-weight metal hydrides during the last year. The diffractometer is shown in Fig. 4 [2]. Monochromatic neutrons with wavelength 1.5560 Å are obtained by reflection from a Ge (511) of a focussing composite monochromator with approximately 90° take-off angle. The detector unit consists of two banks of seven position-sensitive ^{3}He detectors, each covering 20° in 2θ. Typically data is collected between 10 and 130° in 2θ. The structures presented here are determined with the PUS instrument and in many cases in combination with synchrotron X rays.

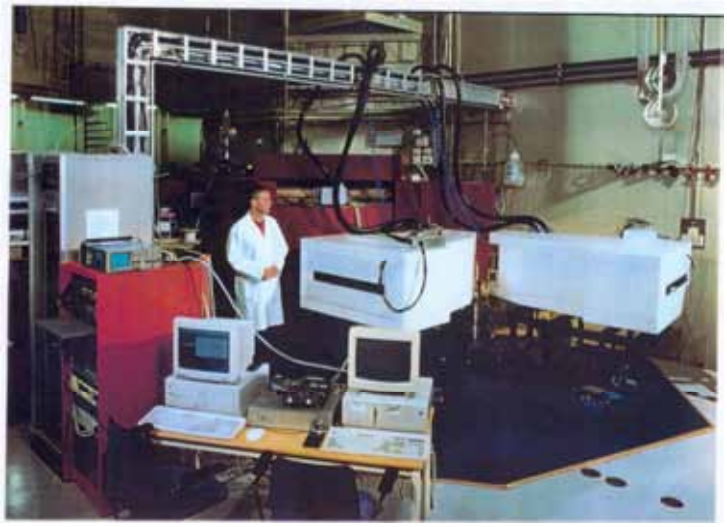

FIG. 4. The PUS powder neutron diffractometer at the JEEP II reactor at Institute for Energy Technology.

3. HYDROGEN STORAGE IN SOLID COMPOUNDS

Reversible metal hydrides have been studied for several decades. In the traditional intermetallic hydrides based on AB_5, AB_2, AB, A_2B alloys the thermodynamics can be adjusted by alloying, but these compounds are typically too heavy for vehicles [3]. Up to about 3 wt% hydrogen can be stored in solid solution body-centred-cubic (bcc) alloys, e.g. Ti-V-Mn and V-Ti-Fe [4]. These compounds are also candidates for hybrid solutions where metal hydrides and high pressure gas are combined. Binary hydrides based on alkali and alkaline-earth elements like LiH, NaH and MgH_2 are too stable, but in particular hydrogen storage in MgH_2 (7.6 wt% hydrogen) and Mg-based compounds (e.g. in complex transition metal hydrides like Mg_2FeH_6, Mg_2CoH_5, Mg_2NiH_4) with catalysts and nanosized particles are still significantly addressed [5]. Recently the mixed transition-metal complex hydride $Mg_2(FeH_6)_{0.5}(CoH_5)_{0.5}$ has been studied [6].

In nanoporous materials, H_2 molecules are adsorbed on surfaces and the amount of adsorbed hydrogen is a function of the total surface area. The H_2 molecules are weakly bonded (physisorbed), and in most cases a low temperature, typically liquid nitrogen temperature (77 K), has to be used for any significant storage of the H_2 molecules. During the last 10 years mainly different carbon-based materials [7] and metal organic frameworks (MOFs) [8] have been studied, but also hydrogen storage in for example zeolites and clathrates has been addressed.

For the chemical hydrides, for example amine borohydride, NH_4BH_4, can decompose in 4 steps with a very high hydrogen yield. Until now, the ammonia borane NH_3BH_3 has mostly been investigated [9]. AlH_3 (alane) with 10.1 wt% hydrogen is another promising regenerative hydrogen storage material, where hydrogen can be released at about 370 K, but a major challenge is the regeneration process [10].

The reversibility and improved kinetics found in Ti-enhanced $NaAlH_4$ [11] initiated a significant effort on alanates (aluminium-based compounds) and in recent years also on other complex hydrides based on nitrogen and boron for on-board hydrogen storage applications [1, 12, 13].

4. HYDRIDES BASED ON ALUMINIUM, NITROGEN AND BORON

A characteristic feature of the complex hydrides is the presence of anionic metal complexes. These compounds have mixed ionic-covalent bonding features. Within the anionic complex, hydrogen is covalently bonded. In alanates the H atoms are covalently bonded to Al in $[AlH_4]^-$ tetrahedra or $[AlH_6]^{3-}$ octahedra, and in borohydrides four H atoms are covalent bonded to boron in $[BH_4]^-$ tetrahedra. The cation is ionicly bonded to the anionic complex.

In addition to $NaAlH_4$ (with 7.5 wt% hydrogen content) other promising alanates with high hydrogen contents are $LiAlH_4$ (10.6 wt%), $Mg(AlH_4)_2$ (9.3 wt%), $Ca(AlH_4)_2$ (7.9 wt%) and $LiMg(AlH_4)_3$ (9.7 wt%). For example the $I4_1/a$ structure of $NaAlH_4$ consists of isolated $[AlH_4]^-$ tetrahedral, and each Na atom has eight H atoms as nearest neighbours (Fig. 5). The desorption of hydrogen from alkaline-based alanates takes place by the following two-step reaction:

$$MAlH_4 \leftrightarrow 1/3\ M_3AlH_6 + 2/3\ Al + H_2 \quad (1)$$

$$\leftrightarrow MH + Al + 3/2\ H_2 \quad (2)$$

where M = Li, Na or K. There exist several other alanates with AlH_6 octahedra based on alkali and earth-alkali elements. Examples of such compounds are $CaAlH_5$ and $LiMgAlH_6$, that are intermediate phases in the desorption from $Ca(AlH_4)_2$ and $LiMg(AlH_4)_2$, respectively, and mixed alanates like Na_2LiAlH_6 (Fig. 6), K_2NaAlH_6 and K_2LiAlH_6. An extensive overview of structures of alanates is given by Hauback et al. [1].

Many publications have during the last decade addressed the effect of additives, like Ti-based compounds, in alanates with advanced modelling and a number of experimental techniques, but the understanding is still limited. Recent studies have confirmed that the additives act as a nanosized catalyst which improves the kinetics, and transition metal (TM) catalysts are present on the surfaces both as crystalline and amorphous TM-Al phases [14, 15]. The alanates with the highest hydrogen capacity, $LiAlH_4$ and $Mg(AlH_4)_2$, have been considered to be irreversible and Ti-enhanced $NaAlH_4$ is the best complex hydride for vehicle applications even though the cycling hydrogen capacity is only 3–4 wt%. However very recently it has been shown that Ti-doped $LiAlH_4$ can operate as a reversible hydrogen storage material that can release up to 7 wt% hydrogen at temperatures as low as 80°C and that the material can be recharged almost quantitatively under remarkable mild conditions using liquid dimethyl ether as a solvent [16].

At present the crystal structure of four different modifications of AlD_3 – α, α', β and γ – has been determined by neutron diffraction [19]. One example is the structure of β-AlD_3 shown in Fig. 7. Typically these structures consist of corner-sharing AlD_6 octahedra. However, γ-AlD_3 constains edge-sharing octahedra in addition.

Based on the pioneering work of the reversible reaction in mixtures of $LiNH_2$ and LiH by [20] hydrogen storage in Li- and Mg-based amides and imides has been extensively studied. The most promising composites consists of $Mg(NH_2)_2$ and LiH in different ratios, e.g. $Mg(NH_2)_2$ + 4LiH, $Mg(NH_2)_2$ + 2LiH and $3Mg(NH_2)_2$ + 8LiH [21, 22]. The complete structures of $LiND_2$ and $Mg(ND_2)_2$ have recently been determined by Sorby et al. [23]. The 'best' combination with respect to reversible hydrogen capacity and desorption temperature seems to be the 3:8 ratio. The practical reversible storage capacity is >6 wt%, but limitations are still slow kinetics and too high temperature for hydrogen release. In addition, the presence of NH_3 during desorption is also an issue to be resolved. Still the hydrogenation/dehydrogenation processes including the presence of intermediated phases, structures of some of the key-phases and effect of catalysts are still poorly understood for these compounds [24].

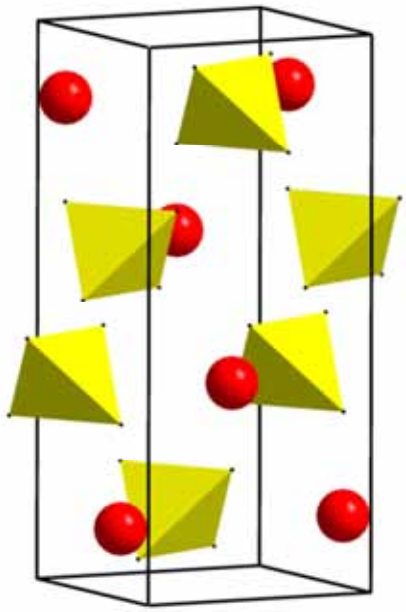

FIG. 5. The structure of $NaAlD_4$ (deuterided sample used for neutron diffraction [17].

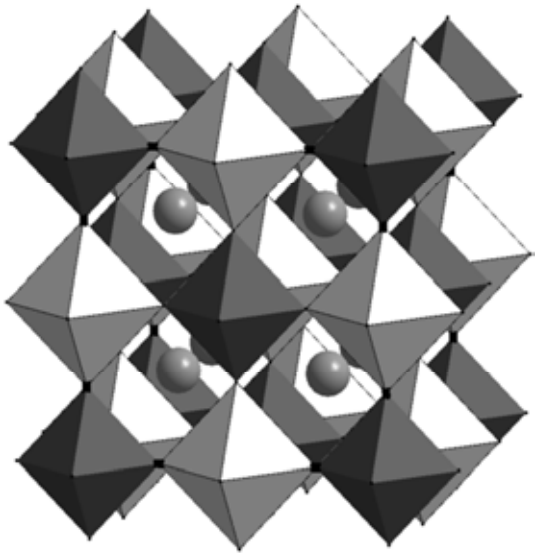

FIG. 6. The crystal structure of Na_2LiAlD_6 [18].

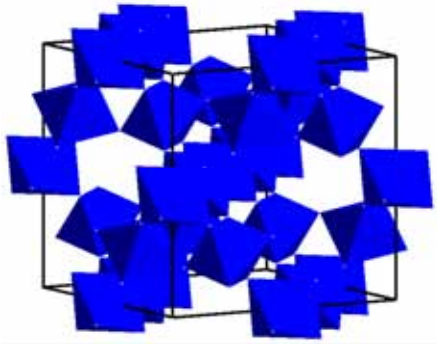

FIG. 7. The crystal structure of β-AlD_3 [25].

The complex hydrides with the highest hydrogen content are borohydrides like $LiBH_4$ (18.5 wt% hydrogen), $Mg(BH_4)_2$ (14.9 wt%) and $Ca(BH_4)_2$ (11.6 wt%). $LiBH_4$ can be prepared directly from the Li, B and H_2 at 970 K and hydrogen pressure of 150 bar [26]. The dehydrogenation process exhibits three distinct peaks in the temperature range 470-620 K indicating several intermediate steps, but the details have to be clarified [12]. For $Mg(BH_4)_2$ and $Ca(BH_4)_2$ the predicted decomposition enthalpies are in the range of low/medium-temperature hydrides if the following decomposition routes are assumed [12]:

$$Mg(BH_4)_2 \rightarrow MgH_2 + 2B + 3H_2 \quad (3)$$

$$Ca(BH_4)_2 \rightarrow 2/3CaH_2 + 1/3CaB_6 + 10/3H_2 \quad (4)$$

Recent NMR spectroscopy experiments [27] show strong evidence of the presence of $[B_{12}H_{12}]^{2-}$ in the partially decomposed borohydrides. It's showed [28] that $TiCl_3$-catalyzed $Ca(BH_4)_2$ can be partly rehydrogenated (3.8 wt% hydrogen) at 623 K and 90 bar of hydrogen. However, $Mg(BH_4)_2$ is still not found to be reversible. Detailed in situ synchrotron diffraction studies of $Ca(BH_4)_2$ and $Mg(BH_4)_2$ show several phase transitions and much more complicated decomposition routes than proposed according to eq. (3) and (4) (Fig. 8, Fig. 9) [29].

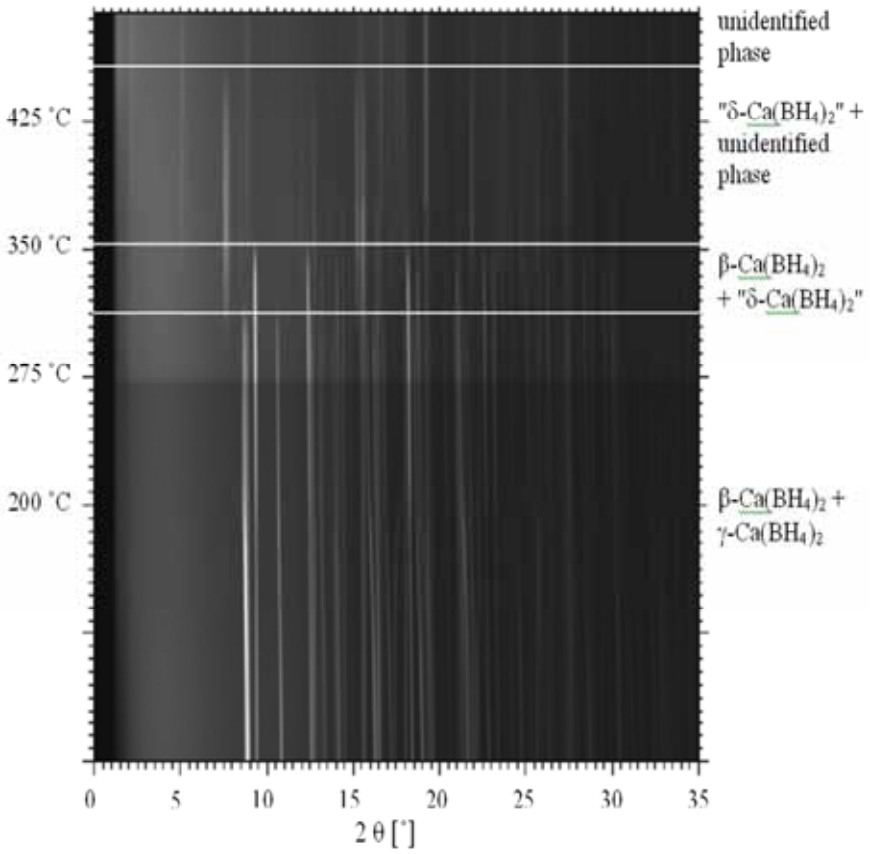

FIG. 8. Synchrotron X ray diffraction patterns for $Ca(BH_4)_2$; data as a function of temperature (40 – 500 °C) [29].

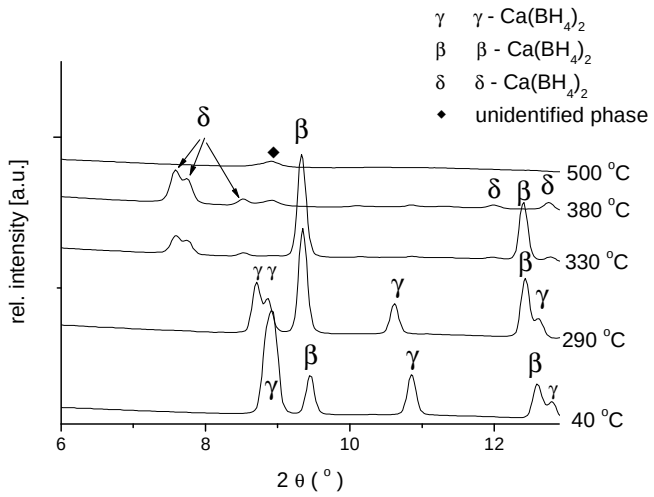

FIG. 9. Synchrotron X ray diffraction patterns for $Ca(BH_4)_2$; patterns at selected temperatures showing details from the different transition steps [29].

Recently, the crystal structure of an intermediate phase in the $Ca(BH_4)_2$ system have been solved based on synchrotron X ray diffraction data [30]. The composition is suggested to be CaB_2H_x. From desorption studies and refinements of the data, x is significantly smaller than 8, and our data suggests $x \approx 2$. The proposed structure is shown in Fig. 10.

Additional challenges for the boron-based compounds are the presence of both amorphous phases obtained during synthesis by ball-milling techniques and amorphous intermediate and end products during decomposition. At present, only limited data is available on hydrogenation and dehydrogenation properties including the presence of intermediate phases and their structures and the effect of catalysts in these compounds.

So-called 'destabilized hydrides', e.g. mixtures of $LiBH_4$ and MgH_2, are shown to be reversible, but the operating temperature is still too high and kinetics too slow [31]. Nanoparticles and nanostructured materials for hydrogen storage improve the reaction kinetics, but still it is not clear how the thermodynamics are influenced by size effects [32].

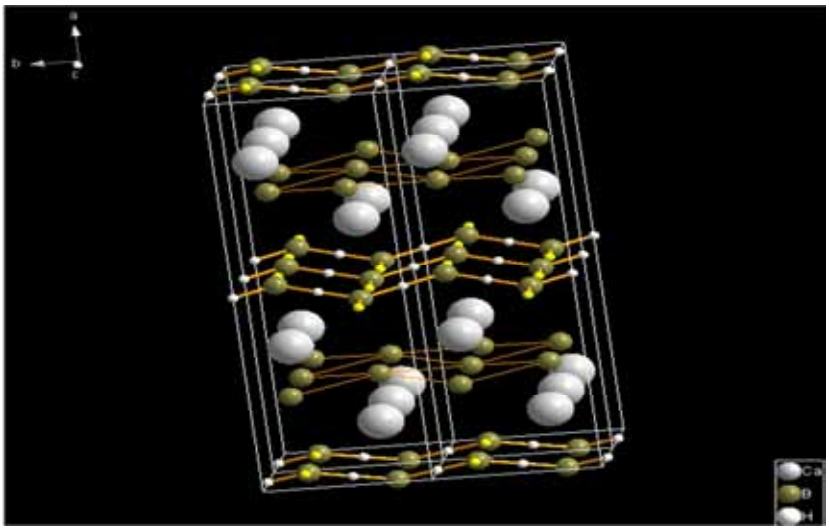

FIG. 10. The structure of CaB_2H_x with x=2. Large grey spheres: Ca; small grey spheres: H; and green spheres: B [30].

5. CONCLUSIONS

Hydrogen storage in solid materials is the long term goal. During the last 10-12 years a number of promising new lightweight materials have been developed and studied. However, still no materials satisfying each of the main targets with respect to storage capacities, thermodynamics and kinetics have been found, and further research in this field is strongly required. These efforts will involve combinations of theory and experiments, development and improvement of novel methods for synthesis and last, but not least, in situ methods and development of strategies for combination of different techniques for characterization. This is in particular important for studies of nanoscopic materials and the effect of catalysts. The understanding of for example the hydrogenation/dehydrogenation processes and effect of catalysts is still limited. A better understanding could also be important for development of improved materials for hydrogen storage. In these efforts, the use of nuclear methods is crucial.

REFERENCES

[1] HAUBACK, B.C., in Solid-state Hydrogen Storage Materials and Chemistry, Ed. G. Walker, Woodhead Publ. (2008).
[2] HAUBACK, B.C., et al., J. Neutron Res. **8** (2002) 215.
[3] BOWMAN JR., R.C., FULTZ, B., MRS Bulletin **27** (2002) 688-693.
[4] AKIBA, E., OKADA, M., MRS Bulletin **27** (2002) 699-703.
[5] DORNHEIM, M., et al., Scr. Mater. **56** (2007) 841.
[6] DELEDDA, S., HAUBACK, B.C., Nanotechnology **20** (2009) 204010.
[7] BÉNARD, P., CHAHINE, R., Scr. Mater. **56** (2007) 803-808.
[8] HIRSCHER, M., PANELLA, B., Scr. Mater. **56** (2007) 809-812.
[9] BOWDEN, M., AUTREY, T., BROWN, I., RYAN, M., Current App. Phys. **8** (2008) 498-500.
[10] SANDROCK, G., REILLY, J., GRAETZ, J., ZHOU, W.-M., JOHNSON, J., WEGRZYN, J. Appl. Phys. A **80** (2005) 687-690.
[11] BOGDANOVIĆ, B., SCHWICKARDI, M. J., J. Alloys Compd. **253** (1997) 1-9.
[12] ORIMO, S.-I., NAKAMORI, Y., ELISEO, J.R., ZÜTTEL, A., JENSEN, C.M., Chem. Rev. **107** (2007) 4111-4132.
[13] GRAETZ, J., Chem. Soc. Rev. **38** (2009) 73-82.
[14] BRINKS, H.W., HAUBACK, B.C., SRINIVASAN, S.S., JENSEN, C. M., J. Phys. Chem. B **109** (2005) 15780-15785.
[15] PITT, M.P., et al., C.M., ACTA MATER. **56** (2008) 4691-4701.
[16] LIU, X., MCGRADY, G.S., LANGMI, H.W., JENSEN, C.M., J. Am. Chem. Soc. **131** (2009) 5032-5033.
[17] HAUBACK, B.C., BRINKS, H.W., JENSEN, C.M., MURPHY, K., MAELAND, A.J., J. Alloys Compd. **358** (2003) 142-145.
[18] BRINKS, H.W., HAUBACK, B.C., JENSEN, C.M., ZIDAN, R., J. Alloys Compd **392** (2005) 27-30.
[19] HAUBACK, B.C., KRIST, Z., **223** (2008) 636-648.
[20] CHEN, P., XIONG, Z., LUO, J., LIN, J., TAN, K.L., Nature **420** (2002) 302-304.
[21] LENG, H.Y., et al., J. Phys. Chem. B **108** (2004) 8763-8765.
[22] NAKAMORI, Y., KITAHARA, G., MIWA, K., TOWATA, S., ORIMO, S., Appl. Phys. A **80** (2005) 1-3.
[23] SØRBY, M.H., et al., J. Alloys Compd. **428** (2007) 297–301.
[24] NAKAMURA, Y., HINO, S., ICHIKAWA, T., FUJII, H., BRINKS, H.W., HAUBACK, B.C., J. Alloys Compd. **457** (2008) 362-367.

[25] BRINKS, H.W., LANGLEY, W., JENSEN, C.M., GRAETZ, J., REILLEY, J.J., HAUBACK, B.C., J. Alloys Compd. **433** (2007) 180-183.
[26] FRIEDRICHS, O., et al., Acta Mater. **56** (2008) 949-954.
[27] HWANG, S.J., et al., J. Phys. Chem. C **112** (2008) 3164-3169.
[28] KIM, J.-H., JIN, S.-A., SHIM, J.-H., CHO, Y.W., Scr. Mater. **58** (2008) 481-483.
[29] RIKTOR, M.D., et al., J. Mater. Chem. **17** (2007) 4939-4942.
[30] RIKTOR, M.D., SØRBY, M.H., CHŁOPEK, K., FICTHNER, M., HAUBACK, B.C., J. Mater. Chem. **19** (2009) 2754-2759.
[31] VAJO, J.J., OLSON, G.L., Scr. Mater. **56** (2007) 829-834.
[32] BÉRUBÉ, V., RADTKE, G., DRESSELHAUS, M., CHEN, G., Int. J. Energy Res. **31** (2007) 637-663.

SMALL-ANGLE NEUTRON SCATTERING INVESTIGATIONS OF NANOCONFINED HYDRIDES

S. SARTORI, K.D. KNUDSEN, B.C. HAUBACK
Institute for Energy Technology
PO Box 40, NO-2027 Kjeller
Norway
sabrinas@ife.no

Abstract. One of the most promising issues for the introduction of the hydrogen economy is the use of hydrogen as energy vector in the form of solid storage material based on nanoscaffold hydrides. When dealing with nanoporous compounds, small-angle neutron scattering (SANS) gives invaluable information that can help to develop the most suitable material. In the present work nanoscale particles of $Mg(^{11}BD_4)_2$ and $NaAlD_4$ infiltrated in carbon scaffolds were studied by SANS and their behavior compared with the bulk powders. The particles size has been estimated to be in the range of 1-6 nm for the nanoconfined Mg-borohydride and < 5 nm in the case of infiltrated $NaAlD_4$.

1. INTRODUCTION

The introduction of hydrogen as an energy carrier of the future dictates to face significant challenges. High reversible storage capacity, fast kinetics, ambient operating temperature and acceptable safety are among the requirements of the transportation sector. Many research efforts are currently under way to develop new technologies for the storage of hydrogen. Solid state hydrogen materials are considered to be one of the most attractive solutions.

During the last years many groups have focused on the synthesis of nanosized metals and alloys [1-5] as an alternative way to improve the performances of metal hydrides. Improvements and changes in the hydrogenation/dehydrogenation properties of hydrides (such as $LiBH_4$, $Mg(BH_4)_2$ and $NaAlH_4$) when confined in microporous and mesoporous scaffolds have been reported [6-9].

The evidence that complex hydrides infiltrated in microporous carbon are indeed nanodispersed can be difficult to achieve. In this contest, small-angle neutron scattering (SANS) could be useful to extract information about the distribution of hydrogen containing structures, in particular the size-range distribution. With small-angle scattering techniques it is possible to obtain information on nanoparticles and clusters at length scales in the range of 1 to 1000 nm. Mass fractal and surface fractal dimensions can be extracted from the power-law scattering regime of the intensity (I) versus the scattering wave vector (**q**), where $q = |\mathbf{q}| = (4\pi/\lambda)(\sin\theta)$ and 2θ is the scattering angle [10-12]. When the scattering data satisfy the condition of qR >> 1, where R is the particle size, the scattered intensity I(q) can be approximated as proportional to $q^{-\alpha}$. The power-law scattering exponent α can thus be evaluated from a plot of log (I) versus log $|\mathbf{q}|$. Values of α between 1 and 3 correspond to a mass fractal (i.e. aggregates of particles). At high q, the power-law data are related to surface properties. For rough particles the slope parameter α varies between 3 and 4, where $\alpha = 4$ when particles have fully smooth surfaces and α being close to 3 for those having a highly rough surface area.

The investigation of how the hydride material is organized spatially within the pores of the scaffold is necessary for a better understanding of the nanocomposite systems. The present work concerns SANS studies of $Mg(^{11}BD_4)_2$ and $NaAlD_4$ particles confined by a nanoporous template.

2. EXPERIMENTAL DETAILS

The investigated samples are $Mg(^{11}BD_4)_2$ infiltrated in pre-treated activated carbon (sample labelled $Mg(^{11}BD_4)_2$/AC1), following a wet impregnation procedure [8, 13], and $NaAlD_4$ in activated carbon fibers (sample labelled $NaAlD_4$/ACF25), prepared following a melt impregnation procedure [14]. The respective bulk powders, $Mg(^{11}BD_4)_2$ and $NaAlD_4$, were also investigated. The deuterated version of the hydrides were employed in order to obtain good contrast and low incoherent background in the SANS experiments.

Samples were always kept under protective atmosphere and handled either in a glove box or by applying standard Schlenk techniques.

The SANS experiments were carried out at the JEEP II reactor at IFE, Kjeller, Norway. The *q*-range employed in the experiments was 0.008 to 0.25 $Å^{-1}$. The samples were filled in 1 mm Hellma quartz cuvettes under argon atmosphere. For all samples it was ensured that the transmission was sufficiently high (> 90%) to disregard multiple scattering. Standard reductions of the scattering data including transmission corrections were conducted by incorporating data collected from an empty cell, beam without cell and blocked-beam background. The data were transformed to an absolute scale (coherent differential cross section ($d\Sigma/d\Omega$)) by calculating the normalized scattered intensity from direct beam measurements [15].

3. RESULTS AND DISCUSSIONS

X ray diffraction was not useful to study the infiltrated system considered in this work because of the complete disappearance of the diffraction peaks compared to the bulk $Mg(^{11}BD_4)_2$ or $NaAlD_4$ [13, 14]. Therefore the use of SANS has an invaluable importance to extract information on the prepared nanocomposites.

Figure 1 displays SANS data at room temperature (RT) of the $Mg(^{11}BD_4)_2$ infiltrated powders compared with the scattering from the bulk $Mg(^{11}BD_4)_2$ and the scaffold alone. $Mg(^{11}BD_4)_2$/AC1 sample scatters strongly than the scaffold alone or the bulk. Furthermore, there is a crossover between the two latter just below 0.02 $Å^{-1}$. Below this *q*-value the bulk sample shows a relatively steep rise of the SANS intensity, indicating a significant amount of large particles for the bulk sample.

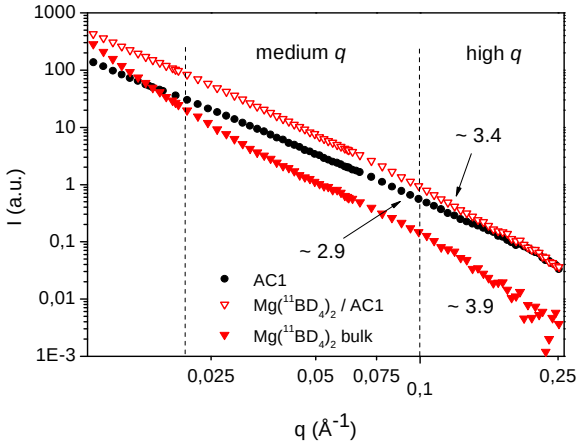

FIG. 1. SANS measurements at RT on AC1, $Mg(^{11}BD_4)_2$/AC1, and bulk $Mg(^{11}BD_4)_2$.

It is possible to distinguish two more regions in Figure 1: the middle *q* range, defined between the two dotted bars (0.02 $Å^{-1}$ < *q* < 0.1 $Å^{-1}$), and the high *q* range (above 0.1 $Å^{-1}$). As evidenced from the measured high *q* slopes (2.9) the scaffold alone has an open structure even at the smallest length scales, that is a mass fractal behaviour. On the other hand, when the scaffold is loaded with Mg-borohydride, the measured slope increases to 3.4, showing the conversion to a surface fractal regime, where a majority of the pores have been filled. The size distribution (volume distribution) obtained by means of an indirect Fourier transform performed on $Mg(^{11}BD_4)_2$/AC1 confirms the small dimensions of the obtained hydrides particles, in the range between 1 and. 6 nm (10 to 60 Å) [16]. This result is in very good agreement with the characteristic feature at about 4 nm found with our preliminary interpretations of the SANS data [13].

The combination of SANS and *in situ* small-angle X ray scattering (SAXS) on the infiltrated $Mg(^{11}BD_4)_2$ and the bulk alone has been used [16] in order to gain information about the material behaviour during heating up to 400 °C. The data indicates that when infiltrated into the scaffold there is negligible reduction/modification in particle sizes with temperature [16]. The only detectable changes, measured at high *q*, are localized on the surface of the particles which becomes rough during heating. In the case of the bulk, instead, the powders showed significant changes of both particles size and surface morphology under the same conditions [16].

Figure 2 shows SANS data of the composite $NaAlD_4$/ACF25, the scaffold alone, as well as the bulk $NaAlD_4$. The bulk material behaves quite differently compared to the composite, in particular the scattering intensity of $NaAlD_4$ is higher at low and intermediate *q*-values, showing that in the bulk the average particles size is significantly larger than in the composite. While the composite and the scaffold follow the same behaviour at low *q*, some alterations are present above 0.03 $Å^{-1}$, where there is an excess scattering from the composite compared to the scaffold alone. The size distribution obtained by means of an indirect Fourier transform of the excess scattering confirms the small sizes, well below 5 nm, of the $NaAlD_4$ particles when they are integrated into the scaffold [14].

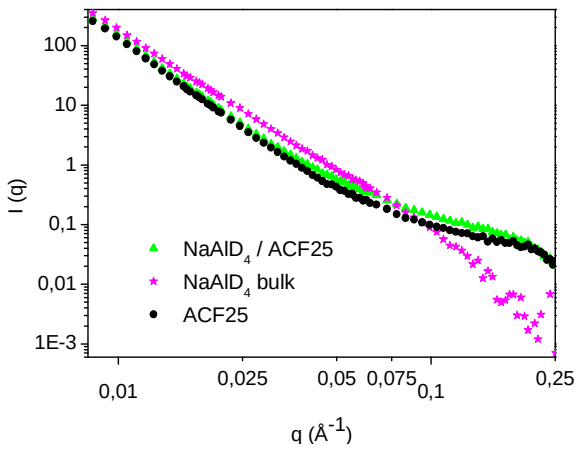

FIG. 2. SANS measurements at RT on ACF25, $NaAlD_4$/ACF25, and bulk $NaAlD_4$.

In situ SAXS data were also collected on the composite, on the scaffold alone, and on the bulk $NaAlD_4$ [14]. The data suggested that the integration into the scaffold of sodium alanate stabilize the size of the particles upon heating, while the particles of the bulk powders undergo changes under the same conditions [14]. The slope parameter of the composite remains constant upon heating to 290 °C, with values of $\alpha \sim 2.3$ at central and at high *q* [14].

The fact that we do not reach the surface fractal regime in the high *q*-range (i.e. α between 3 and 4) is an indication of the small structures present in the composite, which behaves like a mass fractal system even to the smallest length scales accessible with SANS, i.e. around 1 nm.

4. CONCLUSIONS

The study resulted in the direct measurements of the successful nanoscale infiltration of hydrides in carbon scaffolds. The Mg-borohydride particles infiltrated in activated carbon have been estimated by SANS measurements to have a distribution of particles size in the range of 1-6 nm. During the heating treatment it was observed that the nano-confined particles maintained their size distribution and the decomposition affected only the morphology of the particle surface. Similar measurements on bulk powders of $Mg(^{11}BD_4)_2$ showed significant modification of both particles size and surface morphology.

The use of small-angle scattering on nanoconfined $NaAlD_4$ has also provided important information on the characteristics of this hydride. When infiltrated, the particles size of the hydride has been estimated well below 5 nm. Furthermore, the integration into a supporting carbon scaffold has a remarkable stabilizing effect on the morphology of the $NaAlD_4$ nanoparticles.

REFERENCES

[1] EASTMAN, J. A., et al., Phys. Rev. B 48 (1993) 84.
[2] WEISSMUELLER, J., et al., Phil. Mag. Lett. 80 (2000) 411.
[3] ZUETTEL, A., et al., Appl. Surf. Sci. 162/163 (2000) 571.
[4] PUNDT, A., Adv. Eng. Mater. 6 (2004) 11.
[5] YAMAUCHI, M., et al., J. Phys. Chem. C 112 (2008) 3294.
[6] VAJO, J. J., et al., Scr. Mater. 56 (2007) 829.
[7] ZHANG, Y., et al., Int. J. Hydrog. Energy 32 (2007) 3976.
[8] FICHTNER, M., et al., Nanotechnology 20 (2009) 204029.
[9] LOHSTROH, W., et al., Chem. Phys. Chem. 11 (2010) 789.
[10] BALE, H. D., et al., Physical Review Letters 53 (1984) 596.
[11] SCHMIDT, P. W., J. Appl. Cryst. 24 (1991) 414.
[12] SCHMIDT, P. W., "Modern Aspects of Small-Angle Scattering", Kluwer Academic Publishers, Netherlands (1995) 1-56.
[13] SARTORI, S., et al., Nanotechnology 20 (2009) 505702.
[14] SARTORI, S., et al., submitted I (2010).
[15] WIGNALL, G. D., et al., J. Appl. Cryst. 20 (1987) 28.
[16] SARTORI, S., et al., submitted II (2010).

NEUTRON DIFFRACTION STUDIES OF METAL HYDRIDES ALLOYS FOR HYDROGEN STORAGE

J. HUOT
Physics Department and Hydrogen Research Institute, Université du Québec à Trois-Rivières
3351 des Forges, Trois-Rivières, Québec
Canada
jacques.huot@uqtr.ca

Abstract: In this paper we present results obtained from two different classes of metal hydrides. First, we will discuss the effect of ball milling on the hydrogen storage properties of magnesium hydride. High energy milling of MgD_2 produces a nanocrystalline structure made of a mixture of β-MgD_2 and the high temperature/high pressure phase γ-MgD_2. Neutron powder diffraction showed that the ball-milled β-MgD_2 and γ-MgD_2 structures are distorted compared to the same phases synthesised at high-pressure and high temperature. The Mg-D bond lengths are modified in β-MgD_2. In γ-MgD_2 phase, only one bond length is changed. This may be the explanation for the limited amount of γ-MgD_2 synthesized by energetic ball milling. The second case is the crystal structure of a new class of metal hydrides, the so called 'Laves phase related BCC solid solution'. From neutron diffraction, we found that two phases are present in the as-cast alloy $TiV_{0.9}Mn_{1.1}$. One is a BCC solid solution, the other is a C14 Laves phase. We found that in the C14 phase there is a preferential site for titanium atoms while the vanadium and manganese atoms are distributed on the other two sites.

1. INTRODUCTION

Metal hydrides are attractive candidates for a safe way of storing hydrogen for a broad range of practical purpose such as portable, mobile or static applications. However, more research is needed in order to develop metal hydrides that meet all the industry requirements. For example magnesium hydride has a high hydrogen storage capacity (7.6 wt.%) but its temperature of operation is too high for most applications. In the case of body cubic centered (BCC) alloys such as Ti-V-Mn and Ti-V-Cr they have relatively low reversible capacities (a few wt.%) but their temperature of operation near room temperature makes them attractive for some applications if their cost could be reduced.

For metal hydrides development, neutron diffraction is an important tool because it allows the localization of the atoms in the crystal structure, especially hydrogen (deuterium). In this review we will show two examples of the use of neutron diffraction in the development of new metal hydrides. First, we will discuss the appearance of the metasable γ-MgH_2 in ball milled magnesium hydride and propose a mechanism for its formation. Secondly, the crystal structure of $TiV_{0.9}Mn_{1.1}$ alloy is presented. Neutron diffraction showed that this alloy is a mixture of C14 and BCC phases and that the C14 phase has preferential site for titanium atoms.

2. EXPERIMENTAL DETAILS

Powder neutron diffraction experiments were performed at room temperature on the C2 DUALSPEC high-resolution neutron powder diffractometer at Chalk River with a 800 multiwire detector spanning 80° 2θ. The monochromator was a planar Si (531) giving a wavelength of 1.3287 Å. For magnesium hydride samples, the sample holder was a cylindrical can made of vanadium (diameter 0.5 cm, height 7 cm). For $TiV_{0.9}Mn_{1.1}$ alloy, the measurement was performed on as-cast button wrapped with platinum foil which served as an internal standard for lattice parameters calculation. The data were measured with two positions of the detector, one from 5-85°, and a second from 30-110°.

3. MAGNESIUM HYDRIDE

It is known that under high pressure and temperature (2.5-8 Gpa and 250-900°C) a metastable orthorhombic high-pressure magnesium dihydride (γ-MgH_2) coexists with the tetragonal β-MgH_2 phase[1, 2]. This structure could also be synthesized by high energy ball milling[3]. In order to understand the formation mechanism of γ-MgH_2 phase by ball milling we compared the γ-MgH_2 phase synthesized by ball-milling with the structure of γ-MgH_2 made by high pressure and temperature reported by Bortz et al. [4].

Deuterated magesium powder was milled for 20 hours in a Spex 8000 model shaker mill with a vial and balls of stainless steel. Neutron diffraction was performed at room temperature on the C2 DUALSPEC high-resolution neutron powder diffractometer at Chalk River. Experimental details on neutron measurement and sample preparation are given in Ref. [5]. Rietveld refinement was performed by using the FULLPROF software [6].

Figure 1 shows the observed, calculated and difference neutron diffraction patterns of ball milled MgD_2. The peaks were broad due to the nanocrystalline nature of the sample. Magnesium oxide and hydroxide were produced by reaction of ball milled magnesium dihydride when exposed to the air. The incoherent diffraction of hydrogen gave the high background showed by the diffraction pattern.

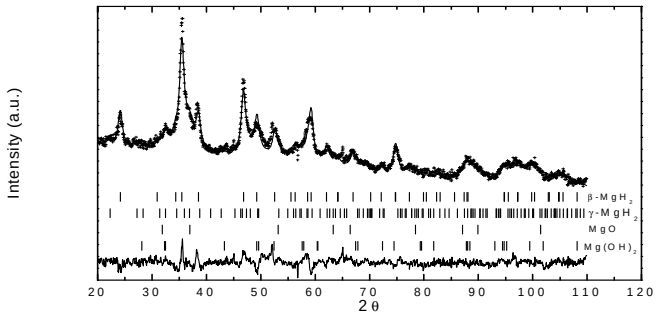

FIG. 1. Neutron powder diffraction of 20 hours milled nanocrystalline MgD_2. (crosses: experimental intensity, upper solid line: calculated intensity, lower line: residue).

The phase abundance of β-MgD_2, γ-MgD_2, MgO, and $Mg(OH)_2$ were respectively 32wt.%, 14wt.%, 36wt.%, and 18wt.%. Both β-MgD_2 and γ-MgD_2 had a slightly altered lattice parameters compared to ref [4]. The atomic positions also experienced a variation. The reason for such a variation could be understood by examination of the bond length. In table 1, we present the D-Mg bond length in ball-milled MgD_2 compared to high-pressure high temperature synthesised MgD_2 (ref [4]). For the β □phase one bond length is stretched while the other one is compressed by the same amount. In the γ-MgD_2 structure two bond lengths variation are small and one is highly stretched compared to the γ phase synthesised at high temperature and pressure.

TABLE 1. DEUTERIUM-MAGNESIUM DISTANCES (IN Å) IN MGD_2. THE VALUES IN PARENTHESES ARE THREE STANDARD DEVIATIONS AND REFER TO THE LAST DIGIT

Phase	High temperature- high pressure Ref [4]	Ball-milled/This work	Variation (%)
β-MgD_2	1.9351(9)	1.915(4)	-1.0
	1.9549(6)	1.976(5)	1.1
γ-MgD_2	1.915(3)	1.92(2)	0.3
	1.943(3)	1.93(2)	-0.7
	2.004(3)	2.04(2)	1.8

In Ref. [4], the authors pointed out that for the pressure induced $\beta \Rightarrow \gamma$ phase transition, bonds are broken and re-established. When magnesium hydride is ball milled, it seems that in β phase the bond length are symmetrically stretched and compressed by about 1%. A possible explanation of the appearance of γ phase upon ball milling is that higher strain could probably not be accommodated in β phase and the strain is relaxed by a phase transformation to γ phase. The stress field may act as the driving force for the $\beta \Rightarrow \gamma$ phase transition in the ball-milled material.

4. $TiV_{0.9}Mn_{1.1}$ ALLOY

Solid solution BCC alloys (mainly Ti-V-Mn and Ti-V-Cr based) are promising hydrogen storage materials because of their relatively high storage capacity and their ability to absorb and desorb hydrogen in ambient conditions [7]. Recently, we reported the study by neutron diffraction of the crystal structure of the multiphase alloy $TiV_{0.9}Mn_{1.1}$ [8]. Refinement of the neutron pattern of an alloy with $TiV_{0.9}Mn_{1.1}$ composition is difficult because, the scattering cross section of Ti and Mn are almost the same, making them hard to distinguish with neutron radiation. Moreover, vanadium is difficult to locate because of its small cross section. Despite these disadvantages, a good quality neutron diffraction pattern could give precise information about the crystal structure. Using high exposure time a workable neutron diffraction pattern could be collected [9]. In this investigation, the Rietveld analysis of the pattern was carried out using the softwares EXPGUI [10] and GSAS [11].

In Fig. 2 we present the Rietveld analysis of the neutron diffraction pattern of arc melted $TiV_{0.9}Mn_{1.1}$. The residue curve is small, indicating a good fit of the pattern as confirmed by the weighted difference between the calculated and measured intensities of R_{wp}=5.67%. Rietveld refinement confirmed the presence of C14 and BCC phases but also of a small amount of titanium. No oxides phases were observed.

In table 2 the identified phases (beside platinum which was added as internal standard) are displayed along with their respective phase abundance and lattice parameters. The phase identified as C14 is a member of the so-called ‘Laves phases’ structures.

The appearance of this C14 Laves phase is expected because, as pointed out by Akiba and Iba [7], these new BCC alloys have a nominal AB_2 composition and are closely related to Laves phases. In our Rietveld analysis the atomic occupancy and position in the C14 phase were refined. Atomic positions are noted by using the Wyckoff notation. The Wyckoff symbol describe the special positions of the space group, beginning with *a* for the highest symmetry. For the C14 structure, position 2*a* is (0,0,0), 4*f* is (1/3,2/3,z), and 6*h* is (x,2x,1/4). In table 3 the refined parameters for the C14 phase are shown.

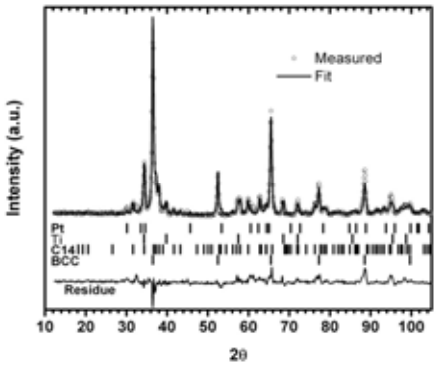

FIG. 2. Neutron diffraction pattern and Rietveld refinement of $TiV_{0.9}Mn_{1.1}$. The short vertical bars indicate the position of Bragg peaks. The bottom curve is the difference between experimental and calculated pattern.

TABLE 2. CRYSTAL STRUCTURES OF $TiV_{0.9}MN_{1.1}$ AS DETERMINED FROM RIETVELD REFINEMENT. THE VALUES IN PARENTHESES ARE THREE STANDARD DEVIATIONS AND REFER TO THE LAST DIGIT

Phase	Space Group	Abundance (%)	Lattice parameters (Å)
C14	P 6_3/mmc	32 (4)	a =4.906(3) c = 8.011(9)
BCC	I m -3 m	65 (1)	a =3.018(1)
Titanium	P 6_3/mmc	3 (1)	a =2.971(5) c = 4.63(1)

TABLE 3. CRYSTALLOGRAPHIC PARAMETERS OF THE C14 PHASE IN $TiV_{0.9}MN_{1.1}$ AS DETERMINED FROM RIETVELD REFINEMENT OF NEUTRON DIFFRACTION PATTERN

Site (Wyckoff symbol)	Refined Coordinates	Atoms	Occupancy
2a	-	Mn	0.65
	-	V	0.35
4f	z = 0.065	Ti	1.0
6h	x = 0.82356	Mn	0.58
		V	0.42

Rietveld refinement proved that titanium atoms are localized exclusively on the 4*f* site while the manganese and vanadium atoms are distributed on the 2*a* and 6*h* sites but with a different abundance. These abundances give a stoichiometry of $TiV_{0.8}Mn_{1.2}$ for the C14 phase. It should be pointed out that TEM-EDX measurements gave for the C14 phase a higher proportion of manganese atoms than nominal composition [8]. Therefore, it may be concluded that for this system C14 phase has a better affinity for manganese atoms than for vanadium.

5. CONCLUSIONS

Neutron diffraction is a unique and powerful tool for the structure characterization and the localisation of hydrogen (deuterium) atoms. In the case of ball milled magnesium hydride powder neutron diffraction showed that strain relaxation could be a possible explanation for the β-$MgD_2 \Rightarrow \gamma$-MgD_2 transition. Neutron diffraction of $TiV_{0.9}Mn_{1.1}$ alloy confirmed that the arc melted alloy was formed by a C14 and a BCC phases. In the case of C14, titanium atoms occupy the 4*f* site while on the two other sites there is a higher proportion of manganese than vanadium. Neutron diffraction played a crucial role in the understanding of metal hydrides and will remain a privileged tool for the development of new metal hydrides for practical applications.

REFERENCES

[1] BASTIDE, J.P., BONNETOT, B., LÉTOFFÉ, J.M., CLAUDY, P., Mater. Res. Bull. **15** (1980) 1215.

[2] NAYEB-HASHEMI, A.A., CLARK, J.B., eds. Phase Diagrams of Binary Magnesium Alloys, Monographs Series on Alloy Phase Diagrams, 1988, ASM International: Metals Park, Ohio. 370.

[3] HUOT, J., LIANG, G., BOILY, S., VAN NESTE, A., SCHULZ, R., J. Alloys Comp. **293-295** (1999) 495-500.

[4] BERTHEVILLE, B., FISCHER, P., YVON, K., J. Alloys Comp. **287** (1999) L4-L6.

[5] HUOT, J., SWAINSON, I., SCHULZ, R., Ann. Chim. Sci. Mat. **31** (2006) 135-144.

[6] RODRIGUEZ-CARVAJAL, J., in Abstracts of the Satellite Meeting on Powder Diffraction of the XV Congress of the IUCr. 1990. Toulouse, France.

[7] AKIBA, E., IBA, H., Intermetallics **6** (1998) 461-470.

[8] HUOT, J., ENOKI, H., AKIBA, E., J. Alloys Comp. **453** (2008) 203-209.

[9] HUOT, J., CRANSWICK, L., SWAINSON, I., Physics in Canada **62** (2006) 289-294.

[10] TOBY, B.H., J. App. Cryst. **34** (2001) 210-213.

[11] LARSON, A.C., DREELE, R.B.V., General Structure Analysis System (GSAS) (1994), Los Alamos National Laboratory: Los Alamos.

PERFORMANCE CHARACTERIZATION OF SOLID STATE HYDROGEN STORES BY NEUTRON DIFFRACTION AND PAS METHODS

E. WEIDNER[1], A. ZEMAN[2], D.J. BULL[3], F. DOLCI[4], M.F.T. TELLING[5], T. HANSEN[6], M. HOELZEL[7], P. MORETTO[1]

[1]Cleaner Energy Unit, European Commission DG-JRC, Institute for Energy, Petten, NL

[2]NAPC Physics Section, International Atomic Energy Agency, Vienna

[3]Institute for Materials Research, University of Salford, Salford, UK

[4]Institute for Nanotechnology, FZ Karlsruhe, Germany

[5]ISIS Facility, Rutherford Appleton Laboratory, Chilton, Didcot, UK

[6]Institut Laue Langevin, Grenoble, France

[7]FRMII, TU Darmstadt, Germany

eveline.weidner-ronnefeld@ec.europa.eu

Abstract: In situ neutron diffraction is a useful tool for understanding the reaction pathway in solid hydrogen storage materials. Especially the combination of the Sievert technique for determining the amount of hydrogen absorbed while recording diffraction patterns can help clarify the mechanisms involved. Microstructural changes occuring during cycling with hydrogen can be investigated by Positron Annihilation Spectroscopy (PAS) an X ray Diffraction (XRD) method, whereby the formation of several types of defects can be determined.

1. INTRODUCTION

The Institute for Energy of the JRC focuses its hydrogen and fuel cell related work on pre-normative research covering the development and improvement of test, performance characterization and numerical simulation methods in the areas of hydrogen storage (gaseous and solid state), hydrogen sensors, fuel cell systems, and hydrogen safety. To underpin this pre-normative research, IE also performs more basic research in some selected topics such as application of nuclear methods for characterization of storage materials. These activities are in part carried out in collaboration with international partners under FP6 NESSHY project. Recent experiments performed at ILL, FRMII and ISIS revealed deviations from published reactions paths in the Li and Li-Mg imide/amide systems. A project investigating the microstructural changes during long term cycling of Al-doped $LaNi_5$ utilised the PAS (positron annihilation spectroscopy) capabilities at JRC Petten. Thereby the formation of microstructural of defects and their dependence on the Al content could be determined.

2. IN SITU NEUTRON DIFFRACTION EXPERIMENTS

In situ neutron diffraction is a powerful tool for understanding the hydrogen absorption/desorption process by directly observing the complex reaction mechanisms involved in the hydrides formation/decomposition. As it is also possible to determine the position of the hydrogen atoms in crystal structures, neutron methods are uniquely suitable for studies of hydrogen storage materials.

EXPERIMENTAL

2.1 Sieverts' technique

To perform in situ measurements at neutron sources during hydrogen ab- and desorption, a portable Sieverts' type apparatus was developed. This enables the quantification of the amount of hydrogen/deuterium absorbed or released by the sample material. Deuterium gas is used for neutron diffraction experiments in preference to hydrogen owing to its favourable coherent to incoherent scattering ratio.

Hydrogen uptake characteristics are often shown as pressure-composition isotherms, most commonly the amount of hydrogen absorbed or desorbed is measured via Sieverts' or gravimetric techniques. For a Sieverts' type measurement, hydrogen pressure is increased or decreased in steps. As the volume and temperature of the system are known, the number of moles of hydrogen atoms absorbed or desorbed by the sample can be calculated from the change in the pressure. The hydrogen content of the sample can therefore be determined for each step. The portable Sievert's apparatus consists of several calibrated volumes, three pressure measuring devices for different ranges, connecting tubing, valves and sample holder. These parts are mainly 316L type stainless steel, which can withstand high hydrogen pressures.

Several types of pressure cells for the sample are employed depending on the geometry of the diffraction instrument and the pressure range of the experiment. At ISIS, the sample is contained in a steel pressure cell with a vanadium window, coated in 2-5 microns of Al_2O_3, acting as a permeation barrier to hydrogen. The sample material is placed in a ceramic boron nitride cup, the steel part of the sample cell is shielded by gadolinium foil. This ensures that only the sample contributes to the measured signal. The maximum pressure rating is 5 bars. Further details of the cell can be found in [1]. For the ILL and FRM II experiments, which were performed at much higher pressures, the sample holders were produced either from a specific type of Inconel (754), which does not activate in a neutron beam, or stainless steel. The material for the sample holder has to be able to withstand both high pressures and temperatures, but not have high absorption of neutrons or produce a strong or complex diffraction pattern itself. This constraint does not leave many options, to our knowledge. Based on Barlow's formula ($P = 2\ s\ t/((d_o - 2\ t)\ SF)$, the wall thickness ($t$), for a pressure rating of 150 bar with a safety factor (SF) of 2, can be as low as 0.25-0.5 mm for a tube of 10 mm outside diameter (d_o) for materials with high yield strength (s).

2.2. Neutron sources

Neutron diffraction measurements were performed at three different neutron sources. The ISIS facility is a spallation source, therefore a time-of-flight technique is utilised for the measurements at the OSIRIS instrument. Incident wavelengths are selected from the Maxwellian distribution, peaked at about 4 Å, emanating from a liquid hydrogen moderator by two disk choppers running at 25 Hz. The relative phasing of the choppers allows different wavelength bands to be selected; d-spacing ranges of a width of about 2 Å can be measured for a given chopper phasing. Thus, obtaining a diffraction pattern over an extended d-spacing range requires a sequential series of measurements at a number of different chopper phasings. Data sets are corrected for wavelength dependent effects and merged, where required, using the standard ISIS diffraction data processing software ARIEL. Owing to the rapid data collection rate on OSIRIS, a pattern for a given d-range can be collected in the order of a minute, offering the possibility of recording multiple diffraction patterns as the system relaxes to equilibrium, yielding a time resolved picture. Full profile refinement is performed using the Rietveld method, implemented in the General Structure Analysis System (GSAS) software [2]. A time-of-flight profile function comprising a convolution of a back-to-back exponential with a pseudo-Voigt function was employed.

Neutron diffraction measurements were also performed on the D20 instrument at the Institute Laue Langevin reactor source, Grenoble, France. This instrument provides high flux and a curved linear position sensitive detector (PSD) resulting in rapid data acquisition over the full angular coverage. With the selected wavelength of 2.42 Å, a d-spacing range of about 10 Å to 1.4 Å was obtained. Time resolved diffraction with a resolution of one minute was possible.

Data sets were corrected for detector efficiency against a vanadium standard, using the standard ILL data processing software LAMP[3]. A super-gaussian peak shape, in particular for high intensity reflections, causes some difficulties in accurately modelling the profile shape. Profile refinement is performed using the Rietveld method with the software package FULLPROF [4].

The third experiment took place at the SPODI instrument at Forschungsreaktor Muenchen (FRM II). The instrument provides diffraction patterns with excellent profile shape and high resolution over a wide 2θ scattering angular range. Thus it is suited for structure refinement on complex systems, in particular phase mixtures. On the other hand, the stepwise movement of the detector array lowers the efficiency and limits the possibilities for time resolved studies.

High flux reactor Petten (HFR) offers the possibility of performing neutron diffraction, small angle neutron scattering and neutron radiography experiments. As the reactor was not operational during much of this projects running time, no measurements were performed there. The instrument HB5 is a combined powder and stress diffractometer. The relatively high flux of $10^{10}m^{-2}s^{-1}$ at 2.5 Å would enable measurement even of small sample quantities. The point detectors, however, make kinetic experiments all but impossible as long measurement times are necessary. An angular range of -2 to155° 2θ with a step size of 0.05° is accessible. Different sample environments are easily installed.

2.3. Sample material

The starting material of Li_3N is synthesised by the reaction of molten alkaline earth metal-sodium alloys with dried nitrogen at 460°C. The cleaned lithium metal (Alfa 99+%) is added to molten sodium (Aldrich 99.5%) in an argon filled glove box and then heated in a stainless steel vessel under nitrogen for 48 hours. The identity of the product was confirmed as Li_3N by powder X ray diffraction. Deuterium (99.8%, BOC Special Gases) dosing is made by Sieverts' method.

The starting material $Li^2Mg(NH)^2$ was prepared by ball milling for 12 h under argon atmosphere a 2:1 molar mixture of $LiNH_2$ and MgH_2 (Sigma-Aldrich) with a powder to ball ratio of 1:20. A Fritsch P6 planetary ball mill was used. Revolution speed was set to 600rpm. A silicon nitride vial and balls were used. The obtained powder was cycled 3 times at 220°C in a Sieverts' apparatus using a 95 bar deuterium pressure for absorption and a 1 bar deuterium pressure for desorption in order to obtain the deuterated material ($Li_2Mg(NH)_2$).

2.4 Results

Information on the rate-limiting step during the hydrogenation reactions in imide/amide was gained through structural and kinetic studies possible at high intensity neutron sources. The combination of two techniques, Sieverts' and diffraction methods is vital to the understanding of the reaction paths in many systems where complex reactions occur, for example via non-stoichiometric compounds and intermediate reactions. Recent experiments performed at ILL, ISIS and FRMII revealed deviations from published reactions paths in the Li [5, 6] and Li-Mg imide/amide [7] systems.

Figure 1 shows a diffraction pattern recorded at a deuterium content of $0.6D/Li_3N$. The phases present are not those expected from the reaction proposed by Chen et al. [8]. The appearance of non-stoichiometric compounds may help explain the sluggish kinetics and limited reversibility in the Li-N-H system [6].

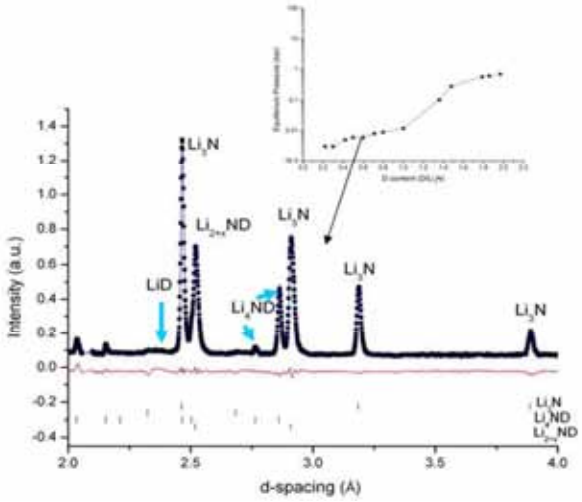

FIG. 1. Diffraction pattern recorded at 0.6D/Li_3N content. The arrows indicate reflection positions of the phases either absent (LiD) or present (Li_4ND) contrary to the published reaction path. The non-stoichiometric phase $Li_{2+x}ND$ is formed instead of Li_2ND. The inset shows the PCI curve simultaneously obtained by the in situ method.

Combining the results obtained at high-intensity (D20/ILL) and high-resolution (SPODI/FRMII) instruments enabled a time resolved investigation of the reaction path in the Li-Mg-N-D system and clear identification of the phases forming during hydrogen absorption. A qualitative comparison of the two instruments, D20 and SPODI is shown in Fig. 2, where the diffraction pattern for comparable sample material and deuterium content is given. The higher resolution offered by the second instrument comes at cost of intensity therefore kinetic measurements are not possible.

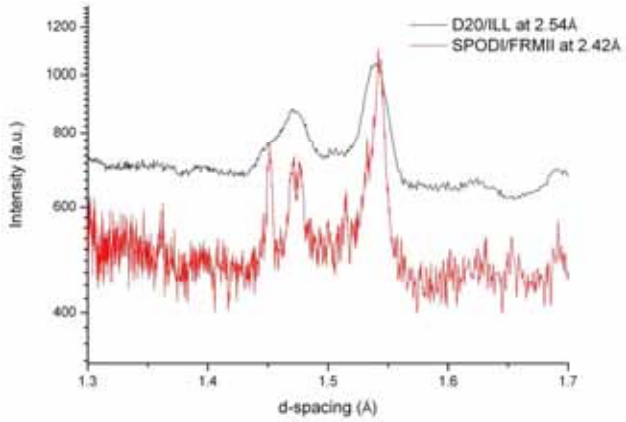

FIG. 2. Qualitative comparison of diffraction patterns collected at two different instruments for similar sample material. The higher resolution data (red line) shows a high degree of noise, however, reflections are more clearly separated.

Key information could be gained from the second experiment as the reflection overlap from phases with similar lattice parameters is greatly reduced (Fig. 2). The experiment performed at D20/ILL on a mixture of Mg-amide and Li-deuteride revealed that an intermediate reaction occurs via three stoichiometric phases, the phase abundances calculated from Rietveld refinements indicate that one of these phases may be very stable and therefore slow to react [7].

3. MICROSTRUCTURAL CHARACTERIZATION BY POSITRON ANNIHILATION SPECTROSCOPY

The $LaNi_5$ intermetallic compound is a well-known hydrogen storage alloy able to absorb near atmospheric pressure at room temperature. In the phase equilibrium of $LaNi_5$–H_2 system, the α phase (solid solution) and the β phase (hydride) are formed. Hydrogen absorption and desorption cycling has two main effects on LaNi type intermetallic compounds: defect generation and pulverization. Both can have a profound influence on the properties of those compounds regarding the capacity (cycling properties) and kinetics. Capacity loss can be due to defects and pulverization as defects lead to amorphisation. Breakup or 'decrepitation' is attributed to the strains in $LaNi_5$ during hydriding (5–7%). The elastic limit of $LaNi_5$ is below 1% [9]. The breakup of the $LaNi_5$ into smaller particles will provide a larger surface-to-volume ratio, offering more reaction sites for corrosion. Alloying the $LaNi_5$ can stabilize it against corrosion and disproportionation reactions. Lattice defects such as vacancies and dislocations have been observed after the absorption and desorption processes of hydrogen in $LaNi_5$. TEM observations, X ray and neutron diffraction measurements have shown that dislocations with a remarkably high density of 10^{11}–10^{12} cm^{-2} are formed in $LaNi_5$ during the first cycle of hydriding [10, 11]. The defect generation in hydrogen cycled $LaNi_5$ and Al substituted derivatives were studied in by analysis of the X ray line broadening and positron lifetime spectroscopy.

3.1 Experimental

A series of three hydrogen-absorbing intermetallic alloys were purchased from Lab. Tech., a Bulgarian company specialising in hydrogen storage technology. The compositions of the materials are $LaNi_{5-x}Al_x$, where x = 0.1, 0.3 and 0.5 wt% nominally. Ingot pieces were milled under Ar for 1 h at 42°C, 300 rpm, in a stainless steel vial. Annealing was performed under purified Ar at 950°C for 5hr, the samples were then activated by 10 soak and release cycles under 20 bar H_2 pressure at 40°C. Cycling consisted of 750 absorption & desorption runs.

Phase abundances, crystallite size and lattice strain were determined by powder X ray diffraction (XRD), carried out on a SIEMENS 5005 diffractometer with CuKα radiation. About 2.7 g of $LaNi_{5-x}$ Al_x powder were used as samples for the positron annihilation lifetime spectroscopy. A ^{22}Na radioactive source was utilised for measurements at RT with BaF_2 detectors with a system resolution of 200 ps and a count rate of $2x10^5$ per second.

3.2. XRD results

Using Rietveld analysis, strain, and crystallite size can be calculated from the width of diffraction peaks. After cycling with hydrogen, LaNi5 shows anisotropic peak broadening, this broadening, however, is reduced in compounds where Ni is substituted by elements such as Al and Sn. The broadening is caused by defects introduced by the cell expansion on the transition from the solid-solution to the hydride phase. TEM analysis has revealed a dense dislocation structure [12]. The XRD peak shape can be modelled and, by application of Krivoglaz theory [13] related to a slip system and dislocation density, Fig. 3. In addition, because of expansion and contraction, 'particles' of the alloys are broken into much smaller pieces than those before hydrogenation. The crystallite size can also be determined by analysis of the profile shape.

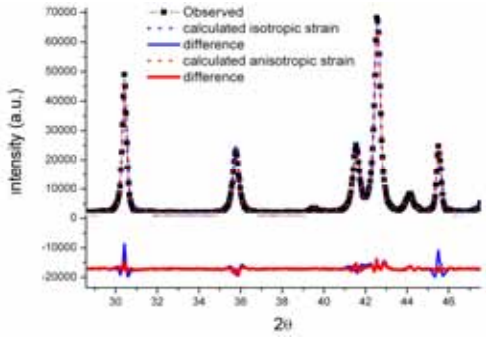

FIG. 3. Comparison of Rietveld full profile refinement of a cycled $LaNi_{4.93}Al_{0.07}$ sample assuming isotropic (blue) and anisotropic (red) strain.

The diffraction profiles were analyzed by Rietveld refinement program Fullprof [4]. For the calculation of the anisotropic parameters of the microstrain, a general function D_{ST} is introduced. The two parameters of the broadening function $D_{ST,}$ S_{aa} and S_{cc} (assuming anisotropic gaussian microstrain along the a (S_{aa}) and c (S_{cc}) lattice parameters) are proportional to local fluctuations of the lattice parameters around their mean values. S_{aa} and Scc allow modelling of broadening of hk0 and 00l reflections, respectively [14]. Pure anisotropic broadening can be related to high S_{aa} values and high densities of basal slip systems. In Fig. 4 the effect of Al addition can be observed, as the high anisotropy of the strain is reduced, and the overall strain much lower with increasing Al content. The results indicate that Al addition reduces strain introduced by cycling. The crystallite size for cycled samples with high Al content at 4000 Å is larger than that of 1200 Å for material with low Al content. Phase abundances can be obtained by Rietveld analysis, and therefore the disproportionation reaction monitored. The minority phases are Ni and Ni_3Al. The quantity of the Ni_3Al phase increases with increasing Al content, however, the amount of this phase appears to be stable during cycling. The amount of a pure Ni phase is reduced with increasing Al addition.

The proposed effect of Al addition of preventing the disproportionation reaction, pulverisation and introduction of defects is therefore supported by XRD data.

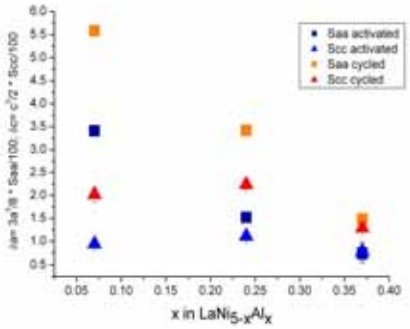

FIG. 4. Effect of Al addition on δa and δc, where $\delta a = 3a^3/8*Saa/100$ and $\delta c = c^3/2*Scc/100$.

3.3. PAS results

The microstructural changes during long term cycling of Al-doped $LaNi_5$ were analysed by the PAS method at JRC Petten. A PAS spectrum can be described as a decay curve, $y(t)$, formed by a number of exponential decay components each with a different intensity and lifetime (I_i,τ_i), convoluted with the instrumental resolution of the detection system (R) and subject to experimental noise (B):

$$y(t) = R(t) \otimes \sum I_i \, e^{-t/\tau_i} + B_i \quad (1)$$

The positrons annihilating in a perfect lattice must decay exponentially and the positron lifetime spectrum can be described by single parameter tau. However in real conditions, lifetime spectrum should be deconvoluted to several sub-components. Typically, two-component analysis is performed, when first parameter Tau 1 with intensity I_1 characterize the basic bulk structure of studied sample, while second component Tau 2 and its intensity I_2 is assigned to the defects present in the structure. It is important to note that conventional lifetime setup without moderated positrons is recognised as bulk-type technique and gives information from the whole region where positrons are penetrated. This, of course, depends on the density of the studied materials as well as the type of positron source (median energy). In the case of a ^{22}Na positron source, the maximum penetration depth would be at the level of 100-500 micrometers for metal samples.

The analysis of positron annihilation spectra confirmed that $LaNi_{5-x}Al_x$ intermetallic compounds are sensitive to the process of hydrogen absorption and desorption, which causes microstructural changes [15]. The positron is a unique probe to study the behaviour of protons in hydrogen-absorbing materials, as both particles have a positive elementary charge. In perfect crystals, positrons delocalise in interstitial sites and annihilate with electrons there, since positrons are strongly repelled by ion cores due to Coulomb repulsion, as are protons. Similar to protons, positrons are trapped by vacancy clusters or dislocations, which have lower densities of ion cores than the bulk material. They annihilate with electrons in the defects. Positron-annihilation characteristics observed in defects are unique for each type of defect, and make it possible to identify existing defects with which protons could have strong interactions. Thus the positron is a unique probe that gives us direct information from the standpoint of the proton about hydrogen storage materials and their structural changes during hydrogen absorption and desorption process [16].

PAS is also more sensitive to small defects, and lower densities of defects, than any other characterization method. Figure 5 shows that on hydrogenation of the $LaNi_{5-x}Al_x$ system the value of Tau 1 as well as its intensity increases, indicating the reduction in electron density due to hydrogenation of material. This suggests that hydrogen takes electron from the host intermetallic compound and obeys the anionic model, thus well agreeing with earlier results in the case of FeTi and $Fe_{46}Ti_{50}Mn_4$ and their hydride system [17].

The outcome of this study confirms that in all three different samples the activation process has generated microstructural changes [15]. Detailed analysis of positron annihilation spectra has indicated generation of small vacancy type of defects as well as bigger conglomerates of the defects. This indication is confirmed by the increase of lifetime Tau 1. The intensity of this parameter is raised as well (Fig. 5).

The positron lifetime spectra can be decomposed vacancy clusters (~225 ps), dislocations (~175 ps) and the matrix (~130ps) [16]. High lifetimes up to 600ps were obtained from fitting the spectra with the second parameter Tau 2 (Fig. 6). The analysis of the experimental results indicated that the increase in value of Tau 2 can be attributed to the trap of molecular hydrogen, which is likely to be in the defect sites in bulk materials.

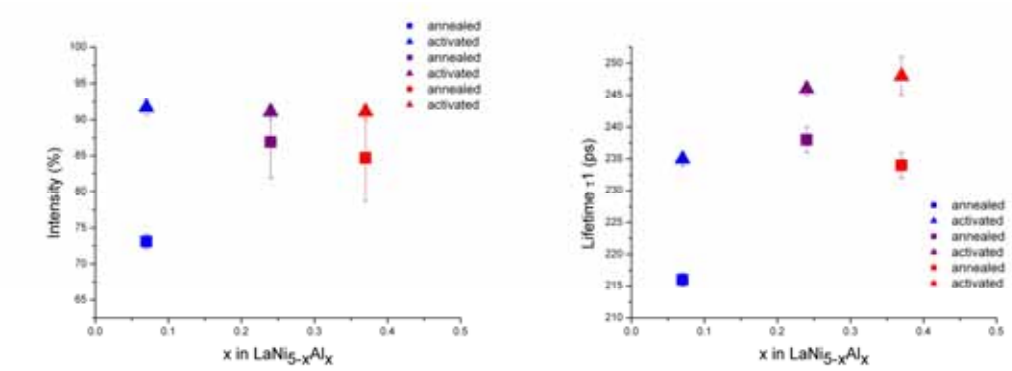

FIG. 5. Positron lifetime in ps and relative intensities in % were obtained from the measurements. An increase of lifetime and intensity of Tau 1 indicate the generation of small vacancy type of defects as well as bigger conglomerates during hydrogen absorption.

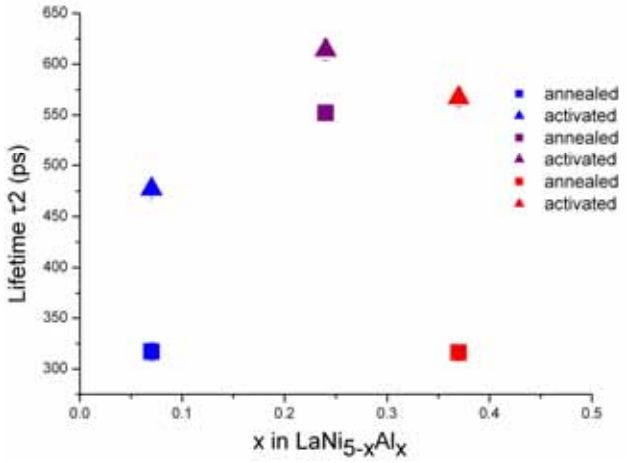

FIG. 6. PAS lifetime tau2.

4. CONCLUSIONS

The results clearly show that substitution of Al into $LaNi_5$ influences not only hydrogenation properties but also the introduction and/or accumulation of lattice strain by the hydrogenation and dehydrogenation.

The results of the peak broadening analysis reveal that the dislocation density is very low for materials with the highest Al content. The PAS results seem to be in contradiction to the XRD analysis, as no strong correlation between defect density and Al content was found. However, the type of defect detected by each method is different. For the PAS data, the increase in Tau1 lifetime is assigned to the bulk structure as well as vacancy type of defects, which are not detectable by the XRD methods employed in this study. The two methods are therefore complementary. Comprehensive information about the microstructural processes can be achieved only by combination with other techniques, such high-resolution transmission electron microscopy and/or small angle neutron scattering.

REFERENCES

[1] BULL, D.J., BUSBY, P., KELLY, P., ROSS, D.K., Nucl. Instr. Meth. (in press).
[2] LARSON, A.C., VON DREELE, R.B., Los Alamos National Laboratory Report LAUR 86-748.

[3] Large Array Manipulation Program
http://wwwold.ill.fr/data_treat/lamp/lamp.html
[4] RODRIGUEZ-CARVAJAL, J., Abstracts of the Satellite Meeting on Powder Diffraction of the XV Congress of the IUCr (1990) 127.
[5] WEIDNER, E., BULL, D.J., SHABALIN, I.L., KEEN, S.G., TELLING, M.T.F, ROSS, D.K., Chem. Phys. Lett. **444** (2007) 76-79
[6] BULL, D.J., et al., Phys. Chem. Ch. Ph.
[7] WEIDNER, E., et al., J. Phys. Chem. C **113** (2009) 15772-15777
[8] CHEN, P., XIONG, Z.T., LUO, J.Z, LIN, J. Y., TAN, K.L., Nature **420** (2002) 302.
[9] FULTZ, B., WITHAM, C.K., UDOVIC, T.J., J. Alloys Comp. **335** (2002) 165.
[10] INUI, H., YAMAMOTO, T., HIROTA, M., YAMAGUCHI, M., J. Alloys Comp. **330/332** (2002) 117.
[11] WU, E., GRAY, E.MACA., COOKSON, D.J., J. Alloys comp. **330/332** (2002) 229.
[12] KIM, G.-H., LEE, S.-G., LEE, K.-Y., CHUN, C.-H., LEE, J.-Y., Acta Metall. Mater. **43** 6 (1995) 2233.
[13] KRIVOGLAZ, M.A., Theory of X ray and Thermal Neutron Scattering by Real Crystals,Plenum Press, New York, 1969.
[14] CERNY, R., JOUBERT, J.-M., LATROCHE, M., PERCHERON-GUEGAN, A., YVON, K., J. Appl. Cryst. **33** (2000) 997.
[15] MORETTO, P., WEIDNER, E., ZEMAN, A., PFRANG, A. (in preparation).
[16] SHIRAI, Y., ARAKI, H., MORI, T., NAKAMURA, W., SAKAKI, K., J. Alloys Comp. **330–332** (2002) 125–131.
[17] SINGH, M., JAIN, J.P., Int. J. Hydrogen Energy **21** (1996), 367.

APPLICATIONS FOR IN-SITU NEUTRON DIFFRACTION ON HYDROGEN STORAGE MATERIALS

F. DOLCI[1], E. WEIDNER[1], M. HOELZEL[2], T. HANSEN[3], M. FICHTNER[4], W. LOHSTROH[4]
[1]JRC Institute for Energy of the European Commission, Petten, Netherlands
[2]Forschungs-Neutronenquelle Heinz Maier-Leibnitz, Garching, Germany
[3]Institute Laue Langevin, Grenoble, France
[4]Karlsruhe Institute of Technology, Karlsruhe, Germany
francesco.dolci@ec.europa.eu

Abstract: In situ diffraction techniques above all, offer the unique opportunity of probing in real time and under experimental conditions the behaviour of the investigated compounds. Especially in-situ neutron diffraction seems to be a preferential choice for the study of hydrogen storage materials, since hydrogen is clearly identified and the structural characterization of the compound can be complete and effective. Phase evolution during hydrogen absorption and desorption cycles and detection of new intermediate phases can be successfully pursued with a considerable improvement in the basic understanding of the material. The use of amide/alkaline hydride mixtures illustrates well such a typical case. In order to obtain a more accurate reaction path for the absorption/desorption processes of magnesium amide ($Mg(NH_2)_2$) and lithium hydride (LiH) mixtures, in-situ neutron diffraction techniques have been employed. Experiments were performed at D20/ILL and SPODI/FRMII. The results reveal a common reaction pathway for 1:2, 3:8 and 1:4 magnesium amide:lithium hydride mixtures. Intermediate reaction steps are always observed in both ab- and desorption. The thermodynamic properties of the system at 200°C are not changed by changing lithium hydride stoichiometry.

1. INTRODUCTION

One of the most attractive suggestions for an efficient and clean energy carrier is hydrogen. Solid state hydrogen storage materials, in particular, are a possible alternative to gaseous or liquid hydrogen, since they combine a high volumetric storage capacity coupled with a relative safety. Especially in recent years, the family of complex hydrides has elated much interest and triggered off a considerable amount of experimental and theoretical research [1]. Moreover, the idea of mixing different complex hydrides together, or with light metal hydrides, has shown very promising results and opened new possibilities for the design of practical hydrogen storage materials. The results obtained are however far from the ones expected on the basis of a simple thermodynamic modelling of the system. Research carried on in the last years, in particular, has pointed out as naive the idea of a simple and direct desorption/absorption reaction between the starting materials, moving to the desorbed products and back [2-6].The use of amide/alkaline hydride mixtures illustrates such a typical case. These compounds are reversible and in particular for the mixed Li-Mg-N-H system the thermodynamic properties associated with hydrogen absorption and desorption should allow an equilibrium pressure of 1 bar hydrogen at 90°C [7]. The proposed reversible decomposition pathway is the following:

$$Mg(NH_2)_2 + 2LiH \leftrightarrow Li_2Mg(NH)_2 + 2H_2 \quad (1)$$

However, by probing with in-situ neutron diffraction measurements the PCI (Pressure Composition Isotherm) of the Li-Mg-N-H system it is clearly possible to notice an intermediate passage with the formation of a new phase [8,9]:

$$2Mg(NH_2)_2 + 4LiH <-> Li_2Mg_2(NH)_3 + LiNH_2 + LiH + 3H_2 \leftrightarrow 2Li_2Mg(NH)_2 + H_2 \quad (2)$$

The concept of the formation of intermediate phases during the hydrogen absorption and desorption processes is important for the fundamental understanding of the mechanism leading to hydrogen uptake and release. In situ diffraction techniques above all, offer the unique opportunity of probing in real time and under experimental conditions the behaviour of the investigated compounds. Especially in-situ neutron diffraction seems to be a

preferential choice for the study of hydrogen storage materials, since hydrogen (deuterium) is clearly identified and the structural characterization of the compound can be complete and effective. Phase evolution during hydrogen absorption and desorption cycles and detection of new intermediate phases can be successfully traced with a considerable improvement in the basic understanding of the material.

2. EXPERIMENTAL

The portable Sievert's apparatus used is formed by several calibrated volumes, two pressure measuring devices for different ranges, connecting tubing, valves and sample holder. These parts are mainly ASI-316L type stainless steel, which can withstand high hydrogen pressures (see Fig. 1). During the experiments the sample holders used were produced either from a specific type of Inconel (754), which does not activate in a neutron beam, or stainless steel (ASI-316L).

FIG. 1. The portable Sievert's apparatus used.

Some neutron diffraction measurements were performed on the D20 instrument at the Institute Laue Langevin reactor source, Grenoble, France. This instrument provides high flux and a curved linear position sensitive detector (PSD) resulting in rapid data acquisition over the full angular coverage. With the selected wavelength of 2.42 Å, a d-spacing range of about 10 Å to 1.4Å was obtained. Time resolved diffraction with a resolution of one minute was possible. Data sets were corrected for detector efficiency against a vanadium standard, using the standard ILL data processing software LAMP [10]. Profile refinement was performed using the Rietveld method with the software package MAUD [11].

Other experiments took place at the SPODI instrument at Forschungsreaktor Muenchen (FRM II). The instrument provides diffraction patterns with excellent profile shape and high resolution over a wide 2θ scattering angular range. Thus it is suited for structure refinement on complex systems, in particular phase mixtures. On the other hand, the stepwise movement of the detector array lowers the efficiency and limits the possibilities for time resolved studies.

3. RESULTS AND DISCUSSION

Three different mixtures were produced by ball-milling different stoichiometric amounts of magnesium amide/lithium hydride: 1:2 ($1Mg(NH_2)2$:2LiH), 3:8 ($3Mg(NH_2)2$:8LiH) and 1:4 ($1Mg(NH_2)2$:4LiH). Neutron diffraction measurements for the 1:2 and 1:4 mixture were performed at the D20 instrument at the Institute Laue Langevin reactor source, Grenoble, France. The 3:8 mixture was analysed at the SPODI instrument at the FRMII reactor source,

Munich, Germany. This instrument provides better angular resolution compared to D20 at the expenses of a slower data acquisition rate. With the selected wavelengths of 2.42 Å for D20 and 2.54 Å for SPODI, a d-spacing range of about 1.4 -10Å is probed. Deuterium gas was used in preference to hydrogen, owing to its favourable coherent-to-incoherent scattering ratio. The phase evolution in different patterns was followed by Rietveld analysis.

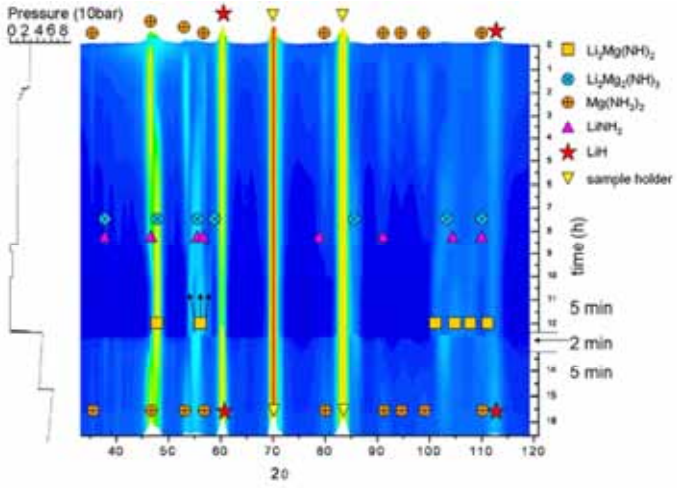

FIG. 2. Diffraction Pattern evolution at 200°C for the 1:4 mixture.

For each mixture an intermediate step with a molar ratio $LiNH_2$:$Li_2Mg_2(NH)_3$ of approximately 1:1 was found, in agreement with reaction 2. An example is shown in Fig. 2 where a complete desorption/absorption cycle is depicted for the 1:4 mixture. In conclusion it is possible to state that by means of in-situ neutron diffraction measurements that the hydrogenation/ dehydrogenation reaction pathway at around 200°C of the three different magnesium amide/lithium hydride mixtures does not change by increasing the lithium hydride content in the system. The comparison of data collected at the SPODI/FRMII and D20/ILL beamlines offer complementary information on crystallographic identity and phase evolution kinetics. The experimental observations for the 1:2, 3:8 and 1:4 mixtures are common and can be summarised as follows:

- Starting from the desorbed state the material is composed of alpha-$Li_2Mg(NH)_2$ (and LiH for the 3:8 and 1:4 mixtures).

- At 200°C and hydrogen pressures between 7 and 40 bar the formation of $LiNH_2$ and $Li2Mg_2(NH)_3$ is observed and the amount of LiH increases.

- At 200°C $Mg(NH_2)_2$ appears only after raising the hydrogen pressure above 40 bar.

ACKNOWLEDGEMENTS

F. Harskamp is acknowledged for the work done on the design and realisation of the portable Sievert's apparatus.

REFERENCES

[1] ORIMO, S., et.al., Chem. Rev. **107** (2007) 4111.
[2] WEIDNER, E., et al., Chem. Phys. Lett. **444** (2007) 76.
[3] RIJSSENBEEK, J., et. al., J. Alloys Compd. **454** (2007) 233.
[4] WU, H., J. Am. Chem. Soc. **130** (2008) 6515.

[5] GARRONI, S., et. al., Scripta Mat. **12** (2009) 1129.
[6] HU, J., et. al., J. Phys. Chem. C **111** (2007) 18439.
[7] LUO, W., J. Alloys Compd. **381** (2004) 284.
[8] WEIDNER, E., et al. J. Phys. Chem. C **113** (2009) 15772.
[9] DOLCI, F., et al. Int. J. Hydrogen Energy **35** (2010) 5448.
[10] Large Array Manipulation Progra http://wwwold.ill.fr/data_treat/lamp/lamp.html.
[11] MAUD: Material Analysis Using Diffraction http://www.ing.unitn.it/~maud/.

STUDY ON HYDROGEN ABSORPTION PROPERTIES AND CRYSTAL STRUCTURE OF LANIAL AND ZRVFE ALLOYS BY MEANS OF XRD

Y. YIMING, Y. YUANFANG, H. LI, Z. PINGZHU, H. SHILIN
China Institute of Atomic Energy
China
yym@ciae.ac.cn

Abstract: Hydrogen adsorption and desorption properties of LaNi alloys can be ameliorated by the addition of aluminium. The thermodynamic and kinetics performance of LaNi4.25Al0.75 alloy for the application of hydrogen storage was studied. LaNi4.25Al0.75 alloy and its deuteride were studied by means of X ray diffraction. Some information about the corresponding crystal structure were obtained. The hydrogen absorption and desorption properties of ZrVFe alloys were studied. The relationship between the phase component and properties was discussed by means of X ray diffraction.

1. INTRODUCTION

Nowadays hydrogen is becoming more and more important in industry fields and our daily life. Hydrogen has been widely used, but the application way and effiency still need to be improved. We are facing the challenges of hydrogen energy which foucsed on hydrogen storage and conversion. Some alloys are suitable for hydrogen storage and transportation. $LaNi_5$ alloy is a good choice, but its equilibrium hydrogen pressure was a bit high and it was based on heavy-weight elements.

Some of the work was proposed to ameliorate hydrogen storage properties by adjusting the composition of LaNi alloy. The equilibrium hydrogen pressure of LaNiAl alloy was a bit high and it may drop down by adjusting the content of aluminium; the hydrogen storage capacity is expected to increase.

2. ALUMINIUM ADDITION TO LANI ALLOY

$LaNi_{5-x}Al_x$ alloys were synthesized by melting lanthanum (high purity of 99.5%), nickle(high purity of 99.9%) and aluminium (high purity of 99.7%) in vacuum furnace. The prepared specimen was put into a vacuumed quartz tube and then annealed.

$LaNi_{5-x}Al_x$ alloys were tested on an established testing system.The PCT curve was obtained (Fig. 1) and the test temperature was 333K. With the increase of aluminium content, the plateau pressure dropped down and the plateau regions narrowed. It means the decrease of hydrogen absorption capacity. It may be interpreted as that aluminium increased the volume and spacing of crystal lattice, then it was easier for hydrogen atom to enter.

As shown in Fig. 2, linearity was exhibited between the logarithm of plateau pressure and aluminium content. Combining with the results of XRD test, the relationship between crystal lattice volume and plateau pressure was shown (Fig. 3). It can be seen that there seemed an approximate linearity between the logarithm of plateau pressure and crystal lattice volume, which means that plateau pressure at certain temperature may be forecasted according to the aluminium content.

The $LaNi_{4.25}Al_{0.75}$ alloy was chosen for farther study according to corresponding practical application. The PCT curves of alloy before and after anneal were shown in Figure1-4. An obvious slope occurred in the plateau regions related to sample without anneal, which indicated the composition asymmetry of alloy sample. This asymmetry may caused by metallographic segregation during the process of alloy synthesis. After anneal, the crystal

structure of different parts of the alloy became uniform again, consequently the plateau region of PCT curve went to a more straight line.

3. STUDY ON HYDROGEN STORAGE PERFORMANCE OF $LaNi_{4.25}Al_{0.75}$ ALLOY

After the procedures of establishing test equipment, volume determination and activation of $LaNi_{4.25}Al_{0.75}$ alloy, the PCT characters and hydrogen absorption dynamics were studied.

It was shown (Fig. 4) that with the increase of temperature, the hydrogen absorption and desorption equilibrium pressure rose, the slope of plateau ascend too. The plateau pressure differences in the hydrogen absorption and desorption process existed. The phenomenon was referred to lag effect. The reason may relate to crystal structure change. At room temperature, the value of H/M can easily reach 4.5 and the plateau pressure was about several Kpa. An obvious plateau region of PCT curve occurred as the H/M value varied from 0.5 to 3.5. The plateau region narrowed when the test was performed at a higher temperature.

To study the stability of alloy, the PCT curves of hydrogen absorption and desorption were measured repeatedly (Fig. 5). At 80℃, hydrogen absorption equilibrium pressure of $LaNi_{4.25}Al_{0.75}$ alloy was about 28KPa and the desorption one was about 25KPa. Figure 5 shows the experimental data of the beginning of four hydrogen absorption-desorption cycles. The first hydrogen absorption curve differed from the latters obviously due to insufficient activation. After activation, the three hydrogen absorption and desorption curves were very close, indicating the alloy was of a good stability.

If there were no special requirements, hydrogen absorption was usually carried out at a lower temperature. The hydrogen absorption speed at room temperature was demonstrated (Fig. 6), which showed some dynamic characters of the alloy.

Hydrogen desorption speed at different temperature was studied and the experimental data were shown (Fig. 7). If greater speed was needed, higher hydrogen desorption temperature was required.

In addition, some deuterium absorption experiments were also performed. Deuterium was found easier to integrate with the alloy with higher stability. Hydrogen and deuterium absorption dynamics were almost the same.

4. XRD RESULTS OF $LaNi_{4.25}Al_{0.75}$ ALLOY

In order to explore the phase change of $LaNi_{4.25}Al_{0.75}$ alloy after hydrogenation or deuteration, different kinds of $LaNi_{4.25}Al_{0.75}$ alloy samples were prepared and tested through XRD analysis. The exact location of diffraction peaks was determined by quantitative slow scanning. Germany bruker D8 advance was adapted as the X ray diffraction machine, Cu (Kα) radiation, tube voltage 40kV, tube current 40mA.

The XRD patterns of alloy and hydride alloy were shown in Fig. 9 and Fig. 10. The diffraction peaks of the hydrid were in accord with those of the alloy, and the difference was the peaks shifted toward small-angle direction. The results indicated that it was not the crystal structure but the crystal lattice spacing changed after the hydrogenation, and the change of crystal lattice spacing leaded to volume expansion and alloy pulverization.

X ray diffraction results indicated that the $LaNi_{4.25}Al_{0.75}$ alloy has the same crystal structure with the $LaNi_5$ alloy. They both belonged to $CaCu_5$ hexagonal crystal system. The lattice parameters of the alloy can be calculated through X ray diffraction results as shown in Table 1. The lattice constant of alloy increased with the addition of aluminium [1]. The quantity increased of c was a bit larger than that of a, which made the value of a/c decrease slightly. Aluminium increased the cell volume, which may be interpreted as the difference of atomic radius. A bigger atom Al (1.43 Å) took the place of a smaller atom Ni(1.25 Å), and then the crystal lattice was enlarged. After hydrogenation, the hydrogen atoms in the hydride formed interstitial solid solutions in the lattice, generally within a gap in the tetrahedron. The larger for the crystal lattice gap, the easier for the hydrogen atom to get into the gap. At the same temperature, the lower hydrogen pressure was required to drive the hydrogen atom into the crystal lattice, the more stable for the formed hydride.As the thermodynamic performance of PCT curve concerned, hydrogen absorption and desorption equilibrium pressure dropped.

5. STUDY ON HYDROGEN STORAGE PERFORMANCE OF ZRVFE ALLOY

The equilibrium hydrogen pressure of LaNiAl alloy may still not be low enough after amelioration. In the case of hydrogen removal, it was necessary to adopt an alloy with super-low equilibrium hydrogen pressure. We also carried out this part of research work.

The hydrogen absorption PCT curve of the ZrVFe alloy sample from 673K to 873K were shown in Fig. 11. An obvious hydrogen absorption plateau was found. The plateau pressure became higher with the increase of temperature. The curve slope increased with the increase of absorbed hydrogen quantity, indicating the formation of more β-phase hydride. Groups of hydrogen absorption capacity (H/M) were selected and equilibrium pressure were obtained under different experimental temperature. A new graph was ploted to logP of the 1000/T (Fig. 12). The thermodynamic parameters $\Delta H\theta$, $\Delta S\theta$ of hydrogen absorption were calculated according to the slope and intercept of the fitting line. Then hydrogen absorption equilibrium pressure at room temperature was obtained through VanHoff equation. The PCT curve of hydrogen desorption was ploted by the same way (Fig. 13). The fitted thermodynamic curve was shown in Fig. 14.

To study the stability of hydrogen absorption properties, the PCT curve of hydrogen absorption and desorption was measured repeatedly at 500℃ (Fig. 15). At 500 ℃, hydrogen absorption equilibrium pressure of ZrVFe alloy was about 7Pa. The figure showed the experimental data of the beginning four hydrogen absorption and desorption cycles. They were very close, indicating good stability of hydrogen absorption properties of the alloy.

As shown in Fig. 16, the desorption equilibrium pressure was lower than the aborption one,which demonstrated significant lag effect. Different ideas were shown on this point. Plastic degradation mechanism is a more widely accepted theory. The defects of different density made the hydrogen absorption and desorption plateau pressure deviate from the true equilibrium pressure.

As far as the dynamics concerned, the hydrogen absorption speed was measured repeatedly (Fig. 17). The hydrogen absorption curves were very close except the first cycle, indicating the alloy was of a good stability.The difference mentioned above was mainly caused by different specific surface of the alloy.

Hydrogenation velocity curves of different initial H/M ratio were shown in Fig. 18. It was found that hydrogen absorption velocity dropped with the increase of H/M. This may be

interpreted as that with the H/M ratio increased, hydrogen equilibrium pressure increased and hydrogenation driving force caused by pressure difference decreased.

The dehydrogenation velocity curve with the same H/M at different temperatures were shown in Fig. 19. It can be found that the decomposition rate of hydride increased with temperature.

In addition, the properties of the resistance to air poisoning were studied. The alloy showed good resistance to pulverization and combustion performance [2].

6. XRD RESULTS OF ZRVFE ALLOY

In order to explore the phase change of ZrVFe alloys after hydrogenation or deuteration, different kinds of ZrVFe alloy samples were prepared and tested through XRD analysis. Germany bruker D8 advance was adapted as the X ray diffraction machine, Cu (Kα) radiation, tube voltage 40kV, tube current 40mA.

ZrVFe alloy was cut into wafer and directly analyzed after sample polishing. Hydrogenated and dehydrogenated alloy samples were grinded before analysis.

XRD patterns of ZrVFe alloy and hydride samples were shown in Fig. 20 to Fig. 24. It can be seen that the raw materials were mainly composited from the metal Zr and Fe2Gd phase by comparing with the standard cards, indicating a certain amount of rare earth elements may also be used to adjust the properties of the alloy by replacing some of the V in ZrVFe alloy.

Figure 21 referred to the sample after dehydrogenation. It was shown that the metal phase was basicly recovered except a small amount of hydride phase caused by incomplete dehydrogenation. Figure 22 referred to the unsaturated hydrogenation sample. More diffration peaks of hydride were found and the metal phase decreased, indicating a typical mixture of α phase and β phase.

Figure 23 and 24 referred to alloy samples after saturated hydrogenation or deuteration. It was almost entirely made up of the hydride or deuteride of Zr and Fe_2Gd.

No obvious oxide phase was found on XRD patterns, indicating slight oxidation of the samples and good performance of oxidation resistance.

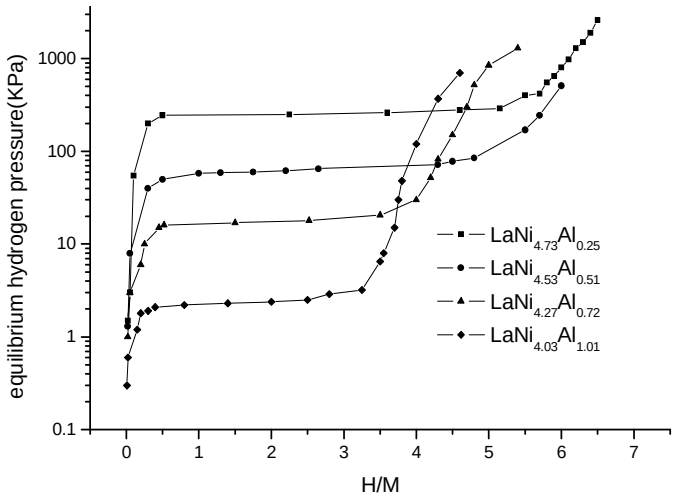

FIG. 1. PCT curve of LaNi5-xAlx alloy at 333K.

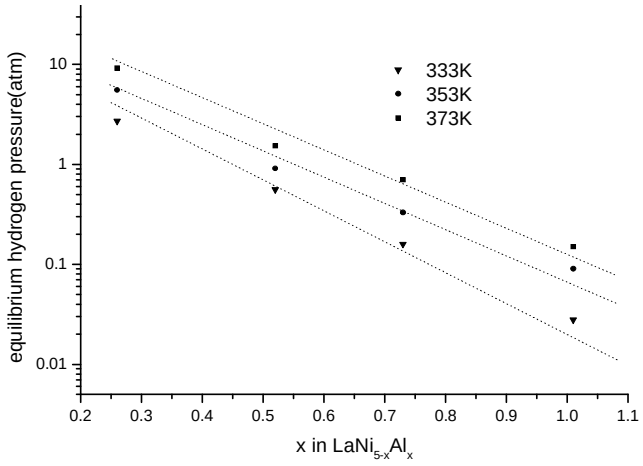

FIG. 2 .Relationship between aluminium content and hydrogen absorption plateau pressure.

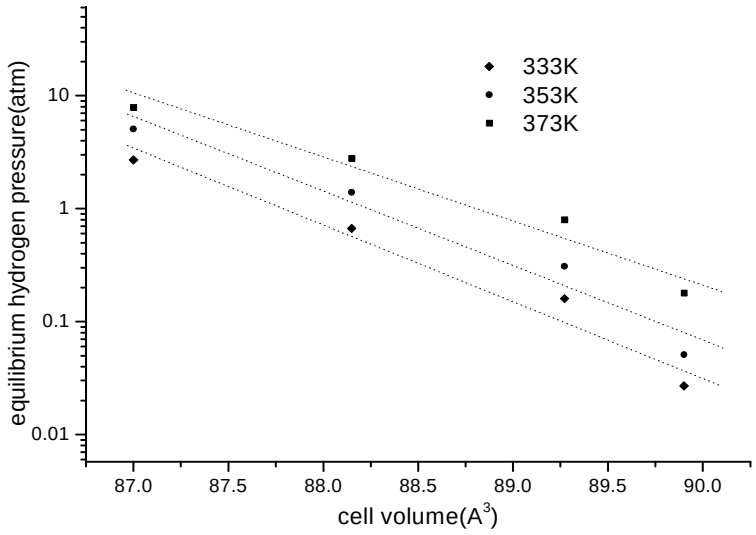

FIG. 3. Relationship between cell volume and hydrogen absorption plateau pressure.

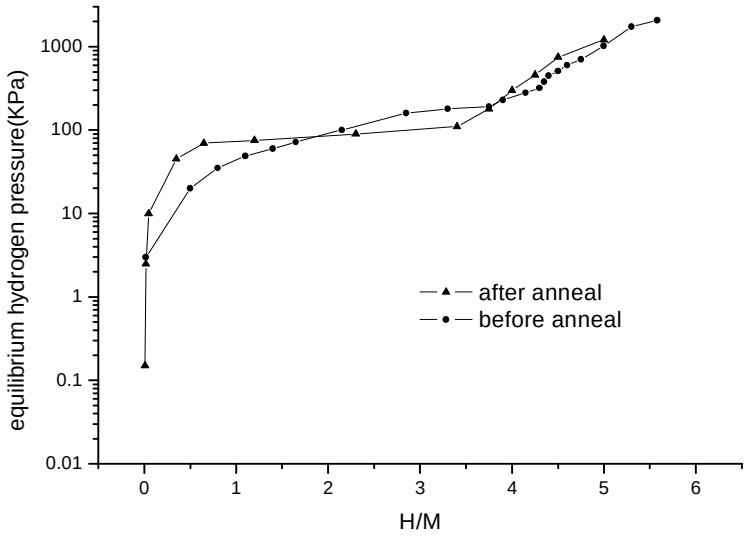

FIG. 4. P-C-T curves of LaNi4.25Al0.75 alloy and alloy annealed.

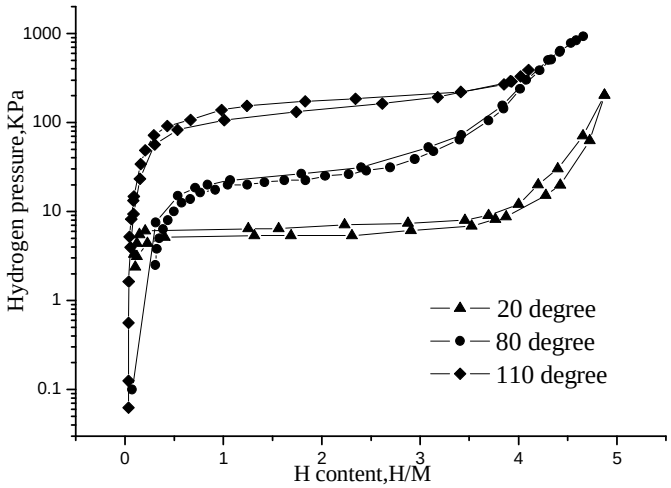

FIG. 5. P-C-T curve of LaNi4.25Al0.75 alloy at different temperature.

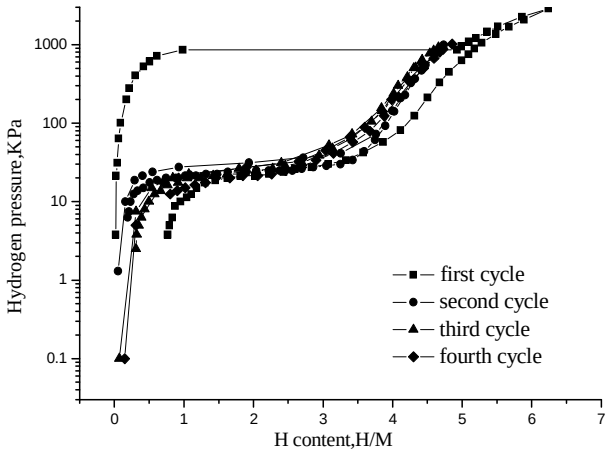

FIG. 6. P-C-T curve of LaNi4.25Al0.75 alloy at the temperature 80 ℃,weight of the alloy 3.183g.

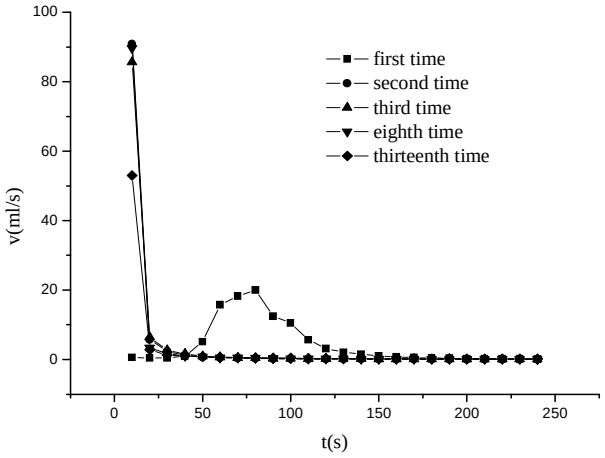

FIG. 7. The hydrogen absorption speed at room temperature, weight of the alloy 101.53g.

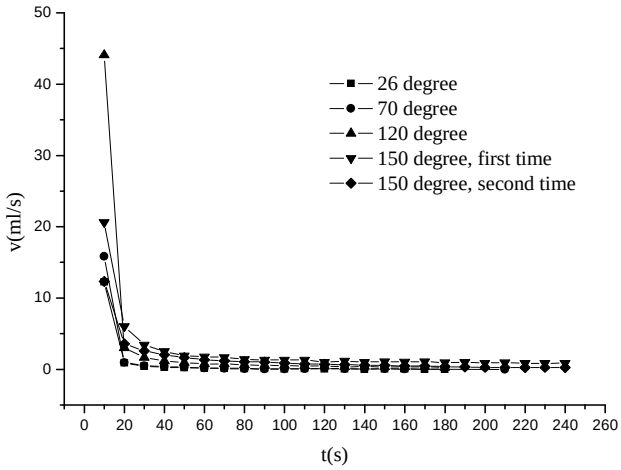

FIG. 8. Dehydrogenation velocity curve at different temperatures.

TABLE 1. THE LATTICE PARAMETERS OF THE ALLOY

1. alloys	2. A(Å)	3. C(Å)	4. a/c	5. V(Å^3)
6. $LaNi_5$	7. 5.019	8. 3.977	9. 1.262	10. 86.79
11. $LaNi_{4.27}Al_{0.72}$	12. 5.045	13. 4.05	14. 1.246	15. 89.26

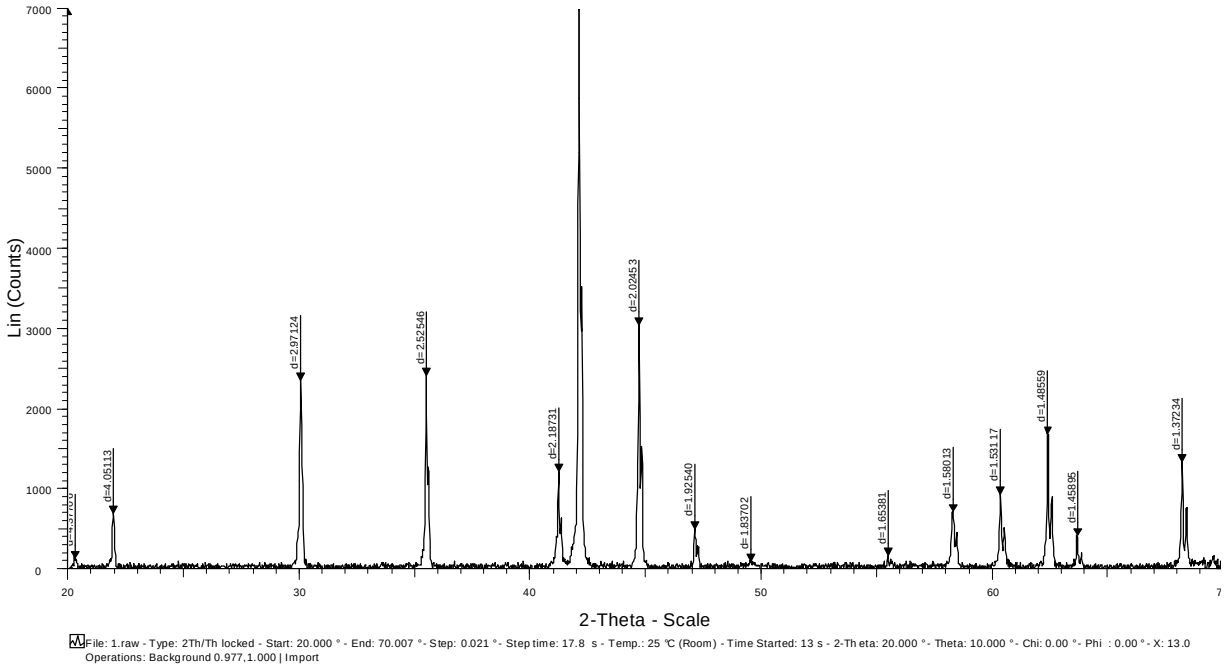

FIG. 9. XRD pattern of original LaNi4.25Al0.75 alloy.

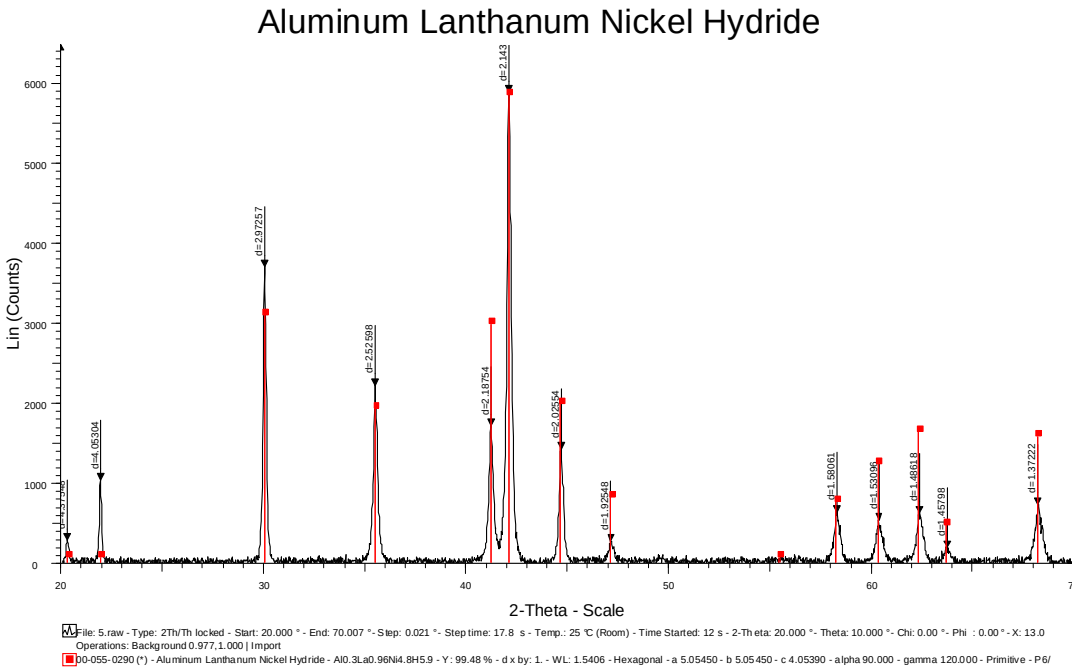

FIG. 10. XRD pattern of completely hydrogenated LaNi4.25Al0.75 alloy.

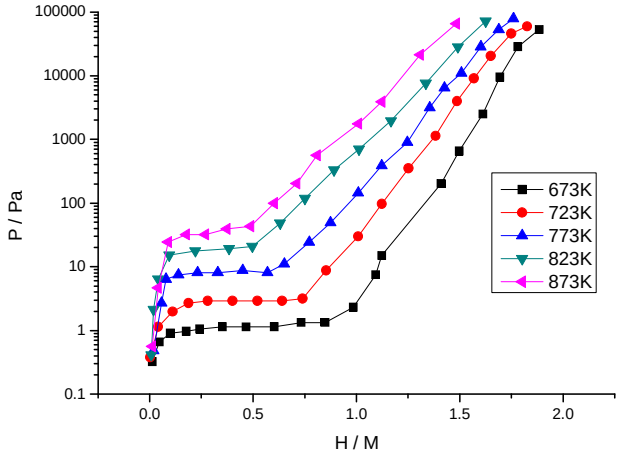

FIG. 11. Hydrogen absorption PCT curve of ZrVFe alloy

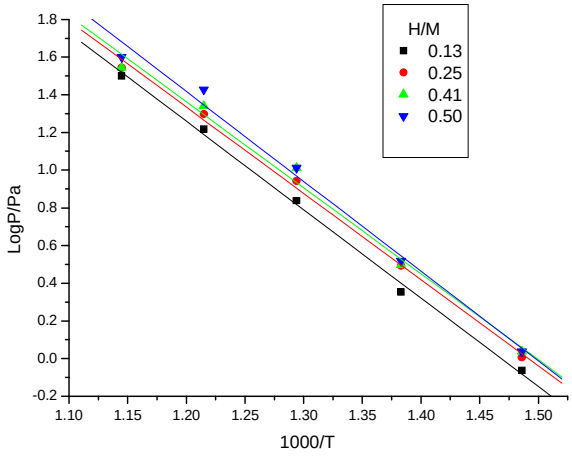

FIG. 12. VanHoff curve of ZrVFe hydrogenation.

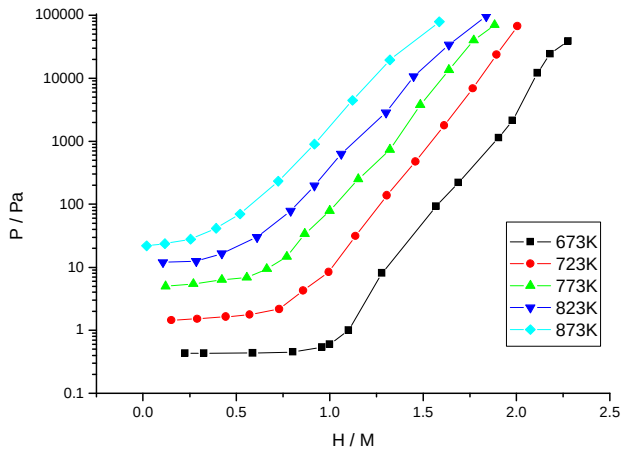

FIG. 13. Hydrogen desorption PCT curve of ZrVFe alloy.

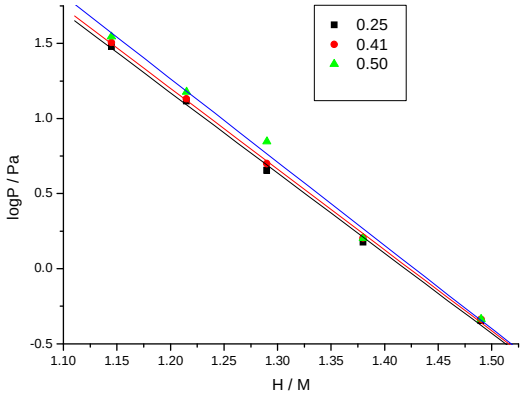

FIG. 14. VanHoff curve of ZrVFe dehydrogenation.

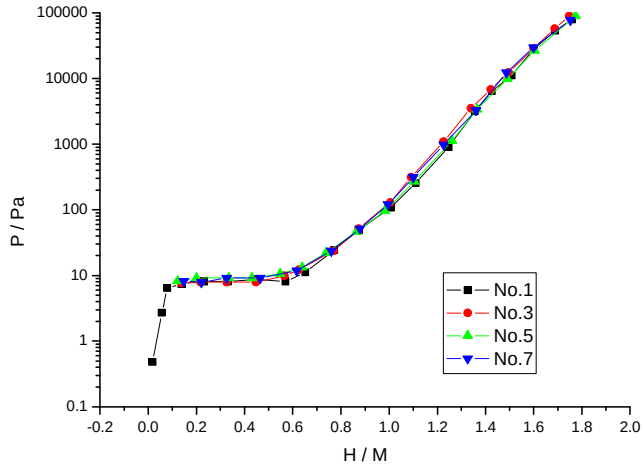

FIG. 15. Hydrogen absorption PCT curve of ZrVFe at 777K.

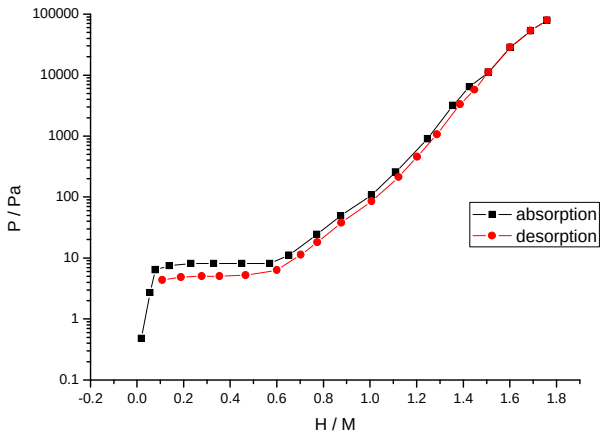

FIG. 16. Hydrogen absorption desorption PCT curve of ZrVFe at 773K.

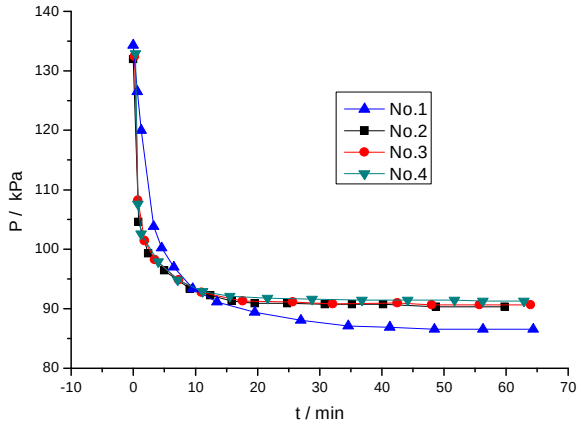

FIG. 17. Hydrogenation velocity curve H/M on hydrogenation velocity.

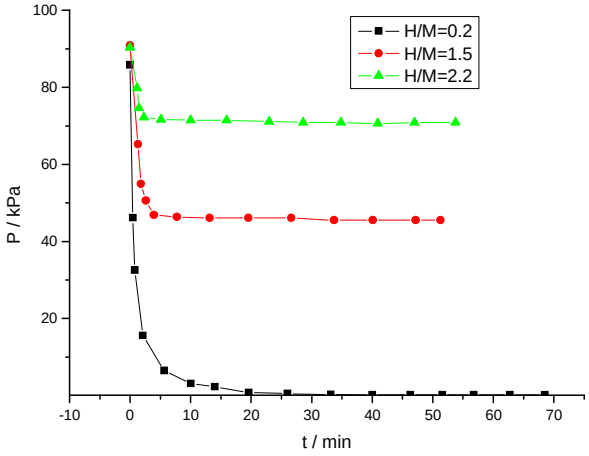

FIG. 18. Effect of different original at room temperature.

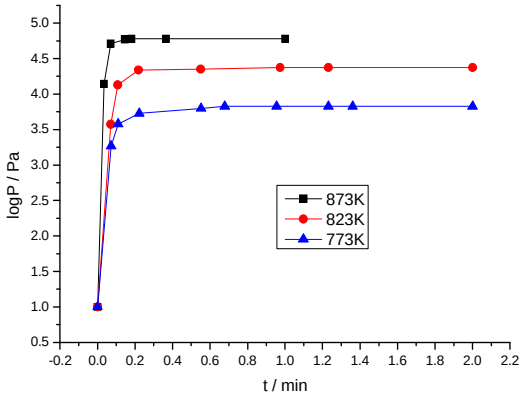

FIG. 19. Dehydrogenation velocity of H/M=1.45 hydride at different temperature.

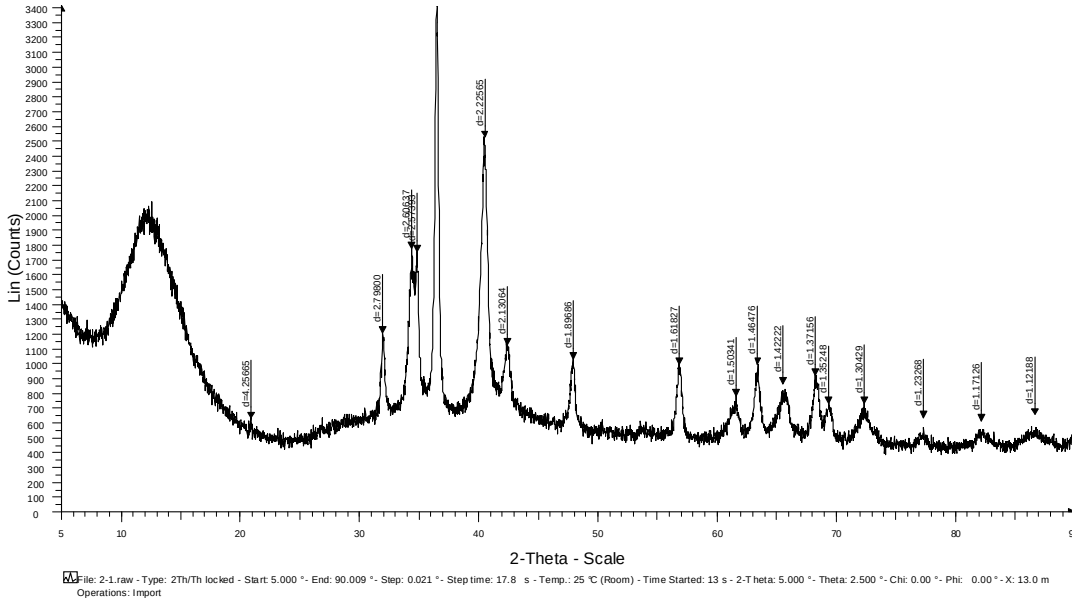

FIG. 20. XRD pattern of original ZrVFe alloy.

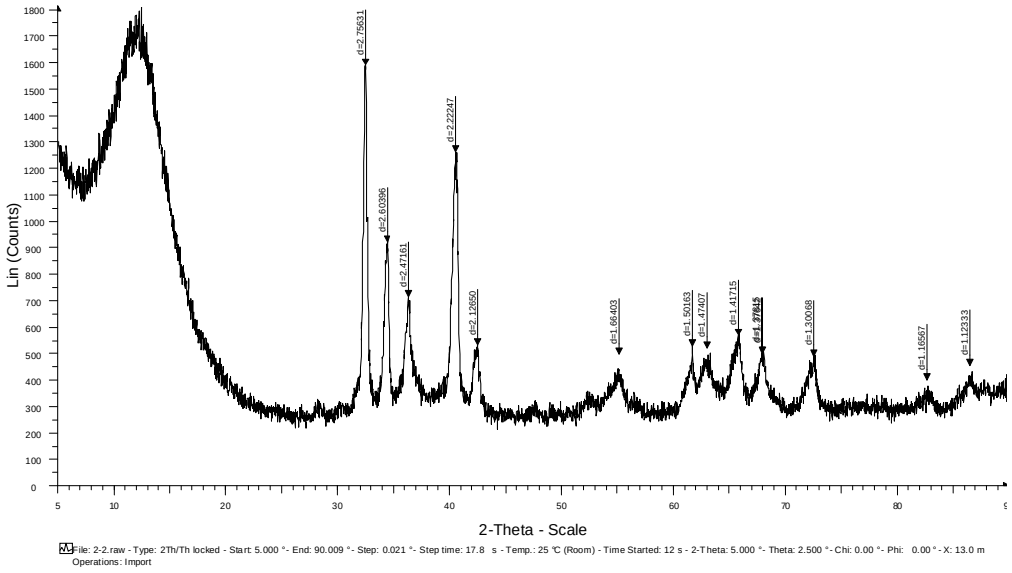

FIG. 21. XRD pattern of dehydrogenated ZrVFe alloy with some hydrogen remaining.

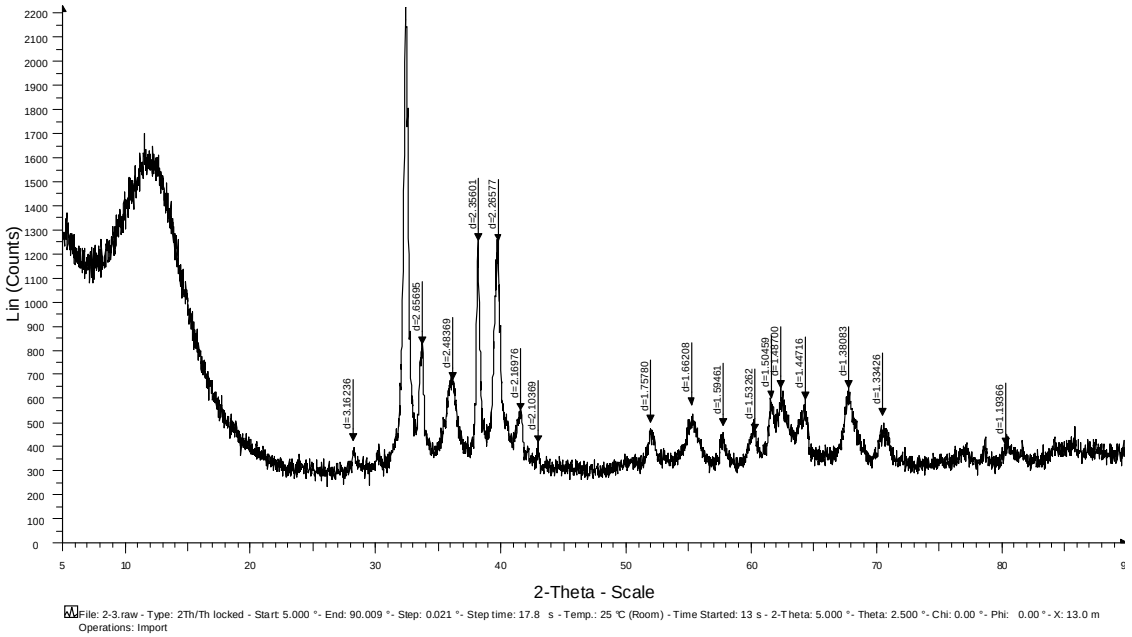

FIG. 22. XRD pattern of incompletely hydrogenated ZrVFe alloy.

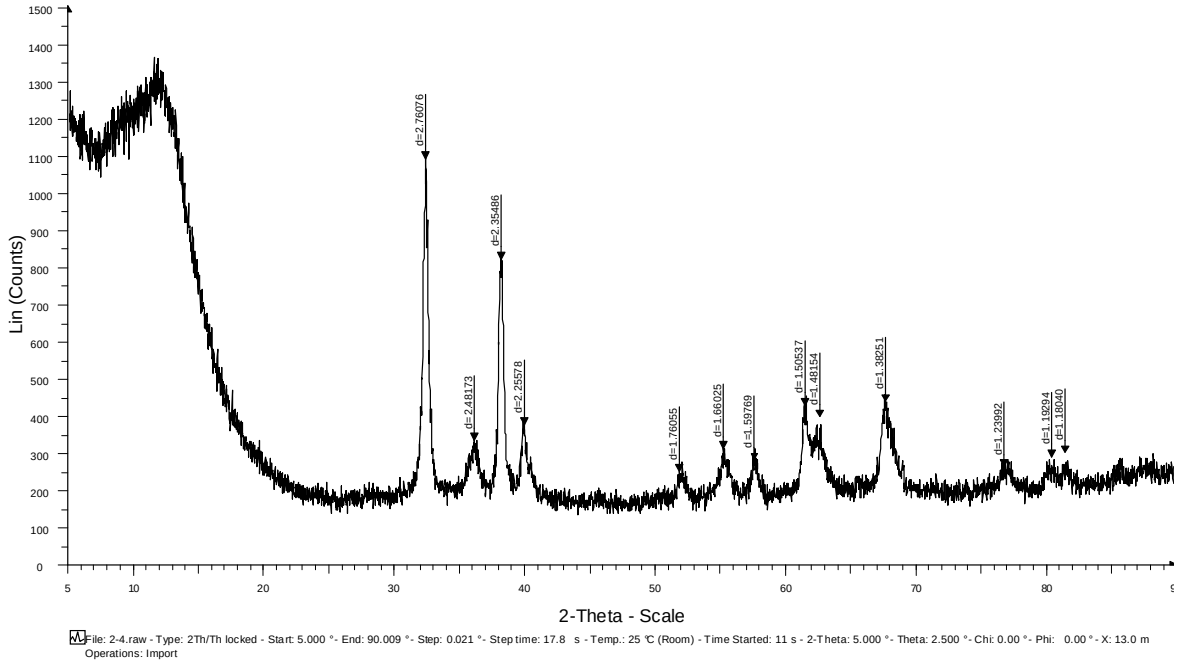

FIG. 23. XRD pattern of completely hydrogenated ZrVFe alloy.

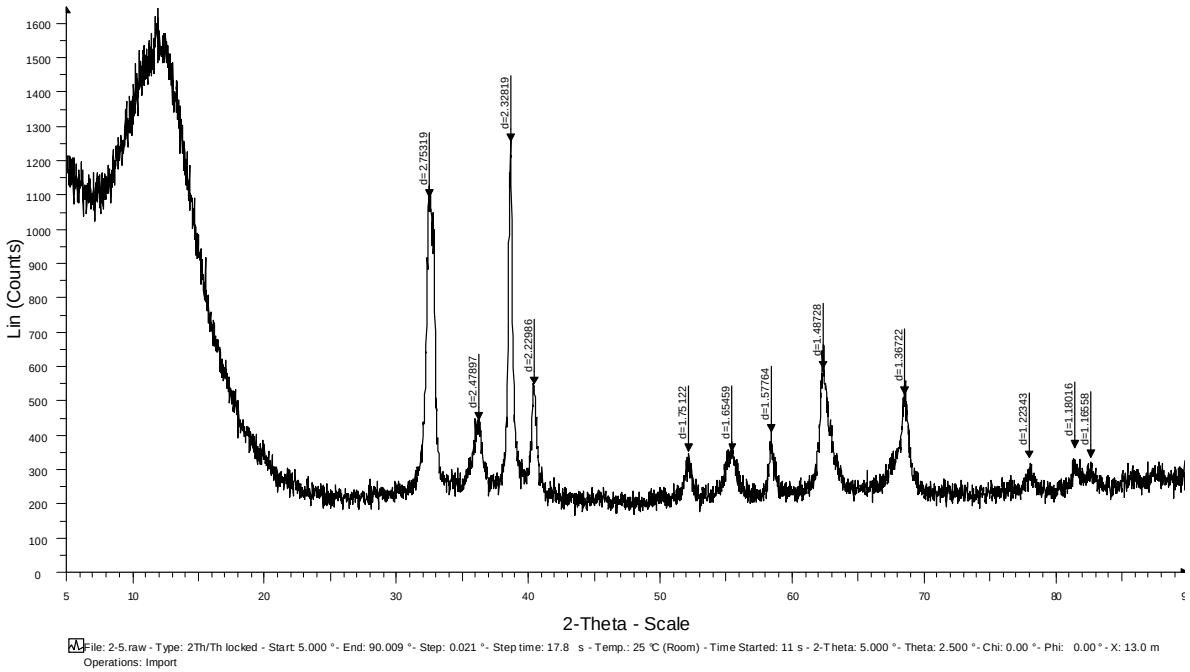

FIG. 24. XRD pattern of incompletely deuterated ZrVFe alloy.

REFERENCES

[1] PERCHERON-GUEGAN, A., LARTIGUE, C., ACHARD, J.C., GERMI, P., TASSET, F., J. Less Common Met. 74 (1980) 1-12.

[2] TRIPATHI, A., SINGH, N., AVASTHI, D.K., Vacuum. **48** (1997)1023-1025.

HYDROGEN DEPTH PROFILING USING TOF-ERDA AND IEE-ERDA SPECTROSCOPY

Z. SIKETIĆ, I. BOGDANOVIĆ RADOVIĆ, M. JAKŠIĆ
Ruđer Bošković Institute, P. O. Box 180, Zagreb
Croatia
zsiketic@irb.hr

Abstract. Determination of atomic concentrations in the compounds is one of key problems in materials science. Time-of-Flight Elastic Recoil Detection Analysis is a powerful method for depth profiling of light and medium mass elements in near surface layers of material. However, due to poor detection efficiency those spectrometers are not commonly used for hydrogen analysis. We have performed some improvements in order to increase detection efficiency and to make spectrometer more suitable for hydrogen analysis. The spectrometer performance was tested on amorphous Si sample implanted with H- ions. Sensitivity for hydrogen in silicon matrix was found to be several tens of ppm with a surface depth resolution of ~15 nm. With intention to be used for the 3D analysis of hydrogen, a Ion-induced Electron Emission (IEE) ERDA system has been installed on the nuclear microprobe. By positioning IEE ERDA system at 45° instead of 30°, as well as by using heavier ions (O ions instead of He), even two orders of magnitude better sensitivity can be obtained without significant deterioration of depth resolution due to the increased recoil cross section. The ability to use a system for 3D imaging of H in samples is demonstrated. The obtained depth resolution for hydrogen close to the silicon sample surface was found to be about 20 nm and the minimum detection limit for H detection in Si sample was estimated to be 3×10^{15} at/cm^2.

1. INTRODUCTION

Time-of-Flight Elastic Recoil Detection Analysis (TOF-ERDA) was developed in mid-1980s by several research groups for applications in different research areas such as optoelectronics, thin-film sensors, interfacial diffusion or reactions semiconductor devices [1-3]. Energy and time of flight of the recoiled atoms are measured in coincidence which enables us to separate all elements by energy and mass. Time/energy spectra are converted to depth profiles using known relation of energy loss by unit of length of the ions in the sample (stopping power). The advantage of TOF-ERDA is that all elements with an atomic mass less than or equal to 28 can be simultaneously detected and depth profiled. Also, the energy straggling due to absorber foils is an order of magnitude smaller than in foil ERDA. The cross-sections for the recoiling of H with heavy ions (Cl, I, Au…) are high due to the mass factor in the Rutherford formula. Therefore, TOF-ERDA spectroscopy is very sensitive technique for light element detection and analysis.

The reason why TOF-ERDA is not usually used for H detection is that, unlike for silicon particle detectors, the efficiency of carbon-foil time detectors is less than 100% for light elements. The detection efficiency depends on the energy as well as on the electronic stopping power of analyzing recoil atoms in the C foil, and this fact can be particularly critical for hydrogen for which the detection efficiency can drop as low as 10 % [4, 5]. Therefore, TOF-ERDA spectrometers have not been the best choice for depth profiling and quantification of hydrogen.

To improve the relative detector efficiency for the lightest elements, it was important to increase the electron yield from diamond-like carbon (DLC) foils. Thin insulating films are known to be excellent electron emitters. Therefore we coated DLC foils with a thin LiF layer [6]. Using this procedure, Time-of-Flight (TOF) detector efficiency was enhanced up to 60% for 400 keV hydrogen [7] in comparison with other TOF systems where pure thin C foils were used and reported detection efficiency was around 20% [4, 8]. In case of TOF-ERDA it is important to have as thin foils as possible to reduce scattering and straggling effects in the foils.

To test depth profiling, an amorphous Si (a-Si) sample was implanted with 10 keV H- ions. The effectiveness of the method concerning depth resolution, sensitivity and stability for hydrogen are reported.

In the Ion-induced Electron Emission (IEE) Elastic Recoil Detection Analysis (ERDA) system scattered ions and recoil atoms pass through a set of four thin carbon foils before they reach a solid state (energy) detector. As the foils are thin with a total thickness of the four carbon foils of about 68 μg/cm^2 or 3400×10^{15} at/cm^2), energy resolution in the hydrogen recoil spectrum is not decreased. The number of electrons emitted from the foils is proportional to the stopping power of the particles in the foil material, which is a principle of particle identification in IEE ERDA [9, 10]. Emitted electrons are accelerated toward the microchannel plate (MCP) detector. The signal from the MCP detector, i.e. the number of emitted electrons, is measured in coincidence with the signal from the solid state detector (particle energy) and displayed in a two dimensional map. In comparison to ERDA with a stopping foil, this setup gives better depth resolution due to the reduction of energy loss straggling. It has been shown previously that IEE ERDA depth resolution with the broad beam near to the sample surface for detecting hydrogen in silicon matrix is about 45 nm [11] comparing to 80 nm obtained by foil ERDA [12] for the same energy-geometry setup (3 MeV α beam, 30° recoil angle) and a Si sample. For 6 MeV C ions and 30° recoil angle the depth resolution at the surface is about 20 nm [11]. Another advantage of IEE ERDA is that the spectra of recoiled atoms and forward scattered ions are detected in the same particle detector that makes quantitative analysis easier and removes a need for either parallel RBS measurement or current measurement.

To study the capabilities of IEE ERDA system for hydrogen measurements, Si sample implanted with 25 keV hydrogen ions was used. The obtained depth resolution for hydrogen close to the silicon sample surface was found to be about 20 nm and the minimum detection limit for H detection in Si sample was estimated to be 3 × 10^{15} at/cm^2.

2. EXPERIMENTAL DETAILS

2.1 Samples

For TOF-ERDA measurements a 300 nm thick layer in Si was amorphised (in order to avoid channeling effects) by Si implantation. To obtain a sample containing H, a-Si was implanted with 10 keV H- ions at nominal fluence of ~2×10^{16} at/cm^2.

To test the depth profiling abilities of IEE ERDA system, two samples were used: a) silicon sample implanted with 25 keV H- ions at nominal fluence of 5×1016 H- at/cm^2, b) silicon sample implanted with 25 keV H- ions through a 200 mesh cooper grid at nominal fluence of 2×10^{17} H- at/cm^2.

2.2 Experimental setup for TOF-ERDA

The TOF-ERDA spectrometer is installed at a beam line that can accept ions from a 6 MV EN Tandem accelerator. All measurements were performed with 20 MeV 127I6$^+$ ions. The incidence angle toward surface plane was θin=20°, and the scattering angle between the beam and the TOF-ERDA telescope was θscatt.=37.5°. During the measurements, the beam current density was kept between 0.03 pnA/mm^2 and 0.1 pnA/mm^2, and the ion beam fluence was ~ 1012 particles/mm^2.

The TOF-ERDA telescope consists of two timing detectors separated by 523 mm. The particle energy was detected using an ULTRA ion-implanted silicon detector with an area of

300 mm^2. The first timing detector was positioned 478 mm away from the target with a 6 mm collimator placed in front of it to reduce the amount of false start signals. Also, the collimator defined the solid angle of the telescope to be 0.11 msr. The time detectors were electrostatic mirror assemblies using the Busch design [13]. Our assembly included DLC foil (0.4 μg/cm^2 of C grid supported) coated with 2.5 μg/cm^2 LiF, three tungsten grid electrodes and a microchannel plate (MCP) for electron detection. Figure 1 shows measured values of the dependence of the relative detector efficiency on the electronic stopping power in the LiF. The detailed performance of the TOF-ERDA system as well as the efficiency enhancement for hydrogen is described in Ref. [7]. From Fig. 1, it can be seen that efficiency for ~ 400 keV hydrogen is ~ 60% (400 keV is the maximum recoil energy of H in the present measurements).

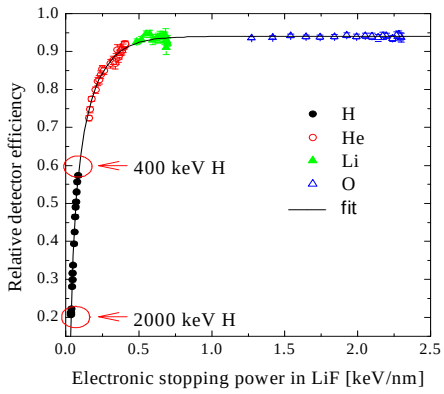

FIG. 1. Relative TOF-ERDA spectrometer efficiency versus electronic stopping power in LiF.

Measured spectra were normalized to efficiency curve (Fig. 1) while detected H energies were correlated with the depths from which the H atoms emerged. The resulting H depth profile (directly converted, slab analysis) was compared with profiles calculated by SRIM [14] as well as spectra simulated by the Monte Carlo (MC) simulation code CORTEO [15].

2.3 Experimental setup for IEE ERDA

All measurements were done using also the 6 MV Tandem Van de Graaff accelerator at the Ruđer Bošković Institute in Zagreb. Negative $^{16}O^{3+}$ ions were produced in a sputtering ion source. Figure 2 shows the layout of the IEE ERDA system in the scattering chamber.

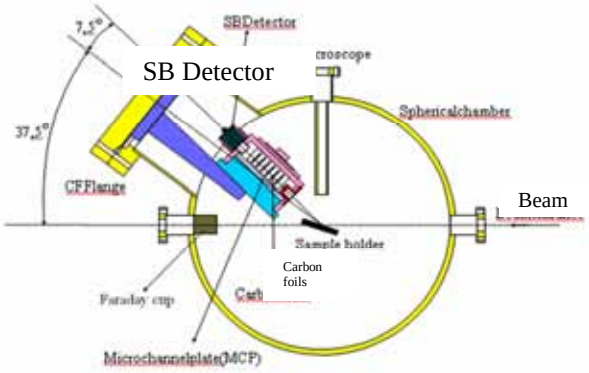

FIG. 2. The layout of the IEE ERDA system in the scattering chamber. Recoil angle φ can be selected to be either 30° or 45°, by rotating the flange for 180°.

The detection system is mounted on the CF100 flange at 37.5° port with respect to the beam direction. By rotating the flange for 180°, two detection angles φ for ERDA analysis can be selected, namely 30° and 45° as can be seen from Fig. 2. The positioning of the sample was done using an optical microscope whose focus defines a center of the chamber. The solid angle of the IEE ERDA system is about 1.3 msr (2 mm diameter and 50 mm distance of entrance collimator from the sample surface). With the scan control system it is possible to choose different scan speeds that can be useful to reduce possible sample damage. The typical scan speed used in all experiments was about 2 ms/pixel. The computer code SIMNRA [16] was chosen for evaluation and quantification of data obtained by IEE ERDA measurements.

3. RESULTS AND DISCUSSION

3.1 TOF-ERDA analysis of the implanted Si sample with 10 keV H- ions

The measurement of the a-Si sample was performed before H implantation in order to determine the hydrogen background in a non-implanted Si sample. The measured values show surface contamination of 12.9 at. % H (assuming that surface layer consist H, C, O and Si), and a homogeneous background concentration of 0.037 at. % H throughout the 300 nm layer. Most likely this background is belonging to the tail of the surface hydrogen peak. This background contribution was later subtracted from spectra measured after H implantation.

Fig. 3a) shows Time-of-Flight vs. Energy coincidence spectrum of a Si sample implanted with 10 keV H- ions.

In the figure, some C and O surface contamination can be clearly seen. The projection of hydrogen events on the time axis is displayed in Fig. 3b) where it can be seen that the implanted H peak with a maximum at 132 nm (assuming pure Si density of ρ=2.32 g/cm^3) is well separated from the surface H peak. We believe that the origin of the surface H peak is due to contamination either induced during the implantation process from the vacuum pumping system or from water adsorbed at the surface during sample handling.

Figure 4 shows a comparison of the measured implanted profile done by direct conversion with CORTEO and SRIM simulations.

Measured implanted profile is in good agreement with the simulated one and measured implanted H concentration (1.67×1016 at./cm^2) is about 16% lower than nominal (2×10^{16} at./cm^2) [17]. A deviation of the measured implanted concentration for H from the nominal concentration is expected. It is caused by the area of the implanted surface not being well-defined, as well as possible inaccurate charge collection, since implantation was performed using an ion source rather than a professional implanter.

Some materials lose hydrogen during analysis. Hydrogen release from the samples during heavy ion bombardment can be very rapid (e.g. biological samples and polymers) or can be negligible (e.g.TiH_2) depending on the nature of the material. Therefore, it is important to monitor hydrogen behavior in the sample during ion beam bombardment. To evaluate the beam related H release during the TOF-ERDA measurement, the yield of detected hydrogen was measured as a function of incident ion fluence. Implanted H sample was irradiated with the 127I beam (energy 20 MeV), and a spectrum was collected in list mode [17]. Separately implanted and surface hydrogen peaks are studied. Results for hydrogen stability vs. beam fluence for both peaks are shown in Fig. 5.

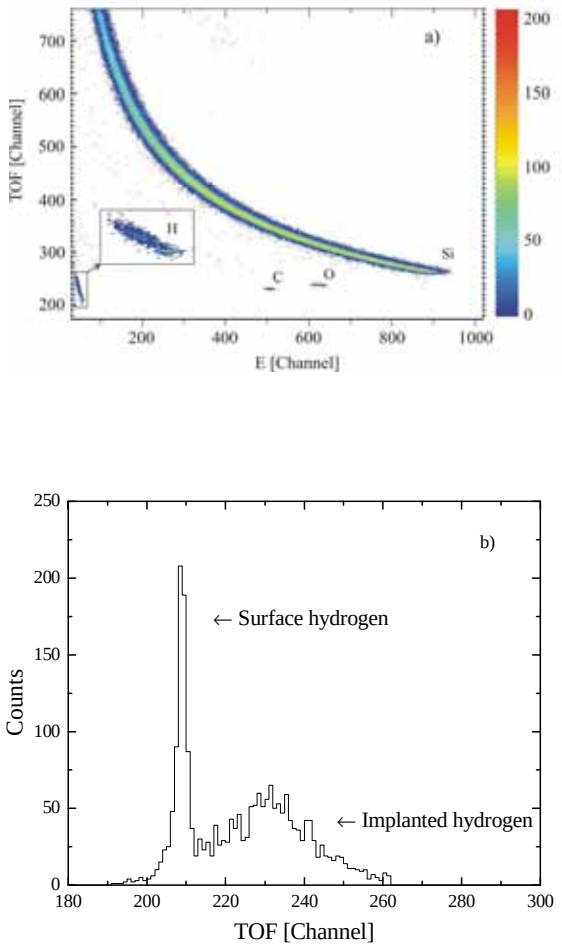

FIG. 3. a) TOF-ERDA coincidence spectrum of a hydrogen implanted a-Si sample, b) Projection of hydrogen events on the time axis.

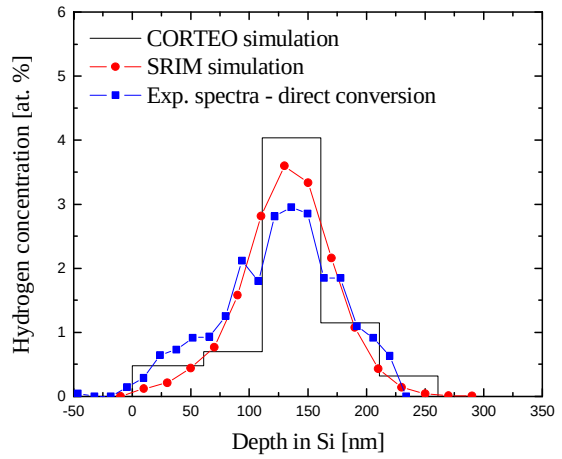

FIG. 4. Depth profile of the implanted hydrogen sample.

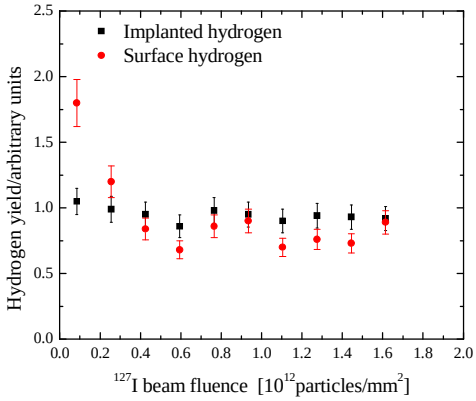

FIG. 5. Dependence of the normalized hydrogen yield with ion beam fluency for H implanted and surface peak in an Si sample.

As can be observed, the fluence-dependent decrease of the implanted peak yield during the total measuring time was relatively low and can be neglected. Contrary to the implanted peak, surface peak shows decrease of the yield with the ion fluence. After some beam fluence (0.5×10^{12} particles/mm^2) surface peak yield becomes constant. As hydrogen surface peak is coming from the sample surface contamination by organic molecules (water and/or hydro-carbons) coming from the vacuum, it is less bonded and easier released during heavy ion bombardment.

Hydrogen contamination of the used amorphised Si sample was 0.04 at. %. Because of that sensitivity for hydrogen in a-Si was estimated from the background coming from incidental coincidences surrounding hydrogen events to be ~ 25 ppm.

A surface depth resolution of 16 nm was calculated from the surface H peak, and the conversion to depth was obtained using the surface approximation [18].

3.2 IEE ERDA analysis of the implanted Si sample with 25 keV H- ions

To test the depth profiling abilities of IEE ERDA system, a silicon sample implanted with 5×10^{16} H at/cm^2 was produced using 25 keV protons from the ion source. According to SRIM [14] calculations, the maximum concentration of H is at the position of 280 nm below the sample surface and is equal to about 7.6 at.%. ERDA measurements were performed with 4.5 MeV $^{16}O^{3+}$ ions at a recoil angle of 30° and a sample tilt of 15°. Figure 6 shows the obtained 2D IEE ERDA spectrum.

As can be seen from the figure, two H peaks are present: one at the surface and one corresponding to the implanted hydrogen. We believe that the surface peak is due to the contamination, either induced during the implantation process from the vacuum pumping system or due to water adsorbed at the surface during sample handling.

The first step in the data analysis is to project all events belonging to H onto the energy axis. After that, an energy calibration of the spectrum was done. Next step was to correlate the detected H energies with the depths from which the H atoms have emerged. The resulting H depth profile is shown on Fig. 7 together with the profile calculated by SRIM [10].

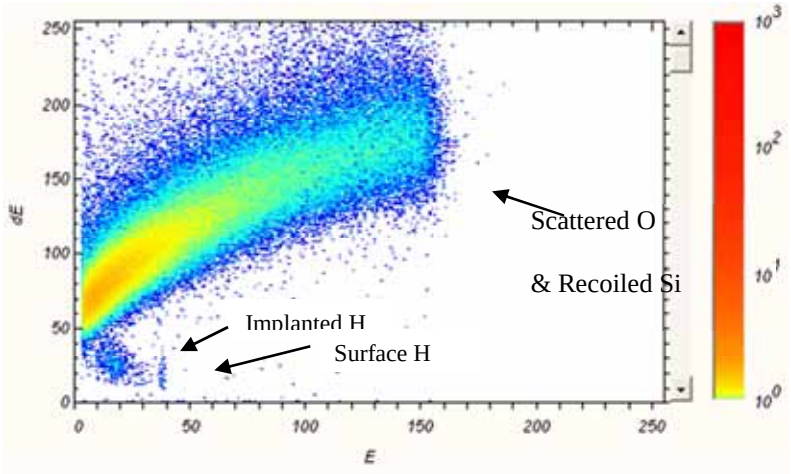

FIG. 6. Two dimensional IEE ERDA map of the Si sample implanted with 5×10^{16} H at/cm^2. Events coming from implanted H are inside the marked polygon. The measurements were performed with 4.5 MeV $^{16}O^{3+}$ ions at a recoil angle of 30° and a sample tilt of 15° towards the beam direction.

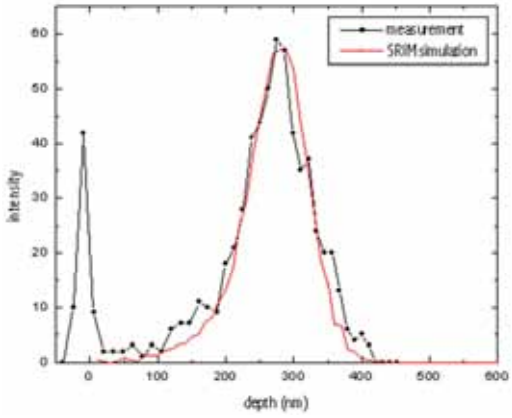

FIG. 7. Measured H depth profile together with the profile obtained by SRIM.

It can be seen that both profiles are in very good agreement. From the surface contamination peak depth resolution near to the sample surface was calculated to be about 20 nm. To obtain sufficient data statistics in the implanted peak as is shown on Figs. 6 and 7 a sample area of 50×500 μm^2 was irradiated with about 10 pÅ current for a collection time of 830 sec. For those experimental conditions and taking into account the number of background counts minimum detection limit for H detection in Si sample was estimated to be 3×10^{15} at/cm^2.

In order to test the imaging abilities of the ERDA system, we have analysed a 3D structure which was produced by implanting 25 keV protons into the Si substrate, but this time through a 200 mesh cooper grid [10]. For imaging, the ERDA recoil angle φ was changed to 45° and the tilt angle to 22.5°. From the total spectrum of hydrogen recoils, the total implanted dose was estimated to be 2×10^{17} at/cm^2. The maximum concentration of H equals to about 25 at%. The peak maximum was again placed 280 nm below the sample surface. As every event in the 2D ERDA spectrum has its own depth (z) as well as the areal (x,y) position a 3D distribution of hydrogen can be extracted. Figure 8 shows projection of all events that correspond to depths between 200 and 350 nm in the 470×510 μm^2 sample area.

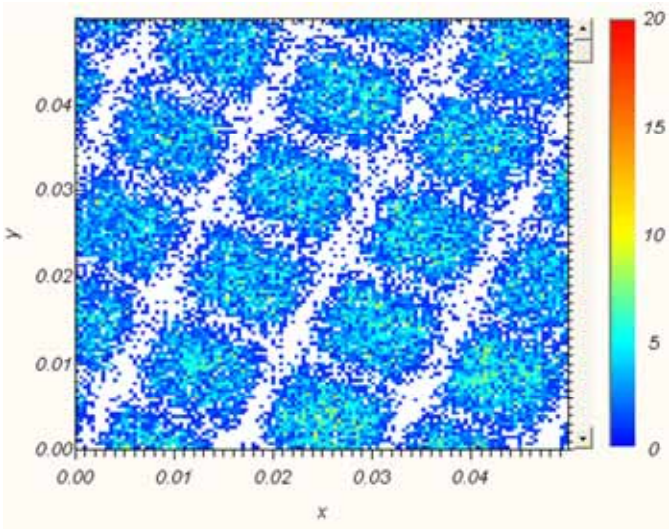

FIG. 8. 3D distribution of H in a Si sample implanted with 25 keV H ions through a mask (200 mesh Cu grid). The figure displays only events belonging to the implanted profile and coming from depths between 200 and 350 nm. The scan size was 470×510 μm^2.

Similar images can be obtained for any layer of the sample down to 350 nm depth. For this measurements a 4 MeV $^{16}O^{3+}$ beam focused to 15×15 μm^2 beam spot was used. The total collected charge was about 6.5 μC and the current was about 350 pA (current density about 1.5 pA/μm^2). By analyzing data offline in replay mode two parameters were examined: (1) The H yield remained stable within 3% and (2) no shift of the implanted profile with time was observed.

4. CONCLUSIONS

In the present work, we have shown that with LiF covered DLC foils in the TOF-ERDA timing stations, the detection efficiency for 400 keV protons is around 60%. This efficiency is sufficient that quantitative analysis of hydrogen and its isotopes can be performed simultaneously with all other lighter elements in the sample in a single TOF ERDA measurement.

The main advantages of the TOF-ERDA system are: very good hydrogen sensitivity (down to ppm range) and good hydrogen depth resolution (~15 nm close to the surface). Another important advantage of TOF-ERDA is that only one measurement per sample is required and all other lighter elements in the sample can be detected simultaneously.

IEE ERDA measurements were performed with a rather poor focus of d > 10 μm few MeV oxygen ions and current densities around 1 pA/μm^2. It was shown that for applied experimental conditions the IEE ERDA system can be used for 3D imaging of samples containing about 10 at.% of hydrogen with the lateral resolution of 15×15 μm^2. With a newly installed quintuplet focusing system this resolution now goes below 1×1 μm2. Detection limits for non-imaging mode, such as 50×500 μm^2 well defined slit mode are significantly lower and correspond to about 3×10^{15} at/cm^2 near to the sample surface. The best obtained depth resolution close to the sample surface was found to be about 20 nm.

REFERENCES

[1] GROLEAU, R., GUJRATHI, S.C., MARTIN, J.P., Nucl. Instrum. Methods Phys. Res. **218** (1983) 11.

[2] THOMAS, J.P., FALLAVIER, M., RAMDANE, D., CHEVARIER, N., CHEVARIER, A., Nucl. Instrum. Methods Phys. Res. **218** (1983) 125.

[3] WHITLOW, H.J., POSSNERT, G., PETERSSON, C.S., Nucl. Instrum. Methods Phys. Res., Sect. B **27** (1987) 488.

[4] ZHANG, Y., et al., J., Nucl. Instrum. Meth. Phys. Res., Sect. B **149** (1999) 477.

[5] KOTTLER, C., DÖBELI, M., GLAUS, F., SUTER, M., Nucl. Instrum. Methods Phys. Res., Sect. B **248** (2006) 155.

[6] BOHNE, W., RÖHRICH, J., RÖSCHERT, G., Nucl. Instrum. Methods Phys. Res., Sect. B 139 (1998) 219.

[7] SIKETIĆ, Z., BOGDANOVIĆ RADOVIĆ, I., JAKŠIĆ, M., Nucl. Instrum. Methods Phys. Res., Sect. B **266** (2008) 1328.

[8] GIANGRANDI, S., et al., Nucl. Instrum. Methods Phys. Res., Sect. B **266** (2008) 5144.

[9] BENKA, O., BRANDSTÖTTER, A., STEINBAUER, E., Nucl. Instr. and Methods B**136-138** (1998) 695.

[10] BOGDANOVIĆ RADOVIĆ, I., MEDUNIĆ, Z., JAKŠIĆ, M., SIKETIĆ, Z., SKUKAN, N., Nucl. Instr. and Meth. B **231** (2005) 123.

[11] BOGDANOVIĆ RADOVIĆ, I., STEINBAUER, E., BENKA, O., Nucl. Instr. and Methods B **170** (2000) 163.

[12] YANG, C., et al., Nucl. Instr. and Methods B **158** (1999) 706.

[13] BUSCH, F., PFEFFER, W., KOHLMEYER, B., SCHÜLL, D. PÜHLHOFFER, F., Nucl. Instrum. Methods Phys. Res. **171** (1980) 71.

[14] ZIEGLER, J.F., Nucl. Instrum. Methods Phys. Res., Sect. B **219** (2004) 1027.

[15] SCHIETTEKATTE, F., Nucl. Instrum. Methods Phys. Res., Sect. B **266** (2008) 1880.

[16] MAYER, M., Technical Report IPP 9/113, Max-Planck Institut fur Plasmaphysik, Garching, Germany, 1997.

[17] SIKETIĆ, Z., BOGDANOVIĆ RADOVIĆ, I., JAKŠIĆ, M., Thin Solid Films **518** (2010) 2617.

[18] CHU, W.K., MAYER, J.W., NICOLET, M.A., Backscattering Spectrometry, Academy Press, New York, 1978.

NEUTRON REFLECTOMETRY: A UNIQUE TOOL TO DETERMINE THE HYDROGEN PROFILE IN THIN FILMS

H. FRITZSCHE[1], J. HAAGSMA[2], C. OPHUS[2], E. LUBER[2], T. HARROWER[2], D. MITLIN[2]
[1]National Research Council Canada, Canadian Neutron Beam Centre, Chalk River Laboratories, Chalk River, ON, K0J 1J0
[2]Chemical and Materials Engineering, University of Alberta, and National Research Council Canada, NINT, Edmonton, AB
Canada
helmut.fritzsche@nrc.gc.ca

Abstract: In this report we show how Neutron Reflectometry (NR) can provide deeper insight into the absorption and desorption properties of commercially viable hydrogen storage materials. NR benefits from the large negative scattering length of hydrogen atoms which changes the reflectivity curve substantially so that NR can determine not only the total amount of stored hydrogen but also the hydrogen distribution with nanometer resolution along a direction normal to the film. In order to use NR, the samples must have smooth surfaces and the film thickness should range between 10 and 200 nm. Our NR experiments on thin MgAl alloy films, capped with a Pd catalyst layer, enabled us to determine the structural changes in these thin MgAl alloy films after absorption and during hydrogen desorption. The thin films expand by about 20% due to hydrogen absorption and the hydrogen is stored only in the MgAl layer with no hydrogen content in the Pd layer. Furthermore, the NR measurements clearly show that a prolonged annealing of the films at temperatures above 473 K lead to an interdiffusion of the Pd layer with the MgAl layer which would make them non-recyclable.

1. INTRODUCTION

A modern vehicle would need about 5 kg of hydrogen in combination with a fuel cell or an Internal Combustion Engine (ICE) to achieve a reasonable travel range. Intense research efforts have been focused on how to store the hydrogen in increasingly smaller volume with decreasing weight of the whole hydrogen storage system. The goal is to find a material that would meet the stringent DOE technical targets for on-board hydrogen storage systems: a gravimetric capacity of 6 wt.% hydrogen, fast absorption (3 minutes to refill the tank with 5 kg hydrogen), desorption in a temperature range between -30°C and 85°C, and a recyclability of at least 500 times. There are many different paths that have been followed in the past to store hydrogen. The most investigated being: compressed gas; chemical binding in metal hydrides; liquid hydrogen (LH_2); physical adsorption in porous materials, and via encapsulation in molecular cages. All methods and materials have their specific advantages and disadvantages, for a review see e.g. [1, 2].

The metal hydrides, in which the hydrogen is chemically bound to a metal atom, are very promising candidates because they can hold up to 10 wt.% hydrogen. The main disadvantage with this group of materials is that the hydrogen is bound too strongly and it therefore needs high temperatures to release the hydrogen. A strategy called ‘destabilization’ has been pursued in the past in order to reduce the hydrogen binding energy. This has been achieved by adding other elements to the hydrogen storing host material or using high-energy ball milling to create nano-crystals [3-8]. Recently, co-sputtering of Mg and Al has been used to destabilize the Mg matrix and create nanocrystalline or amorphous thin films [9, 10]. Thin films are ideal model systems because the preparation is very reproducible and it is possible to easily change the film structure (e.g. catalyst layer) in a well-defined way. Only recently we have successfully applied neutron reflectometry (NR) to determine the hydrogen profile in thin MgAl alloy films with nanometer resolution [11].

2. THEORETICAL DESCRIPTION OF NEUTRON REFLECTOMETRY

The scattering geometry of a typical reflectometry experiment is shown in Fig. 1. The neutron beam hits the surface at an angle θ and is specularly reflected off the sample at the same angle θ. The intensity is measured as a function of the so-called scattering angle θ, which is typically in the range between 0 and 2°. The interfaces of the samples are arranged perpendicular to the scattering vector

$$|\vec{q}| = \left|\vec{k}_r - \vec{k}_i\right| = \frac{4\pi}{\lambda}\sin(\theta) \tag{1}$$

with $\vec{k}_i$ and $\vec{k}_r$ being the incoming and reflected neutron wave vector and λ the neutron wavelength. The interaction with the film is reduced to a one-dimensional problem and it can be described for grazing incidences with an effective potential V_j in layer j given by [12]:

$$V_j = \frac{2\pi\hbar^2}{m} N_j b_j \tag{2}$$

where m, N_j, and b_j, denote the neutron mass, atomic density, and coherent nuclear scattering length in layer j. This so-called Fermi pseudopotential V_j describes the interaction of the neutron with the nucleus, and the product $N_j b_j$ is known as the scattering length density (SLD). The SLD depends on the elements and their isotopes in the sample [12]. Hydrogen has a large negative scattering length. Therefore, the SLD of any material absorbing hydrogen decreases substantially and leads to a significant change in the reflectivity curve. This change of the SLD of a Mg film on a Si substrate is depicted in Fig. 2, where the unsorbed Mg film is shown in (a), a film with an atomic ratio of H/Mg = 1 is shown in (b) and a pure MgH_2 film is shown in 2(c). As can be seen from the diagram, the SLD of MgH_2 is negative.

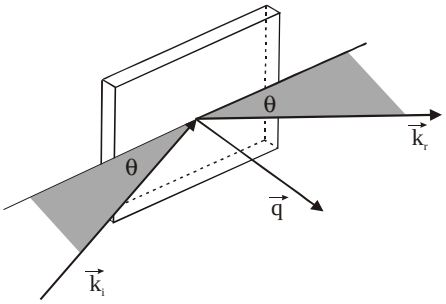

FIG. 1. Scattering geometry for a reflectometry experiment with the wave vector k_i of the incoming wave, the wave vector k_r of the reflected wave, the scattering vector q, and the scattering angle θ.

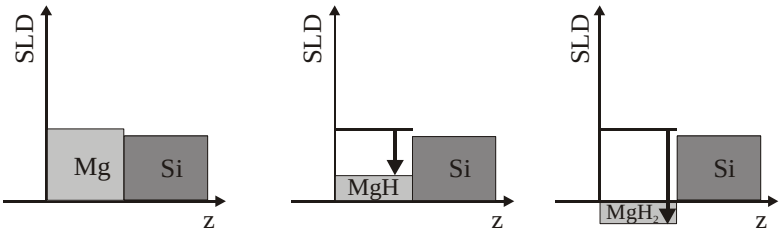

FIG. 2. SLD profile of a) a Mg film, b) a Mg film with a ratio of H/Mg = 1, and c) a MgH_2 film on a Si substrate.

The reflectivity of the sample at a certain scattering angle θ can be calculated by solving the Schrödinger equation using the potential as defined in Eq.(2) and the kinetic energy of the incident neutron as calculated from the scattering angle θ. The simulations presented here were calculated with a software based on the Parratt formalism [13, 14]. The reflectivity curves resulting from the SLD profiles in Fig. 2 are shown in Fig. 3. The solid line corresponds to the unsorbed Mg film, the dashed line to a film with a ratio of H/Mg = 1, and the open circles to a MgH_2 film on a Si substrate. For all simulations the film thickness was kept constant at 30 nm. As can be seen in Fig. 3, the reflectivity curves contain a series of maxima and minima, the so-called Kiessig fringes [15].

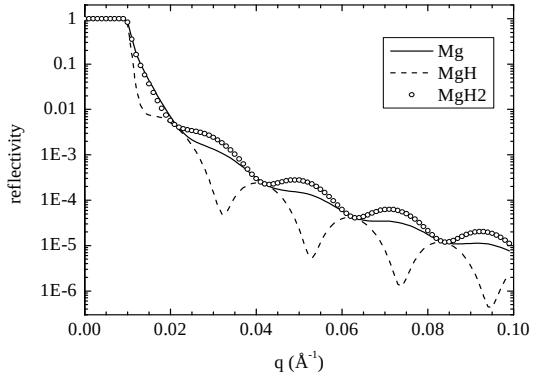

FIG. 3. Neutron Reflectivity curves simulated from the SLD profiles shown in Fig. 2 for a 30 nm Mg film (solid line), a 30 nm Mg film with H/Mg = 1 (dashed line), and a 30 nm MgH_2 film on a Si substrate (open circles).

In general, the observation of oscillations in a reflectivity curve corresponds to a characteristic thickness in the specimen. The oscillations observed in Fig. 3 correspond to the 30 nm film thickness. It is worthwhile to note that for all reflectivity curves in Fig. 3 the distance Δq between the minima is identical. The absolute position of the minima and maxima, however, is different. In Fig. 3 the maxima of the curve for the film with H/Mg = 1 coincides with the minima of the MgH_2 curve. That nicely demonstrates the high sensitivity of a NR curve to the hydrogen content in a thin film. So, by fitting the measured NR curve it is possible to determine very accurately the hydrogen content in a thin film in a thickness range from about 1 to 200 nm. This will be shown in the next section, where we present our NR data on thin MgAl films.

3. EXPERIMENTAL RESULTS ON MGAL THIN FILMS

The films were co-sputtered onto a Si(100) substrate with a native oxide layer of about 1 nm thickness. The Mg sputter rate was held constant at 0.4 nm/s, the sputter rate of Al adjusted for the different compositions, and the Pd was sputtered at a rate of 0.1 nm/s. We used Ar gas with a purity of 99.999% at a pressure of 5.3×10^{-3} mbar, with a maximum base pressure of 2.7×10^{-7} mbar. The MgAl films had a thickness of about 52 nm and were covered with a 10 nm thick Pd layer in order to facilitate the hydrogen uptake [16]. The films were absorbed with hydrogen in a dedicated high-pressure furnace at 430 K for 20 hours at 68 bar.

In Fig. 4 the experimental data are shown for a $Mg_{0.7}Al_{0.3}H_y$ film a) before, b) after hydrogen absorption, and c) after complete hydrogen desorption at 448 K. For the desorption experiments the samples were heated up to the desired temperatures, held at that temperature for one hour, and then the measurements were started and performed at that temperature for about 11 hours. All the reflectivity curves show the aforementioned Kiessig oscillations,

which are due to the total film thickness, i.e. the MgAl plus the Pd layer. The changes in the film structure due to hydrogen uptake can be best visualized by plotting the SLD profile, i.e. the SLD along the surface normal z of the film. The SLD profiles corresponding to the fits are shown in Fig. 4 as insets. By comparing the SLD profiles before and after hydrogen absorption, you can easily conclude an expansion of about 20% for both the Pd and MgAl layer. The SLD of the MgAl layer before absorption is 2.2×10^{-6} Å^{-2}, which represents the theoretical value for a hydrogen-free sample and shows that there has been no hydrogen introduced into the sample during the preparation process. From the shown SLDs it is obvious that no hydrogen is stored in the Pd cover layer. This has also been observed in Pd-covered Fe/Nb multilayers [17]. The amount of hydrogen absorbed into the MgAl layer can be determined from the decrease of the SLD of the desorbed film due to the large negative scattering length of the hydrogen, b_H = -3.739 fm [12]. The SLD of a $Mg_{1-x}Al_xH_y$ film is given by:

$$SLD_H = \rho N_A \frac{(1-x)b_{Mg} + xb_{Al} + yb_H}{(1-x)u_{Mg} + xu_{Al} + yu_H} \tag{3}$$

with the density ρ, the Avogadro constant N_A, and the molar weights u_{Mg}, u_{Al}, and u_H, respectively. As ρ changes due to the expansion of the film we assumed a density change inversely proportional to the film thickness. The hydrogen content y can then be calculated as follows [17]:

$$y = \left(\frac{SLD_H}{SLD_0} \frac{t}{t_0} - 1 \right) \frac{(1-x)b_{Mg} + xb_{Al}}{b_H} \tag{4}$$

with SLD_H and t being the SLD and thickness of the absorbed film and SLD_0 and t_0 being the SLD and thickness of the as-prepared film. The hydrogen weight percent can then be calculated as 100 $(y\ u_H)/((1\text{-}x)u_{Mg} + x\ u_{Al} + y\ u_H)$. The SLD of the $Mg_{0.7}Al_{0.3}$ film changes from 2.2×10^{-6} Å^{-2} for the unsorbed film to 4.2×10^{-7} Å^{-2} for the fully sorbed film corresponding to 4.1 wt% stored hydrogen.

NR is capable of determining film thickness changes and hydrogen uptake as shown above. Furthermore, NR can detect more subtle changes of a film structure like interdiffusion of one material into another one. This was observed in a desorbed Pd-covered $Mg_{0.7}Al_{0.3}$ film when annealing the film at 473 K. Figure 5 shows the NR scans for an annealing time of a) 1, b) 3, and c) 9 hours [18]. The corresponding SLD profiles are shown in the insets. In order to fit the data properly we had to describe the SLD profile of the sample with a 7 box model. In this model the sample was divided up into seven independent layers and for each box the SLD, thickness, and interface roughness were varied to optimize the fit. With the 3 box model that we successfully applied to fit the data presented in Fig. 4 (1 box for the SiO_2, 1 box for the MgAl, and 1 box for the Pd) it was no longer possible to fit the data from the annealed film. As can be deduced from Fig. 5a, there is no hydrogen left in the MgAl film after 1 h annealing at 473 K. After 3 h (Fig. 5b), the SLD at the location of the Pd layer had decreased from 4 to 3.5×10^{-6} Å^{-2} and at the same time the SLD of the MgAl in contact with the Pd layer had increased. This certainly proves the Pd interdiffusion into the MgAl layer. After 9 h annealing (Fig. 5c) the Kiessig fringes are no longer visible which means that the Pd layer has diffused into the MgAl layer.

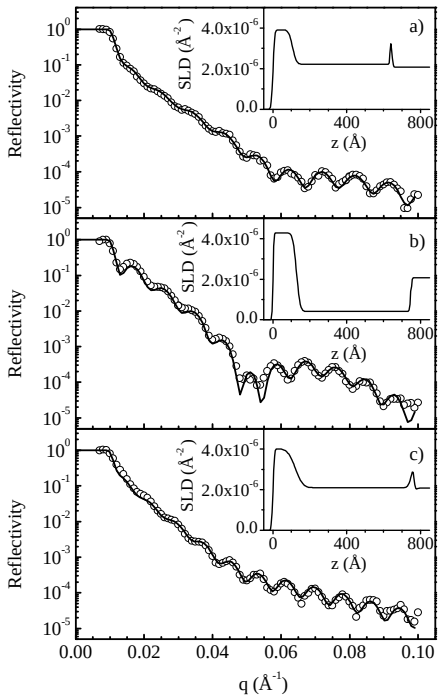

FIG. 4. Neutron Reflectivity curves of a Pd-covered $Mg_{0.7}Al_{0.3}H_y$ thin film on a Si substrate a) before hydrogen absorption (y=0), measured at 295 K; b) after hydrogen absorption (y=1.1), measured at 295 K; and c) after hydrogen desorption, measured at 448 K (y=0). The open circles represent experimental data, the solid lines represent fits, and the insets show the corresponding SLD profile. Taken from H. Fritzsche et al. [11].

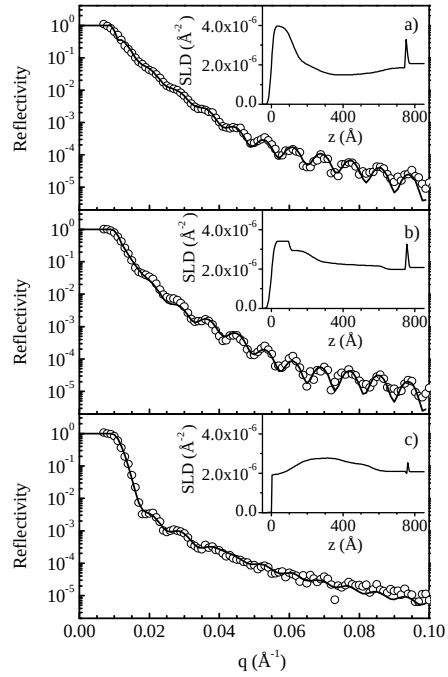

FIG. 5. Neutron Reflectivity curve of a Pd-covered $Mg_{0.7}Al_{0.3}H_y$ thin film on a Si substrate a) after 1 h, b) after 3 h, and c) after 9 h annealing at 473 K. The open circles represent experimental data, the solid lines represent fits, and the insets show the corresponding SLD profile. Taken from H. Fritzsche et al. [18].

4. CONCLUSIONS

We have shown how neutron reflectometry can be used to determine the hydrogen profile in thin films along with the structural changes of the film during hydrogen absorption and desorption. This information is invaluable for the optimization of hydrogen storage materials. Our experiments on Pd-capped $Mg_{0.7}Al_{0.3}$ films show that the hydrogen is homogeneously dispersed within the MgAl layer with an appreciable 4.1 wt% stored hydrogen. By annealing the films at 473 K for more than 9 hours, the film structure is destroyed by interdiffusion of the Pd into the MgAl layer. These structural changes are important in terms of recyclability of a hydrogen storage material.

REFERENCES

[1] SCHLAPBACH, L., ZÜTTEL, A., Nature **414** (2001) 353.
[2] VAN DEN BERG, A.C., AREAN, C.O., Chem. Commun. **668** (2008).
[3] ZALUSKA, A., ZALUSKI, L., STRÖM-OLSEN, J.O., Appl. Phys. A **72** (2001) 157.
[4] DORNHEIM, M., EIGEN, N., BARKHORDARIAN, G., KLASSEN, T., BORMANN, R., Adv. Eng. Mater. **8** (2006) 377.
[5] ORIMO, S., et al., Acta Mater. **45** (1997) 2271.
[6] CUI, N., HE, P., LUO, J.L., Acta Mater. **47** (1999) 3737.
[7] ZALUSKA, A., ZALUSKI, L., STRÖM-OLSEN, J.O., J. Alloys Comp. **289** (1999) 197.
[8] YONKEU, A.L., SWAINSON, I.P., DUFOUR, J., HUOT, J., J. Alloys Compd. **460** (2008) 559.
[9] GREMAUD, R., et al., Appl. Phys. A **84** (2006) 77.
[10] GREMAUD, et al., J. Alloys Compd. **404-406** (2005) 775.
[11] FRITZSCHE, H., et al., Appl. Phys. Lett. **92** (2008) 121917.
[12] SEARS, V.F., Neutron News **3** (1992) 26.
[13] PARRATT, L.G., Phys. Rev. **95** (1954) 359.
[14] Software Parratt32 developed by C. Braun for BENSC, HMI, http://www.hmi.de/bensc/instrumentation/instrumente/v6/refl/parratt_en.htm (1999).
[15] KIESSIG, H., Annalen der Physik, ser. 5, **10** (1931) 769.
[16] PICK, M.A., DAVENPORT, J.W., STRONGIN, M., DIENES, G.J., Phys. Rev. Lett. **43** (1979) 286.
[17] REHM, C., FRITZSCHE, H., MALETTA, H., KLOSE, F., Phys. Rev. B **59** (1999) 3142.
[18] FRITZSCHE, H., et al., Nucl. Instr. Meth. A **600** (2009) 301.

THE STUDY OF SPECIAL FEATURES OF STRUCTURAL TRANSFORMATIONS AT THE HYDROGENATION OF FULLERITE C_{60}

D.V. SCHUR[1], S.Y. ZAGINAICHENKO[1], A.F. SAVENKO[1],V.A. BOGOLEPOV[1], N.S. ANIKINA[1], A.D. ZOLOTARENKO[1], Z.A. MATYSINA[2], T. NEJAT VEZIROGLU[3], N.E. SKRYABINA[4]
[1]Institute for Problems of Materials Science of NAS of Ukraine, Krzhyzhanovsky str. 3, 03142 Kiev, Ukraine
[2]Dnepropetrovsk National University, 72 Gagarin str., Dnepropetrovsk, 49000 Ukraine;
[3]International Association for Hydrogen Energy, 5794 SW 40 St. #303, Miami, Fl 33155, USA
[4]Perm State University, Bukireva str., 15, Perm, 614990 Russian Federation
shurzag@ipms.kiev.ua

Abstract: The fullerene is the fourth allotropic modification of carbon and its properties, as volume, gravimetric and electrochemical capacities, are in excess of many similar properties of metal hydrides and hydrocarbons. The solution of the problem of the reversible hydrogenation of each carbon atom in the frame of fullerene molecule will allow to create the hydrogen storage with the capacity up to 7,7 wt.% H. A series of experiments have been conducted to evaluate the full hydrogenation of fullerite C_{60}; hydrofullerenes have been produced experimentally with the variable content of hydrogen. The optimum regime of C_{60} hydrogenation has been determined resulting in the full hydrogenation of fullerene molecule C_{60}. As was apparent after the tests, the sequence of formation of hydrogenated fullerene molecule $C_{60}H_{60}$ in fullerite has been going in the following order: the molecular hydrogen dissolution in octahedral interstices of fcc lattice of fullerite, the dissociation of hydrogen molecules in going from octa- to tetrahedral interstices, the interaction of hydrogen atoms with fullerene molecule. It has been demonstrated that chemisorption process of hydrogen by molecule C_{60} is limited by diffusive processes in fullerite after hydrogen concentration conformed to $C_{60}H_{36}$. The spectral analysis has shown that the second stage process of chemisorption follows the compressive shell model. The suggestion of the model of processes going on at the interaction between H_2 and fullerite C_{60} has been made. The mechanism for the definition of hydrogenation degree of molecule C_{60} has been proposed in the present paper.

1. INTRODUCTION

It is well known that, fossil fuels resources – headed by petroleum and natural gas – are being depleted rapidly and the environmental problems (climate change, acid rains, ozone layer depletion, pollution, oil spills, etc.) caused by their utilization are increasing. Rising energy prices and the growing environmental damage are hurting the economies of the developing countries mainly, and the income per capital gap between industrial countries and developing countries is widening. This is causing many problems between the developing countries and the industrial countries, including ever-growing illegal immigration to industrial countries such as EU and USA

The Hydrogen Energy System is the permanent answer to these interrelated global problems. Under this system, each country will be able to produce the fuel it needs, i.e. hydrogen, to power its economy, using the primary energy sources available. Therefore, they will not be affected by the rising energy prices and will not spend foreign exchange to import petroleum and/or natural gas. This will speed up their economic growth and at the same time eliminate the environmental damage. Consequently, the Hydrogen Economy will help developing countries develop faster, protect the environment, and eliminate the tension between the developing countries and the industrially developed countries.

The hydrogen safe storage and transportation are the problems restrained the introduction of hydrogen energetics. Solving this problem can contribute considerably to the fast progress of hydrogen at the power market. The hydrogen storage in solids meets the requirements and supply most of the needs of life. The hydrogen density in the volume unit for the majority of hydrides exceeds the density of liquid hydrogen. The bulk of such materials are not explosive, containers for their storage are compact and cheap and it is less of a problem for these containers transit than that during liquid and gaseous hydrogen transportation.

The recently found fourth allotropic modification of carbon, as fullerene, can be one of such materials. As pointed out in [1], the fullerite properties, as volume ($8.25 \cdot 10^{22}$ H atoms/cm^3), gravimetric (7.7 wt.% H) and electrochemical (2000 mA/h·g) capacities, exceed many similar properties of metal hydrides and hydrocarbons. The solution of the problem of the reversible hydrogenation of each carbon atom in the frame of fullerene molecule will allow to create the hydrogen storage with the capacity up to 7.7 wt.% H.

Over the last two decades, a great number of papers were devoted to the solution exactly of this problem [2-17]. In our papers [1, 18] we specified that hydrogen in fcc lattice of fullerite (fullerene in the solid state) can be in the lattice (absorbed) and fullerinated (chemisorption) states. As shown in the paper [19], the fcc fullerite lattice can contain 18 hydrogen atoms in the absorbed state per one molecule C_{60} at the temperature of $T \rightarrow 0$ K. However at the normal conditions only octa- and tetrahedral interstices, as positions of possible location of hydrogen atoms, are worth consideration. The theoretical justification of possibility of all carbon atoms hydrogenation in the fullerene structure is given also in this work.

The conditions of experiments and discussion of experimental results, received during the investigation of special features of processes of gaseous hydrogen interaction with fullerite, are being given in the present paper.

2. EXPERIMENTAL

2.1. Choosing the terms of experimental investigations

Considerable recent attention has been focused on the study of possible execution of full hydrogenation of fullerene molecule C_{60} [1-18]. However the final objective has not been achieved by none of these works. Only the scientific group of I.O. Bashkin [20] has succeeded the setted purpose not only for fullerite C_{60}, but also for CNT, nanofibres [21] and even as for graphite using hydrogen pressure about 7-9 GPa. Each carbon atom, formed one or another structure, has been hydrogenated in these experimental conditions, as it was reported in these papers.

Using high pressures for hydrogenation of fullerene molecules, researchers have mentioned that the process of hydrogenation causes often the destruction and fragmentation of fullerene molecules. Therefore, the optimum pressure of hydrogen is necessary for the performance of the experiment and this pressure must not break down the fullerene structure and at the same time must initiate the flowing of reaction between hydrogen and carbon atoms formed the fullerene frame.

The hydrogenation of fullerene molecule C_{60} on the Ru catalyst in the liquid phase up to the state of $C_{60}H^{48}$ at the pressure of 12.0 MPa has been gained by the authors of paper [4]. In this case, neither destruction nor fragmentation of fullerene molecules has been noted.

2.2. Determination of optimum temperature of interaction

The 75-hours experiment has been conducted for determination of the optimum regime of reaction carrying out on the fullerene molecule hydrogenation at the hydrogen pressure of 12 MPa. In the course of this experiment it has been elucidated the temperature at which the rate of hydrogen interaction with fullerene molecule is at its maximum. The construction and the operation of experimental installation were described in our paper [23]. The fullerite C_{60} sample of mass 0.5-1 g has been used in the experiment. The test specimen has been placed into the working ampoule in the experimental reactor from stainless steel. The reactor has

been vacuumized during one hour for the removal of impurities from fullerite. Thereafter the hydrogen has been supplied to reactor from metal-hydride accumulator up to the pressure of 12 MPa and conditioned for 4 hours (Fig. 1). Then, the temperature in reactor has been raised up to 200°C at the rate of 1°C/min. In doing so the pressure in reactor has been increased on 0.3 MPa, reached 12.8 MPa. This can be explained by the decomposition of solvates formed at the fullerite crystallization. For stabilization of the bar-temperature conditions the specimen has been kept for 4 hours more at the temperature of T = 200°C and the pressure of P = 12.8 MPa. At the 625 minute the rise of temperature in reactor has been continued from 200 to 600°C at the rate of 0.125°C per min.

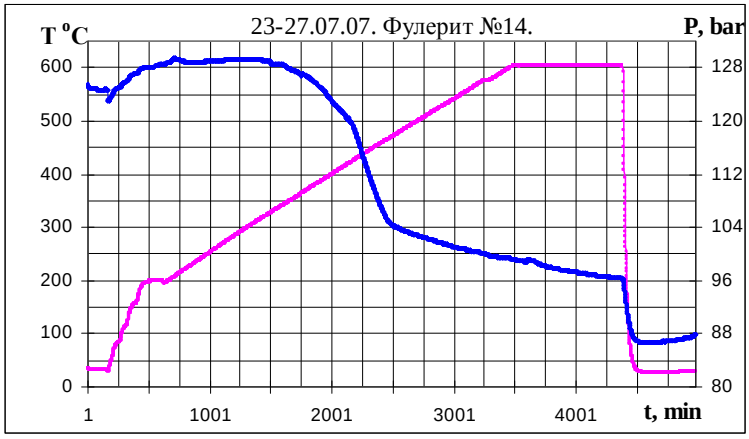

FIG. 1. The pressure change in reactor by varying the temperature at the rate of 0,125°C/min.: 1 – curve at pressure change in reactor; 2 – curve at temperature change in reactor.

During this experiment it has been found that the maximum rate of interaction has been reached at the 2250 minute (FIG. 2) that corresponds to the temperature of 433°C (Fig. 3). It should be pointed out that interaction rate has been sufficiently high over the interval between 2181 and 2410 minutes (about 4 hours) (Fig. 2). This rate has been at the temperature change from 425 to 455°C (FIG. 3). On further increase of temperature the interaction rate begins to reduce. In this experiment after 10 h of exposure at T = 200°C and P = 13 MPa the specimen mass has been changed on 0.6 wt.% (FIG. 4). The total amount of hydrogen absorbed by specimen has been fixed at the level of 8.2 wt.% H.

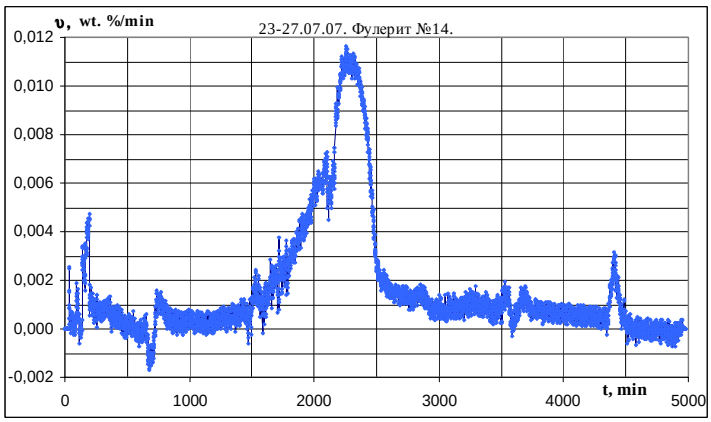

FIG. 2. The time-variation of the rate of fullerite C60 interaction (the rate of temperature growth from 200 to 600°C is 0,125°C/min.).

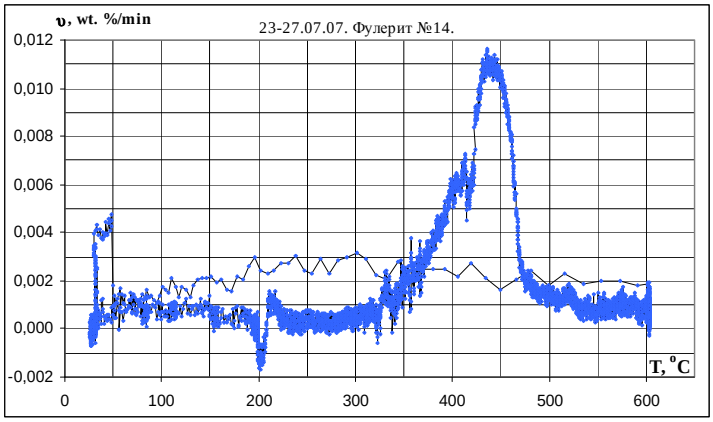

FIG. 3. The variation of the rate of interaction between fullerite C^{60} and hydrogen with the temperature.

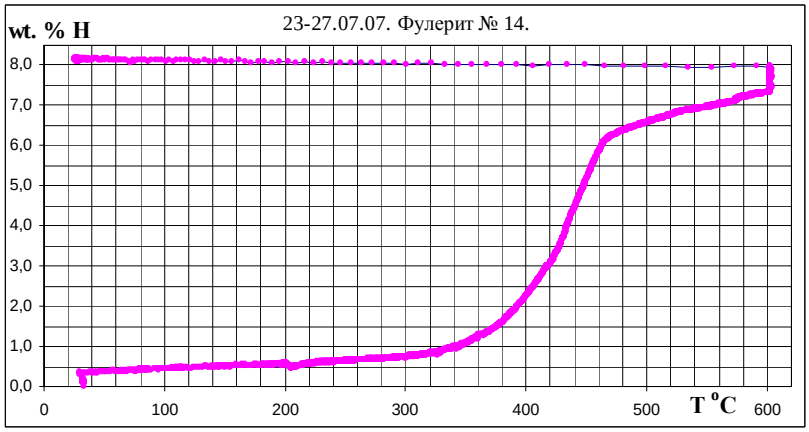

FIG. 4. The variation of specimen mass of fullerite with temperature in the course of experiment.

Another experiment (specimen №10) has shown that the prior annealing of fullerite in vacuum at T = 350°C brings about the more intensive interaction with gaseous hydrogen (Fig. 5). A quick-heating of specimen (over 3 h) up to the temperature of 550°C at hydrogen pressure of 12.5 MPa give rise to specimen saturation with hydrogen up to 7.3 wt.% H (Fig. 5, b) over this period. The further exposure at T = 550°C more than 65 h has not increased the hydrogen volume in specimen. Conceivably the portion of hydrogen has been absorbed by specimen in the initial stage (T = 350°C) at the hydrogen-filling of reactor.

The results of our experiments for specimen №9 (Fig. 5, c) are given for sample that was not annealed tentatively in vacuum. The characteristic splash of pressure in reactor initiated by hydrocarbons ejection at the heating up to 250°C has been seen in the curve ‘2’. The experiments have shown that for the removal of solvated hydrocarbon impurities from fullerite lattice it is sufficiently to heat up fullerite in vacuum over the temperature of 250°C. By virtue of the fact that initial stage of fullerite interaction with gaseous hydrogen remains the elucidated not to the end the necessity of more careful study of this interaction period arises.

(a)

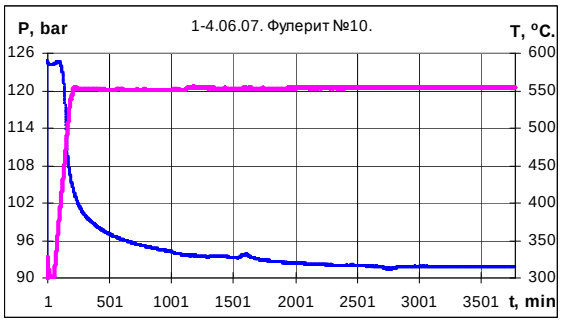

(b)

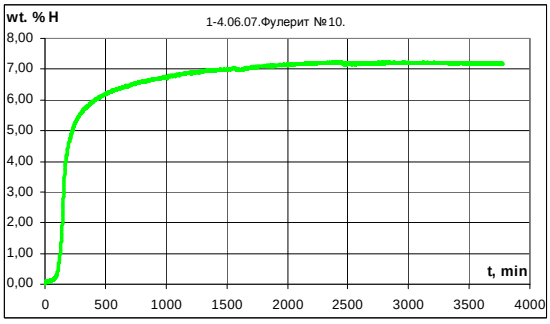

(c)

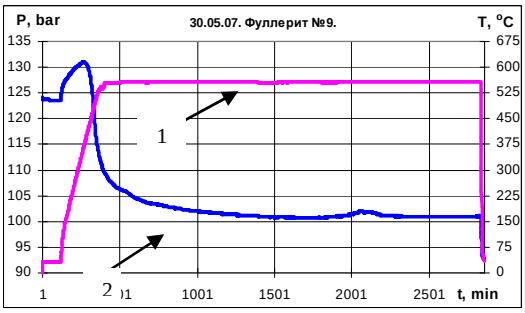

FIG. 5. The experimental curves represented the process of interaction of gaseous hydrogen with fullerite C60 (starting pressure Pst. = 12.5 MPa, final temperature Tfin = 550°C, a) the heating rate of 1.91°C/min.); (1a) the temporal changes in reactor temperature (2a) and b) pressure and mass of specimen №10 c) the temporal changes in reactor temperature (1) and pressure (2) for specimen №9.

2.3. Study of initial stage of interaction between gaseous hydrogen and fullerite

Since the foregoing investigations have determined that the optimum temperature of gaseous hydrogen interaction with fullerite (at P = 12-13 MPa) is the temperature range 425-455°C, all further study has been carried out under this conditions.

Before testing, the sample of fullerite (1 g) has been annealed in vacuum at the temperature T = 449°C over 1 hour. Thereafter hydrogen bleeding-in to reactor has been performed from metal-hydride accumulator up to the pressure P = 13 MPa.

In the course of experiments, we have studied main dependences (FIG. 6):

1. the time-dependence of fullerite mass change (Fig. 6, a, d);
2. the fullerite temperature modification in time (Fig. 6, b, e);
3. the time-change of hydrogen pressure in reactor (Fig. 6, c, f).

The data measurements have been conducted by computer program each minute. The supplementary lines ‘nm’ and ‘kl’ have been entered on the experimental curves of Fig. 6 (d, e, f) and this allows to ascertain the special features of processes under test.

The following peculiarities have been noted in studies of obtained data:

1. the mass change (OA) on 0.085 wt.% can attests the hydrogen adsorption on the surface of fullerite powder (Fig. 6(a));
2. exoeffect at the expense of pressure increase in reactor up to 130 MPa and H_2 absorption (section OA (3 min.) of Fig. 6(b)); lowering the temperature on 6^{o}C at the unchanged mass of specimen (section AB (7 min.) of Fig. 6(a));
3. Increase of specimen mass of 0.5 wt.% corresponding to the introduction of 4 hydrogen atoms per one molecule C_{60} (section BSC (27 min.) of Fig. 6(a));
4. the break in the point S indicated that interaction changes its character (Fig. 6(d, e));
5. the total process on section SC is more energy-intensive than on section BS (Fig. 6 (e));
6. the interaction rate on section SC is greater than on section BS (Fig. 6(d));
7. point C is the site where the interaction nature is radically changed.

3. RESULTS AND DISCUSSION

3.1. Lattice hydrogen

On examination of experimental data and theoretical calculations by molecular-kinetic theory, we have a good chance of interpretation of effect existing on experimental curves. Within the first three minutes the absorption process of hydrogen molecules has proceeded on the surface of fullerite powder and their diffusion is started into the volume of crystallites. In the course of absorption the hydrogen diffuses on octa- and tetrahedral interstitial sites.

In going from octa- to tetrahedral interstice the hydrogen molecule is subject to dissociation process (consuming energy in this case). On further moving into the fullerite volume hydrogen atoms arrive at octahedral interstices from tetrahedral, where they recombinate forming the molecule (releasing energy in this case). The dissociation and recombination processes runs sequentially up to the full occupation of octahedral interstitial sites and formation of molecular fcc sublattice of hydrogen (Fig. 7) occurs.

The activation energy of this process is combined from activation energy of elementary acts, making this sequence. As long as octahedral interstices exist, the quantity of dissociation events will be equal to the amount of recombination acts. As the process of filling of octahedral interstices of fcc sublattice of fullerite by hydrogen is completed, the both molecular sublattices will contain the equal quantity of molecules in the elementary cells. The formed solid interstitial solution can be written as follows:

$$C_{60} + H_2 = C_{60}H_2 \quad (1)$$

The section ‘BS’ on experimental curves corresponds to this process. The break of experimental curves is presented in the ‘S’ indicating that the hydrogen interaction with fullerite changes its character.

It can be assumed that further process of hydrogen absorption follows by the way of occupation of tetrahedral interstices by atomic hydrogen. (Fig. 6e, section SC). However in this case, the energy provision of dissociation would not be compensated by the subsequent exoeffects of recombination reactions. Because of this, the total energy consumption of this process will be more than at the earlier sections and it is defined only by the value of activation energy of the process of hydrogen molecules dissociation.

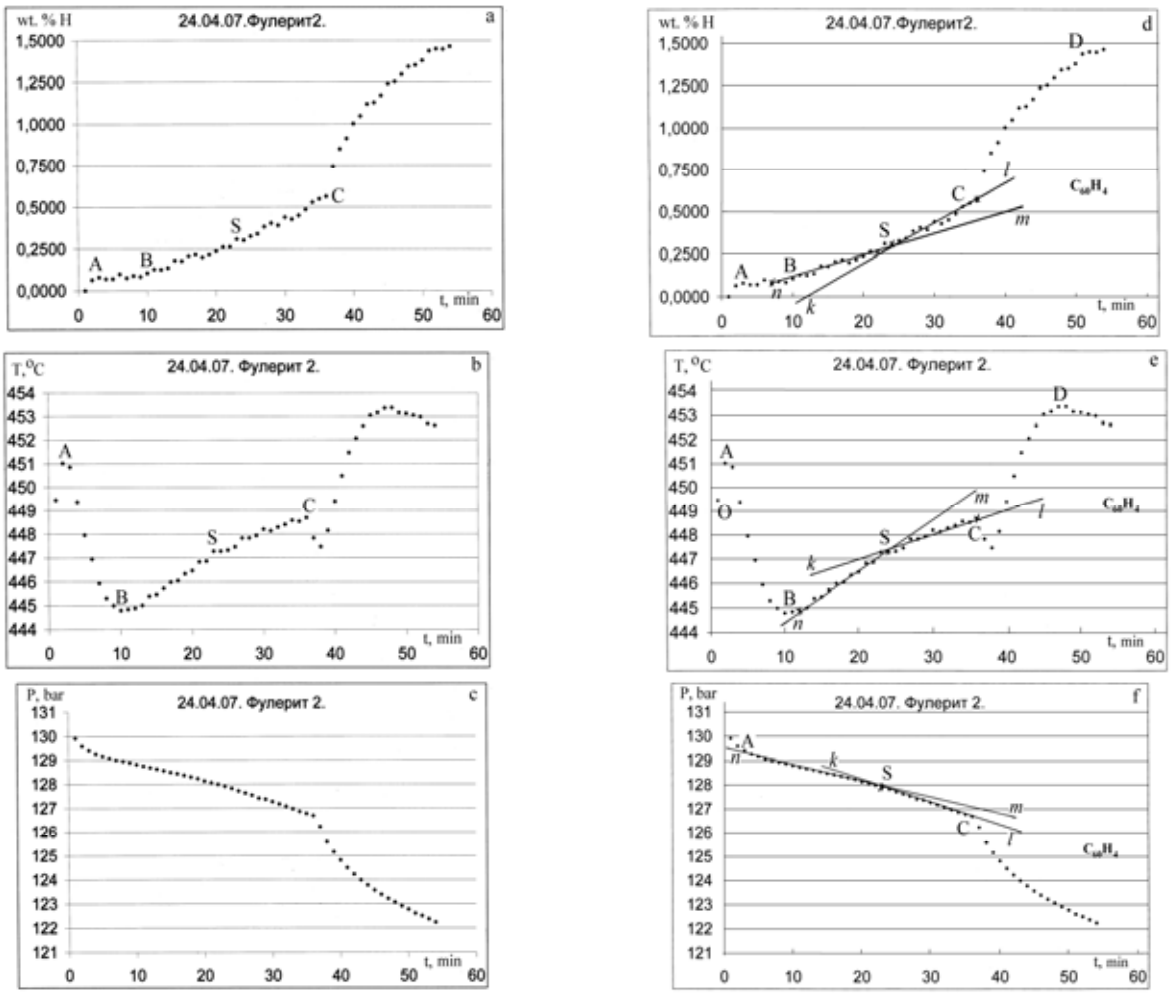

Fig. 6. Experimental plots on investigation of interaction processes between hydrogen and fullerite, presented the formation of hydrogen solid solution in fullerite: a, d) dependences of fullerite mass change with time; b, e) fullerite temperature modifications in time; c, f) hydrogen pressure changes in reactor. The neighbouring points of diagram curves are spaced out at equal intervals of 1 minute; (d, e, f) are supplemented by subsidiary straight lines 'nm' and 'kl'; Section BS – absorption of molecular hydrogen, Section SC – dissociative absorption of hydrogen.

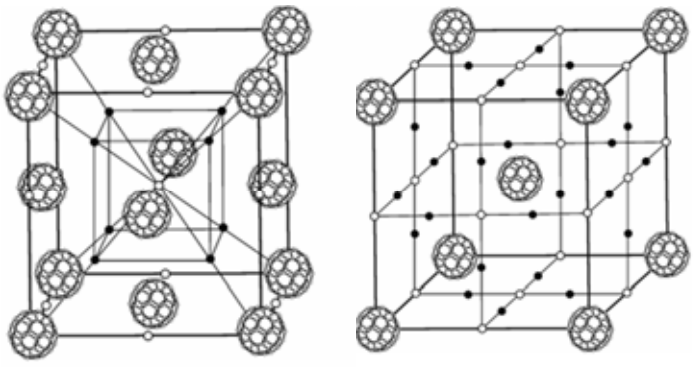

Fig. 7. Elementary cell of fullerite with fcc structure(o -octahedral (O) interstitial sites, in which molecules of hydrogen are located; ● - tetrahedral (T) interstitial sites, in which atoms of hydrogen are placed; - sites of crystalline lattice, in which fullerene molecules are distributed).

In the case of fully filling of tetrahedral interstitial sites, the hydrogen content in fullerite is doubled, because for every octahedral interstitial site there are two tetrahedral interstices. The formation of solid solution can be expressed by equation:

$$C_{60} + H_2 + 2H = C_{60}H_4 \quad (2)$$

The atomic-molecular sublattice of hydrogen contains three hydrogen particles (one molecule and two atoms) per one molecule of fullerene.

At this stage the process of physical absorption of hydrogen by fullerite is completed. This process of absorption is changed by desorption process and the overall process goes in the reverse direction with decreasing hydrogen pressure.

From the view-point of molecular-kinetic theory such mechanism of hydrogen absorption by fullerite is quite possible. As interacting atoms and molecules can be considers as rigid spheres, it can be noted that radiuses RO, RT of sphere entered into octa- and tetrahedral interstices are determined correspondingly by formulae:

$$R_O = 0.41\ r;\ R_T = 0{,}22\ r,$$

where r is the radius of sphere, located in the sites of elementary cell (in the case of fullerene C_{60} r=0,35 nm).

For fullerite we have:

$$R_O = 0.41 \times 0.35\ \text{nm} = 0.1435\ \text{nm};$$

$$R_T = 0.22 \times 0.35\ \text{nm} = 0.077\ \text{nm}.$$

The volumes of these interstices are equal to:

$$V_O = 12.37\ Å^3;\ V_T = 1.91\ Å^3$$

with diameters and volumes of hydrogen molecule and atom taken as

$$D_{H_2} = 0.212\ \text{nm}\ \ V_{H_2} = 4.99\ Å^3,$$

$$D_H = 0.092\ \text{nm};\ V_H = 0.523\ Å^3,$$

it is necessary to point out that hydrogen molecule is freely placed in octahedral interstices and hydrogen atom – in tetrahedral interstices.

Hence, it should be mentioned that in the course of fullerite lattice saturation by hydrogen the following processes of physisorbing hydrogen formation are proceeded (Fig. 6, a, d): 1. OA – adsorption of H_2 on the surface of crystals; 2. AS – absorption of H_2; 3. SC – dissociative absorption of hydrogen; 4. AC – two stage absorption of hydrogen by fullerite lattice; and 5. CK – chemisorption of hydrogen by fullerene molecule.

3.2. Fullerinated hydrogen

The performed experiments have shown that after pressure release the absorbed hydrogen by fullerite is desorbed gradually at normal conditions. Such mobility of hydrogen can signify that the process of hydrogen chemisorption by all molecules of fullerene C60 will undergo evenly with the formation of molecules of equal energy or only fullerene molecules with the equal quantity of hydrogen atoms over all lattice volume. In this case topochemistry of reaction of fullerite interaction with hydrogen corresponds to the volume formation of hydride.

The sets of experiments have been pursued for the purpose of elucidation of topological model of hydrogen interaction with fullerite. The method of express-analysis of definition of fullerene molecules C_{60} presence in the solution developed by authors has been used in the experiments. This method has been described in the paper [24]. The experiments have demonstrated that topochemistry of process of hydrogen chemisorption by fullerene molecule in fullerite up to concentration of $C_{60}H_{36}$ follows the topochemical model of the volume formation of product and after this note the model of compressive shell is operating (Fig. 8).

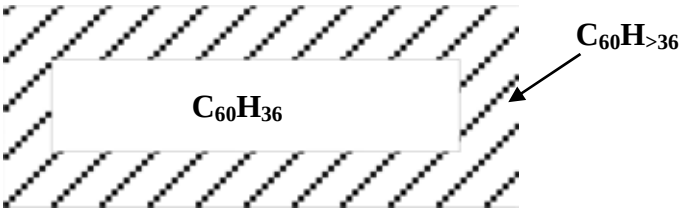

FIG. 8. The topochemical model of compressive shell typical for hydrogenation of fullerite more than concentration $C_{60}H_{36}$.

Analyzing experimental data on chemisorption of hydrogen, it should be emphasized that this process also runs in two stages. The uniform hydrogenation of fullerene molecules over the fullerite volume up to 36-40 atoms of hydrogen is related to the first stage. The second stage on the kinetic curves is expressed by the parabolic dependence. This testifies that the process has diffusive-limitative character (Fig. 4, Fig. 5).

The succession of experiments has been carried out to study the first stage of chemisorption and their findings are given in this work (specimens №9 and №10 – Fig. 5; №12 and №13 – Fig. 8 and №14 – Fig. 1-4). The results of experimental data shown in these figures have been accumulated in the Table 1.

The results analysis has shown that the value of temperature range of chemisorption stage I ($\Delta T = TI - TII$) does not depend on the rate of temperature raise and corresponds to the range near 115-125°C, whereas the change of this temperature range may last from 60 to 2000 minutes. However, it should be mentioned that the rise of temperature rate (υH) considerably affects the initiation of interaction with its shift into the more high-temperature field (see TI in Table 1). At the low rates of heating the reaction proceeds more completely (Δm).

TABLE 1. THE SUMMARY TABLE OF EXPERIMENTAL AND DESIGN DATA OBTAINED IN STUDIES OF CHEMISORPTION STAGE I OF HYDROGEN BY FULLERITE.

№ Experiment	υH, °C/min. The rate of specimen heating	TI (°C) Temperature of chemisorption initial stage I	TII (°C) Temperature of chemisorption initial stage II	ΔT(°C) Temperature range of realization of chemisorption stage I (TI – TII)	Δm (wt. %) Mass change in the course of chemisorption stage I	tI (min.) Duration of chemisorption stage I	$\upsilon^{t}_{\Delta m}$ (wt.%/min.) Average rate of mass change in time $(\frac{\Delta m}{t_I})$	$\upsilon^{T}_{\Delta m}$ (wt.%/ °C) Specific mass of chemisorbed hydrogen with temperature rise of one degree 1°C $(\frac{\Delta m}{\Delta T})$
12	0.061	314	436	122	5.9	2000	0.0030	0.048
14	0.125	340	460	120	5.8	1100	0.0052	0.048
13	0.139	346	465	119	5.8	1000	0.0058	0.049
9	1.34	380	503	123	5.5	92	0.060	0.045
10	1.91	400	516	116	5.38	61	0.088	0.046

The change of average rate of fullerite mass in time ($\upsilon^{t}_{\Delta m}$) increases with increase in the rate of temperature rise. In this case the specific volume of absorbing hydrogen on 1°C of temperature increase remains constant for any rate of heating ($\upsilon^{t}_{\Delta m}$ = const). From the aforesaid and focusing attention on the behaviour of the last two parameters ($\upsilon^{t}_{\Delta m}$ and $\upsilon^{T}_{\Delta m}$), it might be assumed that hydrogenation of fullerene molecule is the energy-controlled process in which the system temperature determines the quantity of hydrogen atoms on the fullerene molecule shell. This conclusion has a vital importance for further investigation of fullerene-hydrogen system and specifically for its applied utilization. Thus, from the results obtained it may be concluded that hydrogen in fullerite lattice at T = 450◦C conserves its high mobility up to its total concentration 5.5 – 6.0 wt.% that correspond to > 40 hydrogen atoms chemisorbed by each molecule C_{60}. Thereafter the process of interaction is limited by diffusive processes.

Because on the second stage the interaction process between hydrogen and fullerite follows the model of compressive shell, the uniform distribution of hydrogen between all molecules of fullerenes is not to be expected in this case (i.e. the formation of molecules with equal amount of hydrogen atoms will not exist). The process of second stage of chemisorption in fullerite differs from the previous processes just by this.

(a)

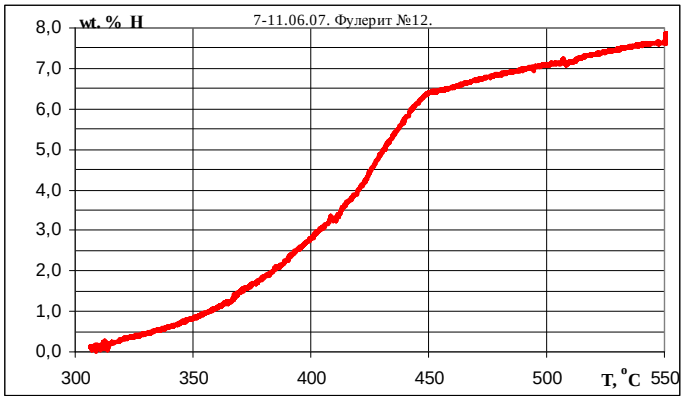

(b)

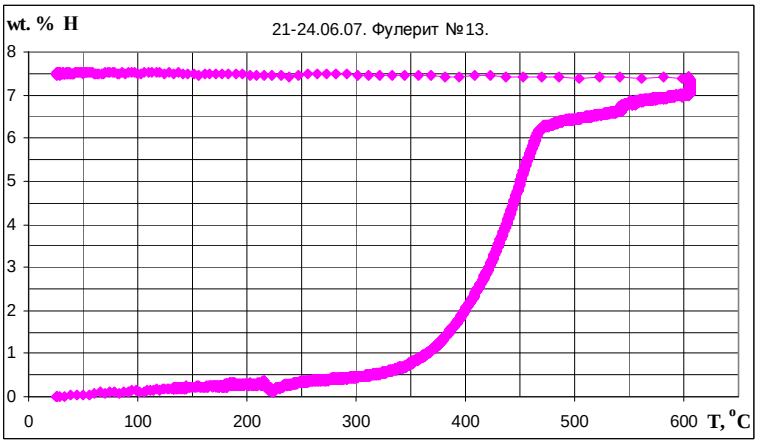

FIG. 9. The temperature dependence of mass change of fullerite specimen: (a) – specimen №12, (b) – specimen №13.

3.3. Model of gaseous hydrogen interaction with fullerite

Using the above discussion data, it can be proposed the model of processes occurred at the interaction between fullerite and hydrogen (Fig. 10). It is evident from this model that the interaction process involves several activated stages. The surface stage involves adsorption and hydrogen molecules transition from the adsorbed state to the absorbed one. The diffusive processes involve molecular diffusion, atomic diffusion and hydrogen atoms transfer through the layer of hydrogenated molecules of fullerene. They are controlled by the volume and grain boundaries diffusion. The hydride phase formation consists of the chain of elementary acts involving absorption of molecular hydrogen, dissociative absorption and chemisorption of hydrogen atoms by fullerene molecules.

The relative contribution of each stage to the interaction rate during the course of reaction has undergone a change. As this takes place, the limiting effect of the surface and diffusive processes on the reaction rate does not permit to study directly the process of interaction between fullerene molecule and hydrogen atom.

Taking into consideration the proposed model and experimental data obtained during hydrogenation of fullerite, it should be noted that in practice both components (lattice HL (Fig. 11) and fullerinated HF (Fig. 12) hydrogen) should be taken into account. The total content of hydrogen in fullerite (HTot) can reach the mass of 8.2 wt.% H, i.e.

$$H_{Tot} = H_L + H_F = H_4 + H_{60} = H_{64}, \text{ i.e. } 0.5 + 7.7 = 8.2 \text{ wt.\% H.} \qquad (3)$$

In the course of saturation process of fullerite by gaseous hydrogen the total content of hydrogen consists for all time from these two components (Table 2). After pressure release and specimen removal from reactor the lattice hydrogen is desorbed spontaneously from fullerite lattice at the normal conditions. Only chemisorbed hydrogen remains predominantly in fullerite. For this reason, in practice it is desirable to use the content of Table 2 for investigation of fullerite-hydrogen system.

TABLE 2. RELATION BETWEEN THE CONTENT OF LATTICE AND FULLERINATED HYDROGEN IN FULLERITE IN THE COURSE OF SATURATION PROCESS.

№	Total content HTot of hydrogen		Lattice hydrogen HL		Fullerinated hydrogen HF in compound C60Hx	
	wt.% H	atoms H/C_{60}	wt.% H	atoms H/C60	wt.% H	x
1	1.346	10	0.519	4	0.826	6
2	2.158	16	0.519	4	1.639	12
3	2.958	22	0.519	4	2.439	18
4	3.745	28	0.519	4	3.225	24
5	5.281	40	0.519	4	4.761	36
6	6.769	52	0.519	4	6.250	48
7	8.211	64	0.519	4	7.692	60

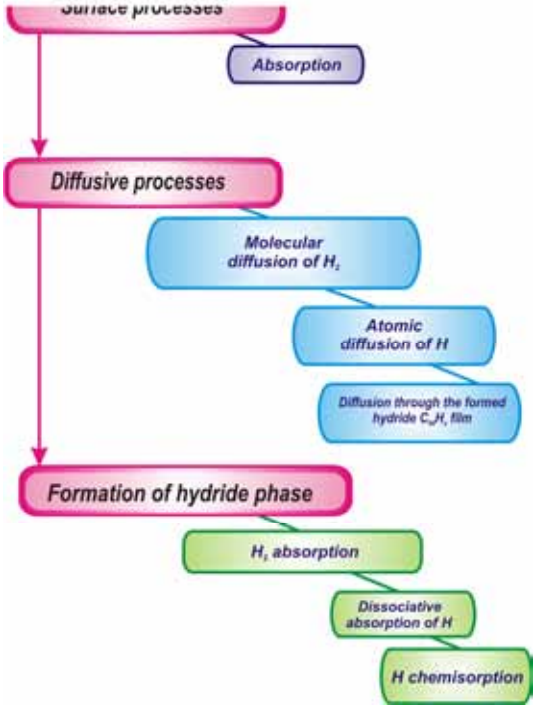

FIG. 10. Hypothetical model of processes at the gaseous hydrogen interaction with fullerite.

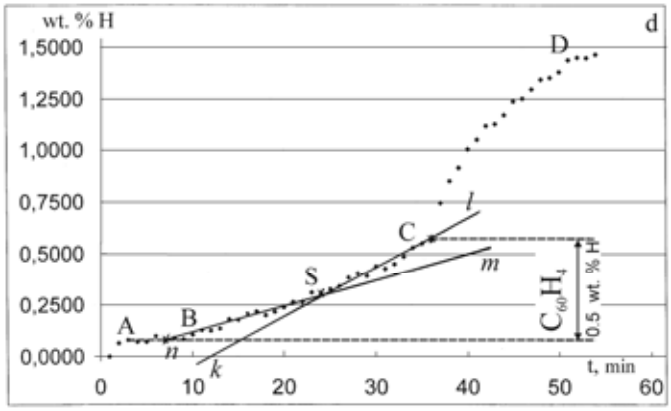

FIG. 11. The adsorption of H_2 and two stage atomic-molecular absorption of hydrogen in fcc lattice of fullerite. Arrowed line shows the content of lattice hydrogen (HL).

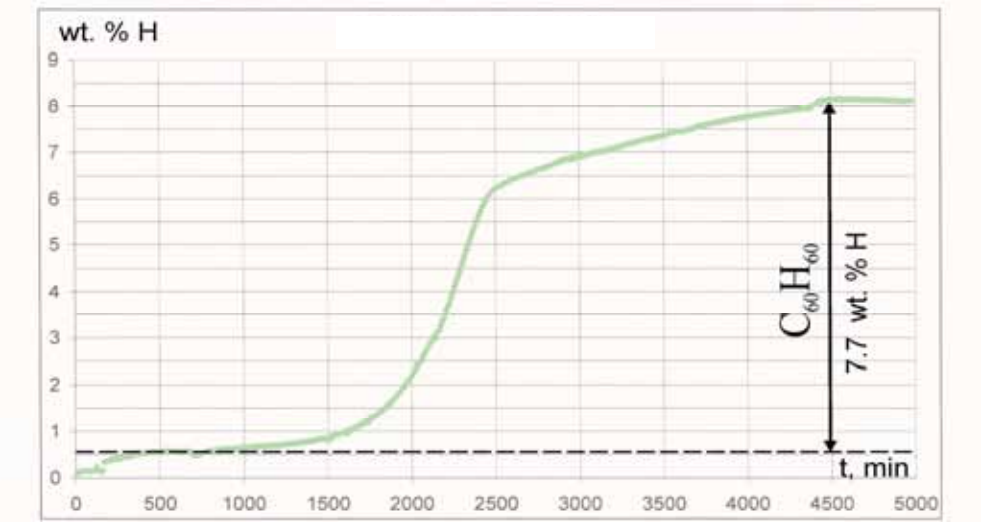

FIG. 12. Kinetics of interaction of gaseous hydrogen with fullerite. Arrowed line shows the fraction of fullerinated hydrogen (HF).

4. CONCLUSIONS

A series of tests were conducted to systematically investigate the fundamental property of fullerite C_{60} on hydrogen capacity.

The main results are summarized as follows:

1. Hydrofullerenes have been produced experimentally with the dissimilar content of hydrogen.
2. The optimum regime of C_{60} hydrogenation has been determined resulting in the full hydrogenation of fullerene molecule C_{60}.
3. The pressure P = 12 MPa and temperature T = 425 ÷ 455^{o}C are the optimal conditions of the performance of process of fullerite C_{60} hydrogenation.
4. As our experimental study has revealed, the induced period, caused by dissociative adsorption of molecular hydrogen, is absent at the interaction between molecular hydrogen and fullerite.
5. The sequence of formation of hydrogenated fullerene molecule $C_{60}H_{60}$ in the fullerite lattice has been going in the following order: the molecular hydrogen dissolution in octahedral interstices of fcc lattice of fullerite, the dissociation of hydrogen molecules in going from octa- to tetrahedral interstices, the interaction of hydrogen atoms with fullerene molecule.
6. It has been demonstrated that hydrogenation of fullerene molecule is the energy-controlled process in which the system temperature determines the quantity of hydrogen atoms on the shell of fullerene molecule especially for its applied use. The chemisorption process of hydrogen by molecule C_{60} is limited by diffusive processes in fullerite after hydrogen concentration conformed to > $C_{60}H_{36}$.
7. The results of our investigation into the application of developed method of spectral analysis have shown that the second stage of process of chemisorption follows the compressive shell model.
8. The model of processes going on at the interaction between H_2 and fullerite C_{60} has been proposed.
9. The mechanism for the definition of hydrogenation degree of molecule C_{60} in fullerite lattice has been suggested in the present paper.

ACKNOWLEDGEMENTS

This work was financially supported by International Atomic Energy Agency (contract № 15895/RO).

REFERENCES

[1] SCHUR, D.V., et al., Carbon **41** (2003) 1331-1342.
[2] JIN, C., et al., J. Phys. Chem. **98** (1994) 4215-4217.
[3] LOBACH, A.S., et al., Izv. RAN., Ser. khim. (1996) 483-484.
[4] SHIGEMATSU, K., ABE, K., MITANI, M., TANAKA, K., **7** (1992) 37-40.
[5] ATTALLA, M.I., VASSALLO, A.M., TATTAM, B.N., HANNA, J.V., J. Phys. Chem. **97** (1993) 6329-6331.
[6] HAUFLER, L.E., et. al., J. Phys. Chem. **94** (24) (1990) 8634-8636.
[7] HENDERSON, C.C., CAHILL, P.A., Science **259** (1993) 1885-1887.
[8] BASHKIN, I.O., et. al., Mol. Mat. **13**(1-4) (2000) 251-256.
[9] GERST, M. BECKHAUS, H.-D. RUCHARDT, C. CAMPBELL, E.E.B. TELLGMANN, R., Tetrahedron Lett. 34 (1993) 7729-7732.
[10] DARWISH, A.D.M. TAYLOR, R. LOUTFY, R., Proc. of 197th Meeting of Electrochemical Society, Toronto, (2000) Abstract 693.
[11] NOZU, R., MATSUMOTO, O., J. Electrochem. Soc. **143** (1996) 1919.
[12] TARASOV, B.P., FOKIN, V.N., MORAVSKY, A.P., SHUL'GA, YU.M., Izv. RAN., Ser. khim. **4** (1997) 679-683 (in Russian).
[13] TARASOV, B.P., FOKIN, V.N., MORAVSKY, A.P., SHUL'GA, YU.M., YARTYS', V.A., J. Alloys and Comp. **25** (1997) 253-254.
[14] TARASOV, B.P., Zhurn obshchei khimii **68** (1998) 1245-1248 (in Russian).
[15] TARASOV, B.P., et al., Proceedings of 12th World Hydrogen Energy Conference, Buenos Aires, Argentina **2** (1998) 1221-1230.
[16] GOLDSHLEGER, N.F., et al., Izv. RAN, Ser. khim. **5** (1999) 999-1002 (in Russian).
[17] GOLDSHLEGER, N.F., et al., Fullerenes, Recent Advances in the Chemistry and Physics of Fullerenes and Related Materials, Vol. 7, Pennington, NJ: The Electrochemical Society, 1999 pp. 647.
[18] MATYSINA, Z.A., SCHUR, D.V., Alloys and Fullerites, Nauka i obrazovanie, Dnepropetrovsk, 2002 (in Russian).
[19] SCHUR, D.V., ZAGINAICHENKO, S.YU., VEZIROGLU, T.N., Int. J. of Hydrogen Energy **33** (13) (2008) 3330-3345.
[20] BASHKIN, I.O., et. al., JETP Lett. **79** (5) (2004) 280.
[21] BASHKIN, I.O., et. al., Proc. of 8th International Conference "Hydrogen Materials Science and Chemistry of Carbon Nanomaterials", Sudak, Crimea, Ukraine, September 14-20 (2003) 796-799.
[22] BASHKIN, I.O., et. al., Proc. of 10th International Conference "Hydrogen Materials Science and Chemistry of Carbon Nanomaterials", Sudak, Crimea, Ukraine, September 22-28 (2007) 686-689.
[23] SAVENKO, A.F., et al., Proc. of NATO ARW on HMSCCN, Sevastopol; 2005. Published by Springer, The Netherlands (2007) 365-382.
[24] SCHUR, D.V., MATYSINA, Z.A., ZAGINAICHENKO, S.YU, Carbon nanomaterials and phase transformations in these materials, Nauka i obrazovanie, Dnepropetrovsk (2007).

PRELIMINARY RESULTS OF THE DEGRADATION OF PLATINUM BASED CATALYST IN PEM FUEL CELLS USING PIXE*

M. GÜNTHER[a], M. DEBRAY[b], H. CORTI[a]
[a]Fuel Cell Group, Department of Physics of Condensed Matter
[b]Discret Nuclear Spectroscopy Group, Tandar Laboratory
Centro Atómico Constituyentes,Comisión Nacional de Energía Atómica (CNEA), Buenos Aires Argentina
hrcorti@cnea.gov.ar

Abstract. This work reports the first results obtained on the dissolution and reprecipitation of platinum nanoparticles in the catalyst-membrane boundary of the MEA of a PEM fuel cell after 700 hours of operation under open circuit conditions. The formation of a platinum line on the membrane side near the cathode will be monitored using the PIXE technique in the ion beam facility at Tandar. The MEA used in the experiment was a commercial one (E-TEK), having a Nafion membrane and nanoparticulated Pt catalyst (loading 40%) on both, anodic and cathodic sides. Details of the sample preparation, the operating fuel cell parameters and the cutting procedure of the MEA previous to the ion beam analysis are described. The spatial resolution of the technique is discussed, along with the importance of the results for modelling the catalyst degradation in PEM fuel cells.

1. INTRODUCTION

Widespread application of hydrogen PEM fuel cells for vehicle and stationary purposes faces two major challenges: cost and lifetime. Although adding more catalyst or using thicker membranes could increase durability, increasing durability without increasing cost or losing performance seems to be the best option. For this reason, efforts are devoted to study the factors that determine a PEM fuel cell's lifetime [1].

Different processes can reduce the life of a PEMFC: dissolution and sintering of platinum or platinum alloys nanoparticles, membrane degradation and carbon-support corrosion. Besides that, the operation conditions such as impurities in the fuel or oxidant streams, pressure and temperature, load transients and start-up/shutdown cycles could also affect the fuel cell's durability.

The aggressive combination of strong acid and oxidizing conditions, high temperature and electrochemical potentials and reactive intermediate products affects the metal catalysts, proton-conducting membrane, and graphite used as catalyst support, gas diffusion layer (GDL) and bipolar plates. Thus, the durability targets of >5.000 hours for automotive fuel cells and >40.000 hours for stationary fuel cells, proposed by U.S DOE [2] are far of been reached.

The lack of standard durability protocols is a consequence of unknown mechanism of the deterioration processes occurring in the fuel cell. Most of the studies related to the chemical and physical degradation mechanisms of PEMFC membranes are performed on Nafion [3], while there have been limited studies on alternative studies on other proton conductive membranes such as those based on poly-benzimidazole (PBI) or modified PBI polymers. On

* Work performed within the framework of the IAEA Research Contract No. 15717/R0 ¨Study of the Degradation Mechanisms of the Membrane-Electrode Assembly of PEM Fuel Cells Using Ion Beam Analysis¨, part of the Co-ordinated Project: Application of Nuclear Methods in Microstructural Characterization and Performance Testing of Materials for Hydrogen Fuel Cell and Storage Technologies.

the other hand, most of the studies on the electrocatalyst stability were conducted on Pt nanoparticles supported on carbon (Vulcan) and mainly at room temperature. Little attention has been paid, so far, to the mechanism of degradation of new cathodic catalysts for the oxygen reduction reaction (ORR) [4].

High resolution Micro-PIXE (MPIXE) is now a well established technique for trace elemental analysis offering non-destructive multi-elemental 2D distribution capability and low detection limits. It allows simultaneous detection of multiple elements, with high quantitative accuracy coupled with an analytical sensitivity down to few ppm in plastics foils materials. Micro-Rutherford backscattering spectrometry (MRBS) provides information on matrix composition and thickness of the foil. The combination of MPIXE and MRBS therefore allows quantitative measurements of elemental concentration. STIM (Scanning Transmission Ion Microscopy) can be used in order to obtain an area mass density image for identifying structures, which are invisible under an optical microscope.

At the best of our knowledge, these techniques have never been used to explore the mechanisms of redistribution of metallic catalysts in contact with carbon support and proton conducting membranes. The aim of this work is to elucidate the mechanisms of degradation of Pt and Pt/Ru as anodic catalysts for PEMFC as well as Pt, and Pt alloys with Pd, Sn, Co and other metals for cathodic catalysts.

In order to accomplish this purpose the high resolution PIXE technique for direct measurements of metal concentration at different distances from the catalyst-membrane and catalysts GDL interphases will be used. The method to be used is similar to that described previously [5].

2. METHODS

2.1 The MPIXE technique

Most of the ion beam analysis (IBA) work done worldwide has been made so far with proton (1–3 MeV) and alpha particle (1–5 MeV) beams, probably due to their availability (most of the laboratories have small machines).Although protons and alpha particles have larger ranges compared to other ions with the same energy per nucleon (MeV/AMU) and are easy to focus to micron or submicrometer dimensions, heavier ions (_Z_ _e" _3_) have other characteristics_that make them very interesting for IBA applications.

The first one is related to the inner-shell vacancy production (or equivalently the X ray production) cross section. This cross section varies with the square of the projectile charge and the relevant energy parameter is the energy per nucleon of the projectile. In this approximation a beam of ^{16}O at 50 MeV is equivalent to protons of 3 MeV but with a cross section 64 times larger. Thus, measurements performed with a beam of ^{16}O at 50 MeV require 64 less time or beam current compared to one performed using 3 MeV protons.

Another advantage of the ^{16}O beam as compared to protons is the bremsstrahlung production. For protons, this contribution to the continuous background will always be present. On the other hand, in this case the membrane matrix is mainly composed of light N=Z elements (with the exception of ^{19}F), and this contribution disappears for ^{12}C and ^{16}O ions beams. For these reasons the heavy ion PIXE technique has clear advantages compared to low energy protons.

All these advantages are preserved in MPIXE where the quantities of sample material used in the analysis are much smaller and consistently the detection limits are higher. Due to the

superiority demonstrated for heavy ion PIXE, high energy heavy ion MPIXE (and other techniques of IBA, micromachining, etc.) was implemented at the Tandar accelerator, being one of few laboratories in the world which works with this technique.

In the standard PIXE the samples will be analyzed with normal size (2x2 mm^2) beams, with the surface of the membrane almost normal to the beam direction.

With our 20 MV tandem is possible to achieve high beam energies and hence larger depth within the analysed material. The possibility of achieving more energetic particles is crucial for the analysis of materials that are inhomogeneous in depth over the known thickness using the so called 'differential PIXE' which enables to get information on target stratum by performing PIXE on the same spot with different beam energies. Concerning this, a large number of test measurements at different beam energies on the various used membranes are needed in order to check the best experimental analysis conditions. In the same context, different ions (from protons to ^{16}O) might be use exploiting the possibilities offered by our tandem accelerator.

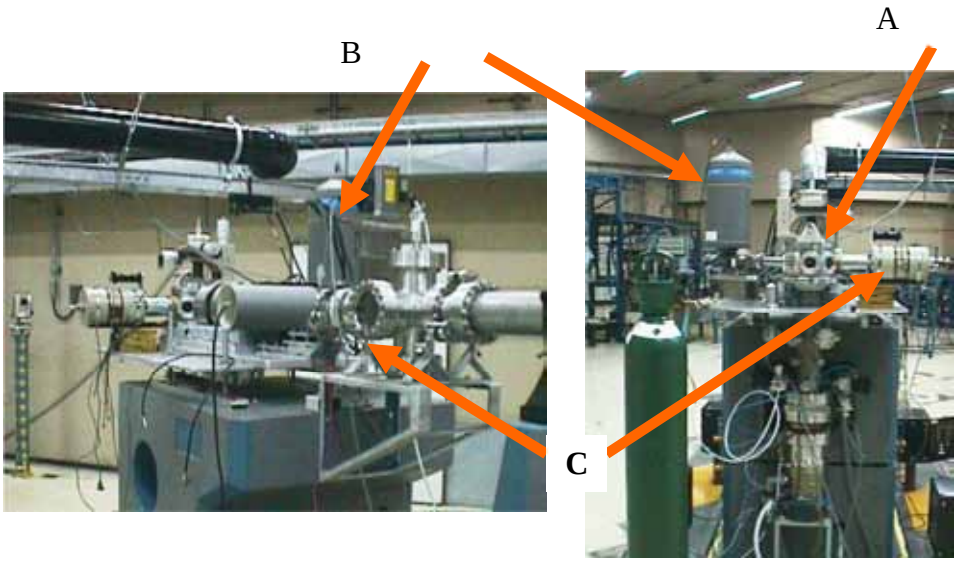

FIG. 1. View of the Tandar microbeam: irradiation chamber (A); detectors Si(Li) - 10 mm^2 (B), Si(Li) – 80 mm^2 (C).

Three techniques are currently being developed with the Tandar microbeam (Fig. 1) to address this problem. The first uses the transversal direct PIXE profile analysis of a cut membrane.

The second method is Rutherford Backscattering Spectrometry (RBS), for information on matrix composition and incident charge state. To detect back-scattered ions for RBS analysis an annular surface barrier detector is set on the beam axis. Scattering angle and counting rates can be controlled by changing the detector to sample distance.

The development of this technique comprises the optimization of the beam spot diameter, the analysis of thin-film depth profile standards at different energies to calibrate de methods and to determine optimum conditions, and finally, the quantitative analysis of the fuel cell MEAs.

2.2 Sample preparation and aging

During this period several MEAs are being prepared with membranes such as Nafion, PBI (polybenzimidazole) and ABPBI (modified polybezimidazole) obtained commercially or, as in the case of ABPBI, synthesized in our laboratory. However, the first PIXE assay is being performed with a commercial MEA (E-TEK) having a Nafion 117 membrane (thickness 170 μm) and Pt catalysts applied on the GDL and pressed on the membrane. The Pt loading on both side of the membrane was 0.5 $mg.cm^{-2}$.

A preliminary test of the MPIXE technique was performed using an E-TEK membrane having Pt on one side and Pt:Ru (atomic ratio 1:1) on the other side. This kind of catalyst is used in direct methanol fuel cell or in conventional hydrogen PEM fuel cells to improve the CO tolerance of the anode.

The MEA along with the GDL and the bipolar plates having channels to introduce the fuel (H_2) and the oxidant (air) were mounted on a monocell stack (Fig. 2). The temperature of the monocell was also controlled during the operation time using a PT100 thermoresistor.

The gases (H_2 and air) were humidified in order to control the water uptake of the membrane and their fluxes were maintained in 40 sccm for hydrogen and 100 sccm for air by using Alicat flow controllers. The complete setup for the MEAs aging process is shown in Fig. 3.

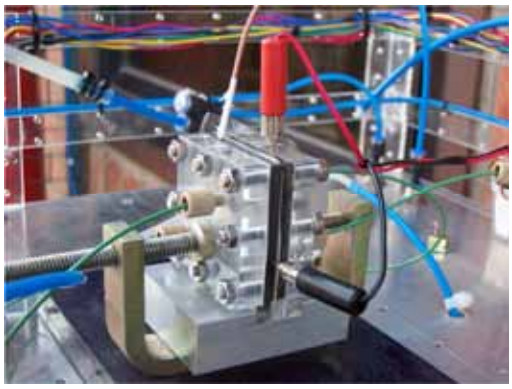

FIG. 2. View of the monocell with the gases input/outlet and the temperature sensor.

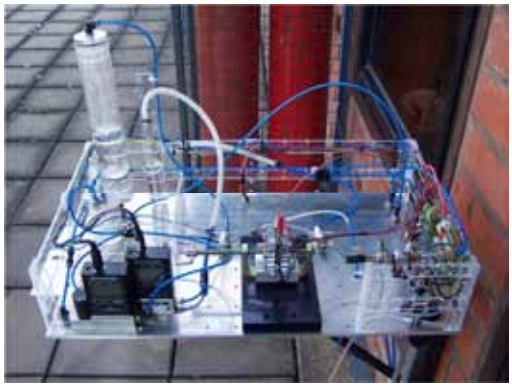

FIG. 3. View of the fuel monocell test station showing the humidifiers, flow controls and associated circuits.

The stack was maintained in open circuit condition to accelerate de dissolution and reprecipitation of Pt from the cathode side. Periodically the cell was connected to an Autolab PGSTAT112 in order to monitor the voltage vs. current curve time evolution.

Once the specified time of aging was reached, the MEA was removed and cut in pieces in order to prepare the sample for the IBA. One of the pieces was immersed in a plastic tube containing a liquid epoxy resin which is cured at moderate temperature. The imbibed membrane is cut in such a way that a transversal section of the membrane is exposed. Finally this side of the sample is polished with alumina.

3. RESULTS

3.1 Reference MEA.

The mechanism of Pt dissolution and reprecipitation within the membrane has been modelled using a thermodynamic and kinetic model that treats all the fundamental processes relevant for coarsening and mass loss in a MEA during normal operation of the fuel cell [8]. The model demonstrates the essential role of the particle size and hydrogen crossover on the degradation of the MEA.

The expected results of Pt degradation for a conventional MEA made with Nafion 117 and Pt nanoparticles supported on Vulcan XC-72 carbon are those reported by Zhang et al. [9], where a Pt band with thickness close to 1 μm or less is formed close to the cathode (several μm) after more than 1500 hours of OCV operation (that is, accelerated test) at 95 °C and 3 bar of pressure H_2/O_2.

In order to have a reference for our ageing tests and to probe that the PIXE technique with allows the characterization of Pt and bimetallic catalyst we performed an IBA with a ^{16}O beam on commercial (E-TEK) MEA with Pt and Pt:Ru (1:1) catalyst on each side of the membrane.

The results, shown in Figure 4, where the Pt side is up and the Pt:Ru side is down, indicate that the both membrane-catalyst layer are well defined. The larger thickness of the Pt:Ru layer is probably due to the tilt of the sample respect to the irradiation direction (a problem which can be avoided in future experiments) and to metal dragging during the cut of the sample

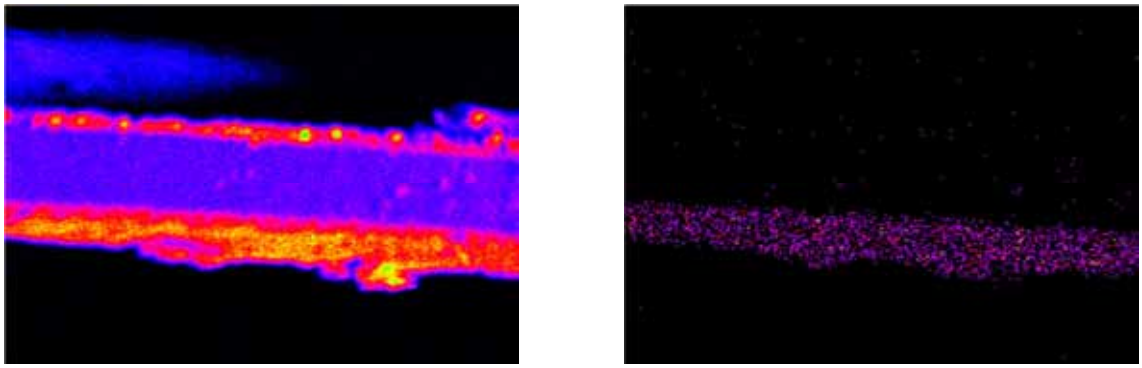

FIG. 4. 500 μm x 500 μm PIXE bidimentional images of the line Pt Lα (left) and the line Ru Kα. (right)

3.2 Aging sample

A commercial (E-TEK) MEA with Pt on both sides is being aged in the test facility described in Section 2.2. The test conditions are:

Temperature: ambient

Pressure (H_2/air) : 0.1 Mpa

Fluxes: 40 sccm for hydrogen and 100 sccm for air

In Fig. 5 it is shown the evolution of the OCV after 720 hours of aging. In average the cell voltage has decreased 10% from the initial value, which is a clear indication of MEA degradation.

In the next phase, MPIXE analysis will be completed. The results will be compared with that obtained by SEM analysis on the same MEA.

The MRBS technique will be also employed and compared to the MPIXE results. It is expected that MRBS could help us to determine the extension of the degradation in case the Pt band is well formed but its thickness is small enough to be determined by PIXE. On the other hand, if the Pt degradation does not result in the formation of a Pt-band, but small particles distributed in the membrane, MPIXE, would be the preferred technique due to its high sensitivity.

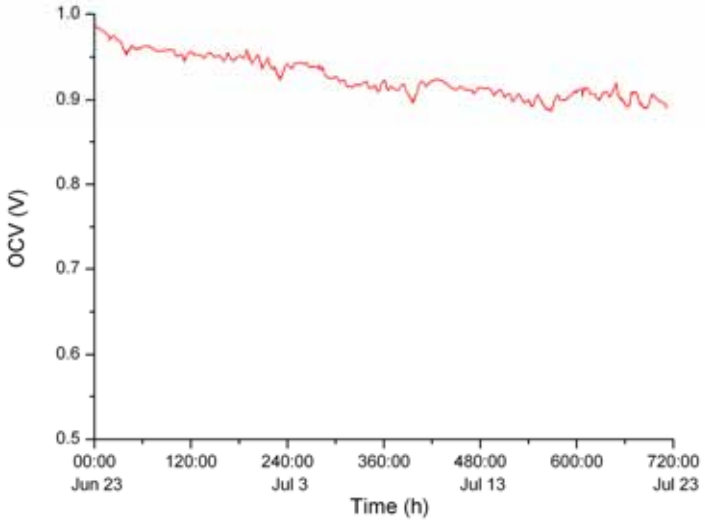

FIG. 5. Open circuit voltage of a commercial Pt/Nafion/Pt MEA as a function of time

ACKNOWLEDGMENTS

The authors thank financial support by IAEA (Research Contract No. 15717/R0) and ANPCyT (PICT 35403 and PAE 36985). HRC is member of the Carrera del Investigador de CONICET. MG thanks a fellowship from ANPCyT-CNEA.

REFERENCES

[1] BORUP, R. et al., Chem. Rev. **107** (2007) 3904.
[2] US DOE, http://www1.eere.energy.gov/hydrogenandfuelcells/mypp/, 2007.
[3] WU, J., et al., J. Power Sources **184** (2008) 104.
[4] ZHANG, S., et al., J. Power Sources **194** (2009) 588.

[5] STOLIAR, P, KREINER, A. J., DEBRAY, M. E., Appl. Rad. Isot. **61** (2004) 771.
[6] DEBRAY, M. E. et al., Nucl. Inst. and Meth. B **99** (1995) 384.
[7] OZAFRAN, M., et al., Nucl. Inst. and Meth. Phys. Res. B 201 (2003) 317.
[8] HOLBY, E. F., SHENG, W., SHAO-HORN, Y., MORGAN, Energy & Environm. **2** (2009) 865.
[9] ZHANG, J., LITTEER, B.A., GU, W., LIU, H., GASTEIGER, H.A., J. Electrochem. Soc. 154 (2007) B1006.

NEUTRON DIFFRACTION STUDY OF MODEL NiO/$LiCoO_2$ ELECTRODES FOR INNOVATIVE FUEL CELL DEVELOPMENT

R. COPPOLA[1], P.F. HENRY[2,4], A. MORENO[3], J. RODRIGUEZ-CARVAJAL[2], E. SIMONETTI[3]
[1] ENEA-Casaccia, FISNUC, CP 2400, 00100 Roma, Italy
[2] Institut Max von Laue – Paul Langevin, 6, rue Jules Horowitz, 38042 Grenoble, France
[3] ENEA-Casaccia, IDROCOMB, CP 2400, 00100 Rome, Italy
[4] Helmholtz Zentrum Berlin, Hahn-Meitner-Platz 1,, 14109, Berlin, Germany
roberto.coppola@enea.it

Abstract - This contribution presents the results of a neutron diffraction study carried out on Ni-NiO 30% electrodes coated with $LiMg_{0.05}Co_{0.95}O_2$ cobaltite deposited on the substrate by complex sol-gel process. The neutron diffraction measurements were carried out at the D20 diffractometer at the High Flux Reactor of the Institut Max von Laue – Paul Langevin. As the catalytic layer is only a few microns thick, the diffracting volume of the cobaltite phase was optimised by stacking 20 small rectangular pieces cut from the original electrode and assuming that the catalytic layer on the electrodes was homogenous. A pure cobaltite sample was used as a reference for identifying in the complete electrode the diffraction peaks of the catalytic layer. Both an as-received sample and an electrode tested 100 h at 650°C were measured. The results show that the adopted technique provides useful and accurate information on the crystallographic phases present the in the as-received electrode, while this structure is completely modified even after such a short exposure.

1. INTRODUCTION

Lithiated nickel oxide, $Li_xNi_{1-x}O$, is considered as one of the best suited materials for the development of innovative molten carbonate fuel cells (Fig. 1), mainly because of its fast oxygen reduction reaction rate.

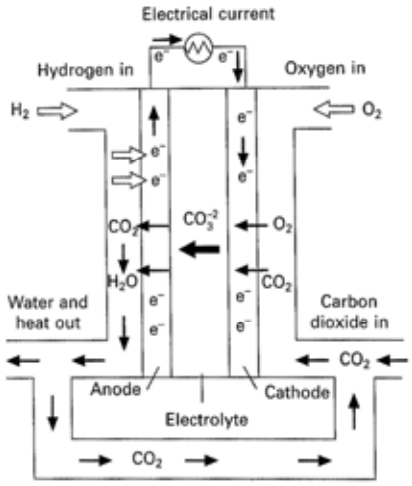

FIG. 1. Schematic of a molten carbonate fuel cell, where the electrolyte is a combination of alkali carbonates, water is produced at the anode side and CO_2 is required at the cathode side after Ref. (1).

However, its rate of dissolution in molten carbonate is high and consequently the cathodic nickel is dispersed and transported inside the electrolyte producing a concentration gradient under the electric field of the cell which results in a considerable decrease of the lifetime. One way to solve this problem is to cover the electrode with a thin layer of a material with a lower solubility in molten carbonates such as ferrites, manganites or cobaltites [1,2]. More specifically lithium cobaltite ($LiCoO_2$) is a semiconducting ceramic material, currently developed by many laboratories and commercially employed in lithium-ion batteries and in electrochromic films [2,3]. A process for the production of Mg doped cobaltite powders and

the preparation of porous cathodes of 100 cm^2 in size has been developed [3-8]. The porous nickel cathode has been covered with a thin layer of lithium cobaltite, doped with magnesium to maintain the properties of the metallic substrate, reducing nickel solubility. The complex sol-gel processing technique was selected because of its effectiveness in covering deeply and homogeneously the porous substrate. The morphology, crystallographic structure, conductivity and solubility of such electrodes have been investigated. In cell tests have been carried out obtaining encouraging results from the electrochemical point of view in comparison with nickel oxide [8]. Within this scientific frame, neutron diffraction has been utilized to characterize the crystallographic structure of the metallic substrate and of the catalytic layer, both in the as-received state and after exposure to simulated service conditions. It is in fact well known that neutron diffraction provides a powerful tool for such investigations, as is shown by review papers such as Ref.[9] and also by work carried out on solid state reaction synthesized $LiCoO_2$ material [10].

2. MATERIAL CHARACTERIZATION

The cathodes were prepared by means of a sol-gel process first adding LiOH to an aqueous acetate solution of Co^{2+} with ascorbic acid, then alkalizing with aqueous ammonia to pH=8 [11]. In these sols, diluted with ethanol, porous cathode plates have been dipped and withdrawn at a controlled rate several times to achieve the required film thickness. The coated substrate was soaked at 200°C for 72 h, then at 400°C for 1h and calcined (using a low heating and cooling rate of 1°C min^{-1}) at 650°C for 4 h. During heat treatments nickel plates were always placed between the ceramic sheets to avoid warping.. The formation of a $LiCoO_2$ crystalline phase on the porous nickel surface was verified by X ray diffraction [9]. The morphology of the cathode coated with $LiCoO_2$ was examined by field emission gun scanning electron microscopy (FEG-SEM) (Fig. 2).

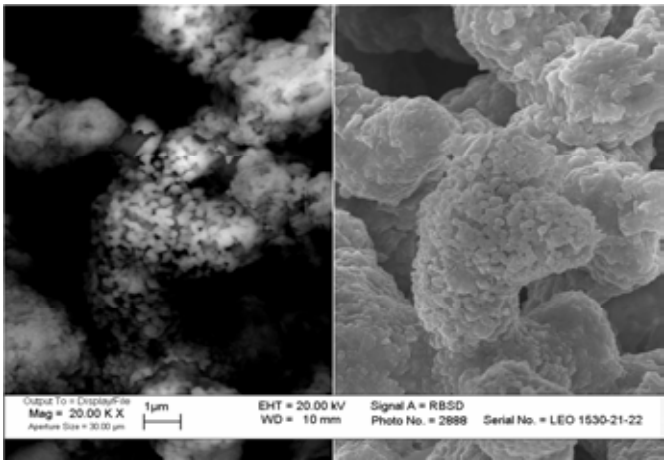

FIG. 2. FEG-SEM micrographs representing the microstructure of the nickel oxide covered with the lithium cobaltite electrode. Backscattering image is on the left, secondary electron image is on the right.

In cell tests showed a good cell performance that gradually improved during the cell operation time, with a voltage of 800 mV at a current density of 100 mA cm^{-2} after 700 h. The samples investigated in the neutron diffraction experiment were prepared in order to optimise the diffracting volume of the catalytic layer, which is only a few microns thick on each side of the Ni/NiO plate, which is itself approximately 0.5 mm thick. Therefore the original 10x10 cm^2

electrode was cut into 40 small rectangular pieces (~2x3cm^2 each), which were then stacked together to obtain a sufficient $LiCoO_2$ mass in the investigated volume. The composition of the electrode substrate is Ni/NiO 30%, while the catalytic layer is $LiCo_{0.95}Mg_{0.05}O_2$. Both an as-received electrode and an identical one tested at 650°C, 100 h were investigated. Reference samples were also prepared to separately characterize the crystallographic structure of the electrode (pure Ni and Ni/NiO 30%) and of the catalytic layer, for which tape cast $LiCo_{0.95}Mg_{0.05}O_2$ cobaltite was taken.

3. EXPERIMENTAL TECHNIQUE AND RESULTS

The neutron diffraction measurements were carried out at the D20 diffractometer at the High Flux Reactor of the Institut Max von Laue – Paul Langevin (ILL) [12] in the high-flux setting using both the highly ordered pyrolitic graphite and the Cu (200) monochromators in order to determine the optimal wavelength set-up, with all subsequent measurements done using the 1.3 Å wavelength. The incoming sample slits and α_2 collimation were also optimised to the sample geometry. This set-up of the instrument provided the best combination of flux and d-spacing range. The sample slit settings and collimation were also varied during these tests to obtain several similar sets of data to determine the optimal set-up. In the cases where the samples were in the form of strips, two different data collection geometries were used. The first one involved mounting the strips in bundles with the individual strips parallel to the incoming neutron beam and the second with the strips aligned perpendicular to the beam. This allowed the effects of preferred orientation of the deposited material to be probed. The differences observed in the patterns obtained as a result of preferred orientation do not substantially affect the refined Ni-NiO and cobaltite models. The data were refined using the ILL standard programs [13, 14].

Figure 3 shows the fit to the diffraction pattern for the Ni strips: although not immediately visible in the figure, there are several weak reflections that are not modelled. The positions of these reflections are at d-spacings of 4.058, 3.513, 2.485, 2.112, 1.613, 1.573, 1.437 and 1.354 Å. Ni is anti-ferromagnetically ordered at room temperature and all of the un-modelled peaks conform to the magnetic unit cell which is double that of the nuclear cell. The broadening of the peaks to higher angle in Fig. 3 is a result of the variation of the instrumental resolution function with 2θ.

Figure 4 shows the fit to the diffraction pattern for Ni-NiO 30% strips. Both NiO and Ni are modelled phases. Low angle reflections that are not attributed to the crystallographic structure of either Ni or NiO were observed which were attributed to the magnetic reflections originating from NiO and Ni, both of which are anti-ferromagnetically ordered at room temperature. Only the nuclear structures were modelled. The unit cell data for the two modelled phases are given in Table 1.

Figure 5 shows the diffraction pattern of the tape-cast cobaltite cathode material, $LiCo_{0.95}Mg_{0.05}O_2$: there is an impurity phase present in the pattern and a search of the possible impurities showed that MgO was a good fit for the residual unattributed peaks. The MgO estimated volume fraction was 0.0196, corresponding to 1.91 wt%, compared with the value of 0.65 wt% found in a previous study for the solid state reaction synthesized material with identical nominal composition [10]. There are also two low angle peaks that are not fitted to either phase but these were too weak to assign to any of the possible binary oxides. The details of the refined phases are given in table 2.

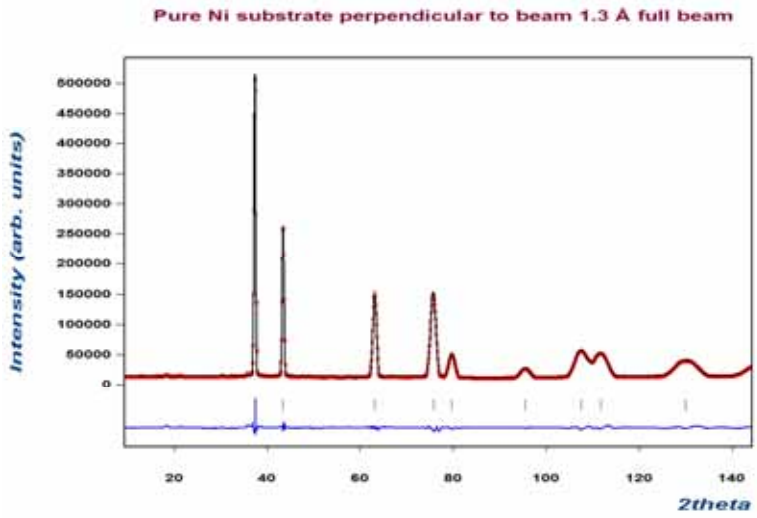

FIG. 3. Profile pattern (in red) of pure Ni substrate strips. The red solid line is the calculated pattern and the blue line is the difference plot. The green tick marks show the allowed reflections (Refined unit cell, a = 3.52695(32)Å, Space group Fm-3m).

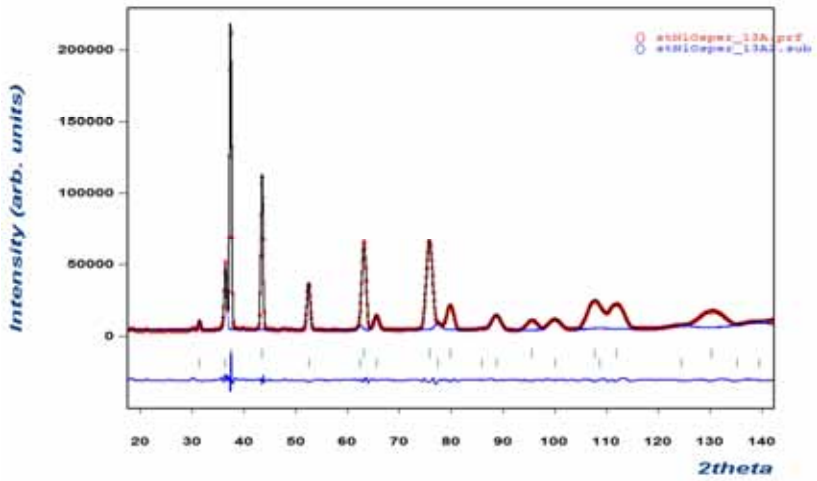

FIG. 4. Profile pattern (in red) of Ni- 30%NiO substrate strips. The red solid line is the calculated pattern and the blue line is the difference plot. The green tick marks show the allowed reflections of each modelled phase (see Table. I). The magnetic scattering is not taken into account.

TABLE 1. REFINED VALUES FOR THE UNIT CELL OF NiO (SPACE GROUP Fm-3m, a = 4.1789(5) Å)

Atom	X	Y	Z	Frac	Uiso x 100/ Å^2
Ni	0	0	0	1.0	0.59(5)
O	0.5	0.5	0.5	1.0	0.90(9)

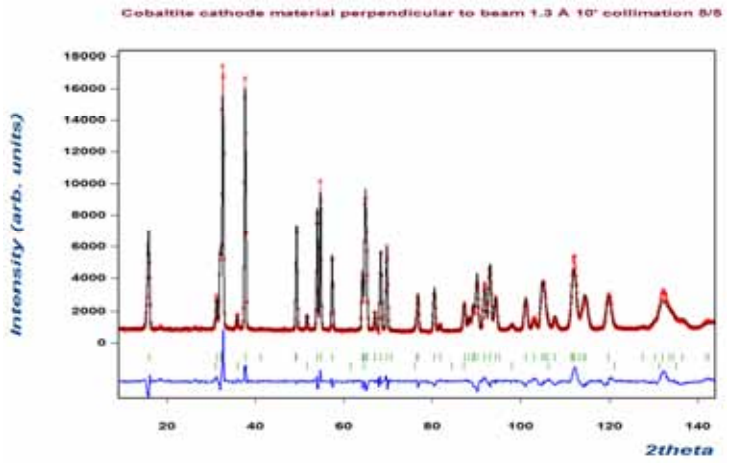

FIG. 5. Profile pattern of tape cast pure cobaltite cathode material referring to the following crystallographic phases: $LiMg_xCo_{1-x}O_2$ (x=0.05) R_{Bragg}= 9.07%, Rf = 5.18%, Vol: 99.117(4) Fract(%): 98.04 (1.17); MgO R_{Bragg}= 10.9%, Rf= 6.26%, Vol: 76.117(13) Fract(%): 1.96(0.13).

TABLE 2. REFINED VALUES FOR THE COBALTITE CATHODE MATERIAL MOUNTED PERPENDICULAR TO THE INCIDENT NEUTRON BEAM

Phase 1	$LiMg_xCo_{1-x}O_2$		Space group R -3 m (hexagonal setting)		
Lattice constants *a* = 2.84005(25) Å; *c* = 14.1783(8) Å; γ = 120 °					
Atom	X	Y	Z	Frac	Uiso x 100/ Å^2
Li	0	0	0.5	1.0	0.71
Mg	0	0	0	0.05*	0.06
Co	0	0	0	0.95*	0.06
O	0	0	0.26017(6)	1.0	0.25
Phase 2	MgO		Space group F m -3 m		
Lattice constant *a* = 4.2372(10) Å					
Atom	X	Y	Z	Frac	Uiso x 100/ Å^2
Mg	0.5	0.5	0.5	1.0	1.00
O	0	0	0	1.0	1.00

* fixed composition.
The atomic weight % of MgO was found to be approximately 1.91(8)%.

Figure 6 shows the diffraction pattern of the as-received electrode. If there were no cobaltite material deposited, the blue (cobaltite deposited strips) pattern should just be a combination of the green and pink. However, it is clear that there are extra reflections in the blue pattern. In Figure 7 the electrode is compared with the pattern measured for the reference materials depicted in Figs 4-6. The main peaks for $LiMg_xCo_{1-x}O_2$ correspond well to the weak reflections in the pattern of the deposited cobaltite strips that could not be assigned to either

Ni or NiO. A full analysis was not possible however with such weak reflections compared to the substrate.

The powder neutron diffraction pattern and resultant fit of the electrode after simulated service treatment are shown in Fig. 8. NiO is clearly present but the original cobaltite material is not, replaced by peaks that do not correspond to phases known to be present in the bulk samples. Further work using powder X ray diffraction is required to identify the phases present after treatment.

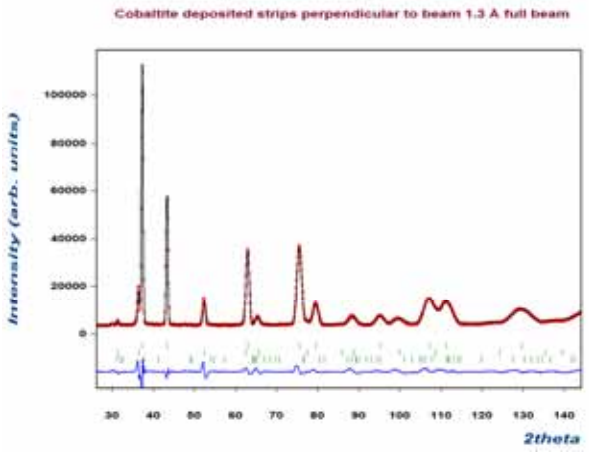

FIG. 6. Profile pattern (red) of the tested electrode referring to the following crystallographic phases : Ni R_{Bragg}= 3.49%, Rf = 1.55%, Vol: 44.049(3) Fract(%): 81.70(1.02); NiO R_{Bragg}= 5.79%, Rf = 2.79%, Vol: 72.635(0) Fract(%): 17.37(0.49); Rhombohedral $LiMg_xCo_{1-x}O_2$ R_{Bragg}= 30.2%, Rf = 16.6%, Vol: 99.033(0) Fract(%): (0.93(0.58).

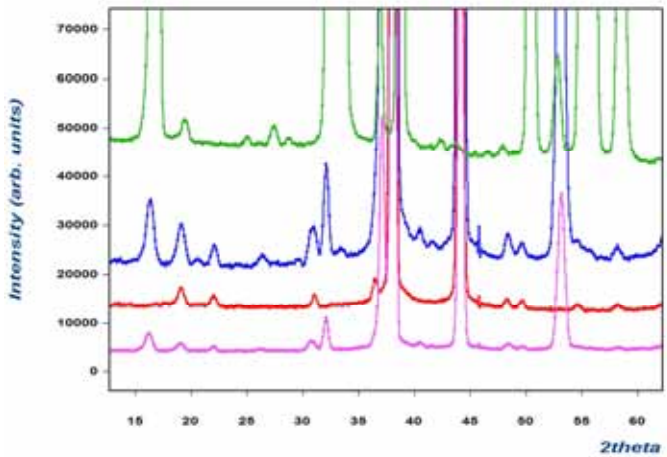

FIG. 7. Details of the profile patterns of the as-received electrode (in blue) compared to cobaltite (green, see Fig. 5), Ni-NiO30% substrate (pink, see Fig. 4) and Ni (red, see Fig. 3). The two main observable peaks for the rhombohedral cobaltite are at 33.4° and 38.8°.

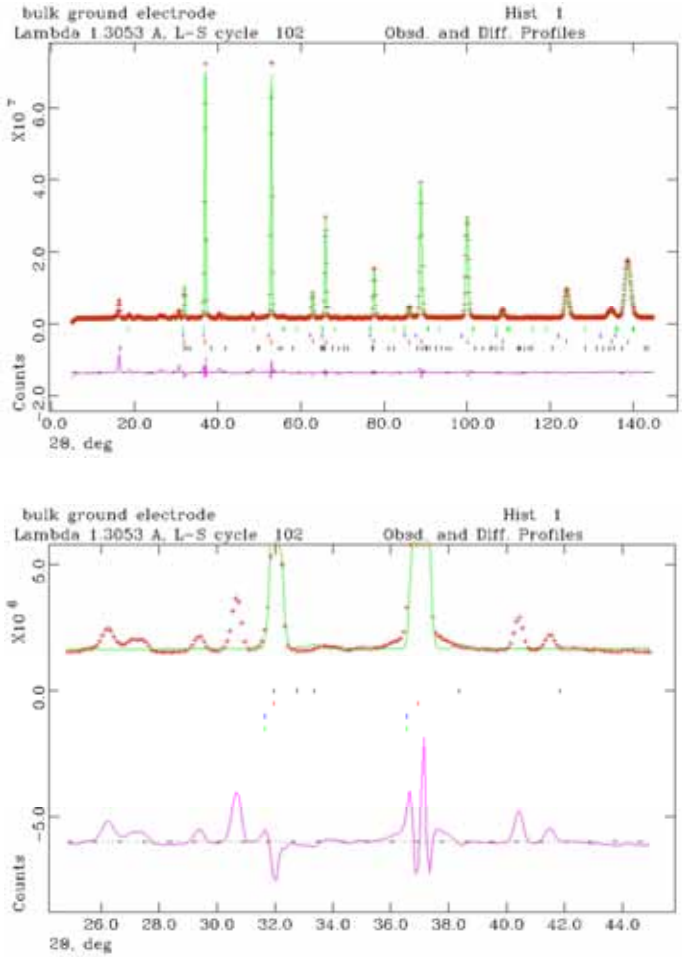

FIG. 8. Profile pattern of the electrode treated at 650°C (crosses) where the marked phases are as follows from top to bottom: $LiMg_xCo_{1-x}O_2$, nickel oxide, magnesium oxide and cobalt oxide (phase 4). The only significant phase present is nickel oxide. Highlighted area at low angle shows the peaks present for the unidentified phases.

4. CONCLUSIONS

Ni/NiO electrodes coated with a few micron thick layer of sol-gel deposited $LiCo_{0.95}Mg_{0.05}O_2$ have been successfully investigated by neutron diffraction exploiting the unique features of the D20 diffractometer and optimising the cobaltite diffracting volume by stacking several pieces of the original electrode. This experimental procedure can be of general interest for similar electrodes especially when they are constituted by elements, such as Li, not easily observable by X ray diffraction. Furthermore, in order to understand the chemical modifications occurring in service it is essential to non-destructively characterize the whole electrode; therefore reference samples are necessary both for the substrate and for the catalytic layer. In the present case, it is clear that refinable data can be obtained from the cathode materials in short timescale periods on D20, although the set-up has not been optimised. In the as-received electrode a cobaltite volume fraction of the order of 0.01 is estimated; after 100 h at 650°C the initial crystallographic structure is completely changed but traces of hexagonal phase are still detectable. The presence of at least one minor impurity phase in the cobaltite cathode materials must also be confirmed by external measurements, such as elemental analysis. It is also not possible at this stage to determine whether there is a measurable effect caused by the thickness of the deposited material onto the substrate strips. The experimental conditions can be optimised by suppressing texture effects and increasing

the cobaltite catalytic layer; high neutron flux is mandatory. Complementary X ray diffraction and EXAFS measurements should provide information on the phases present in the tested electrode and on its homogeneity.

REFERENCES

[1] "Materials for fuel cells" Edited by M. Gasik, Woodhead Publishing in Materials, Cap. 7 Mc Phail, SIMONETTI, E., MORENO, A.

[2] S. T. KUK, Y. S. SONG, K. KIM, Journal of Power Sources 83 (1999) 50-56.

[3] LUNDBLAD, A., Doctoral Thesis, University of Stockholm, (1996).

[4] CAREWSKA, M., PALLINI, F., SCACCIA, S., RTI/ERG/TEA/96(02).ENEA Technical Report

[5] GIORGI, L., et al., J. Power Sources, **49** (1994) 227 – 243.

[6] GIORGI, L., CAREWSKA, M., SCACCIA, S., SIMONETTI, E., ZARZANA, F., Denki Kagaku **6** (1996) 482.

[7] GIORGI, L., et al., in Electrochemical Technology of Molten Salts, eds. C.A.C. Sequeira, G.S. Picard, pp. 285-302, Trans Tech Publications, Switzerland, 1993.

[8] SIMONETTI, E., LO PRESTI, R., J. Power. Sources. **160** (2006) 816.

[9] CHABRE, Y., PANNETIER, J., Progr. Solid State Chem. **23** 1 (1995) 1.

[10] COPPOLA, R., BOURÉE, F., GIORGI, L., Physica B **276-278** (2000) 862.

[11] DEPTULA, A., LADA, W., J. New. Mat. Electrochem. Sys. **6** (2003) 33-37.

[12] HANSEN, T.C., HENRY, P.F., FISCHER, H.E., TORREGROSSA, J., CONVERT, P., Meas. Sci. Technol. **19** 3 (2008) 034001.

[13] RODRÍGUEZ-CARVAJAL, J., Recent Developments of the Program FULLPROF,Commission on Powder Diffraction (IUCr), Newsletter **26** (2001)12.

[14] LARSON, A.C., DREELE, R.B.V., 1994), Report LAUR 86-748. Los Alamos National Laboratory, New Mexico, USA.

ION BEAM-BASED MICROANALYSIS OF HYDROGEN IN PROTON CONDUCTING CERAMICS

P. BERGER[1], S. SORIEUL[1], J.P. GALLIEN[1], S. MIRO[1,2], M.H. BERGER[3], A. SAYIR[4]
[1] Laboratoire Pierre SÜE (CEA/CNRS), CEA/SACLAY 91191 Gif sur Yvette France
[2] DEN-DANS/DMN/SRMP, CEA/SACLAY 91191 Gif sur Yvette Cedex France
[3] Ecole des Mines de Paris, Centre P.M Fourt, BP 87 91003 Evry Cedex – France
[4] NASA GRC 21000 Brookpark Road Cleveland, 44135 OH – USA
pascal.berger@cea.fr

Abstract: The Protonic Ceramic Fuel Cell (PCFC) concept is based on the use of a ceramic electrolyte with hydrogen conduction properties. Designed for an intermediate working temperature (400-600°C), PCFC could overcome most of the drawbacks of existing systems (no noble metal catalysts and reduced thermal ageing). To study proton conductivity in these ceramics and the implication of local microstructural changes, Ion Beam Analysis (IBA) has unique capabilities of measuring local hydrogen concentrations at the micron scale. Inter- and intra-granular defects that can act as barriers for hydrogen diffusion can be identified.

1. STATE OF THE ART IN HIGH TEMPERATURE PROTONIC CONDUCTORS RESEARCH

1.1 Protonic Ceramic Fuel Cell concept

After decades of development of fuel cell technologies, covering a wide range of working temperatures from ambient to 1000°C, there is practically no mature cell working at intermediate temperature in the range 400-600°C. In principle, such a cell could overcome most of the drawbacks of existing systems.

For low temperatures, PEMFC (polymer electrolyte membrane fuel cell) are usually limited to a maximum operation temperature of 90°C to prevent rapid dehydration of the Nafion® electrolyte membranes. Above all, the need for expensive noble metal catalysts and, as a consequence, of purified fuels to prevent CO poisoning, is the major obstacle of their commercial expansion. On the high temperature side, SOFC (solid oxide fuel cell), based on ceramic electrolytes with oxide ion conduction, are efficient above 800°C, but encounter problems of rapid ageing of materials resulting in gradual performance degradation.

In spite of world R&D efforts to overcome these limits, a 'temperature gap' still exists. A concept of an intermediate temperature fuel cell (400-600°C) based on the use of a proton conducting ceramic electrolyte, with higher conductivity than oxide ion based devices in this temperature range has been proposed. Efforts towards producing a PCFC have focused on the use of perovskites.

1.2 Conduction in HTPC ceramics

Pioneering research in PCFCs has been conducted by Iwahara who first evidenced proton conductivity in $SrCeO_3$ [1]. Subsequently, a significant enhancement of conductivity in ABO_3 oxides was demonstrated by partially replacing tetravalent B cations by trivalent ones, inducing formation of vacancies in the oxygen sub-lattice, enabling applications for these ceramics in hydrogen devices such as fuel cells, sensors or steam electrolyzers [2-4]. Most efforts have been focused on cerates and zirconates, especially $BaCeO_3$ and $SrCeO_3$ doped with Y, Yb and Gd [5-12]. Protons can be introduced in the structure by a simple wet atmosphere treatment. This reaction is generally described as a water molecule surface dissociation both filling oxygen vacancies and producing interstitial hydrogen atoms according to the reactions (using Kröger-Vink formalism):

$$H_2O + V_o^{\cdot\cdot} \leftrightarrow O_o^{x} + 2H_i \quad (1)$$

$$H_2O + O_o^{x} + V_o^{\cdot\cdot} \leftrightarrow 2\,OH_o \quad (2)$$

The concentration of protonic charge carriers depends on the number of oxygen vacancies and thus on the dopant concentration which is set typically between 5 to 10%. Relative to undoped materials, the protonic conductivity can be enhanced by up to 4 orders of magnitude.

Hydrogen transport in ceramics is described as a Grotthuss-like process where protons, present in the form of hydroxyl groups, can rotate around oxygen atoms and jump to an adjacent site (hopping mechanism). Although a conduction mechanism based on hydroxyl mobility is sometimes invoked, most of the experimental evidence (such as $\sqrt{2}$ dependence of conductivity with deuterium [9-12]) supports that the proton is the charge carrier. An important point is that this jump is assisted by oxygen lattice vibrations which reduce activation energy for proton transfer. Best protonic conductivities have been observed in loosely packed structures which favor metal-oxygen vibrations in spite of larger O-O distances [7, 13]. Quantum Molecular Dynamics (QMD) simulations confirm this description of the proton transfer process and provide additional information on the influence of the bonding between oxygen anions and B-site cations [14, 15].

1.3 Limitations to the use of HTPC ceramics

As a consequence of their chemical properties, the best protonic conductors are also the most vulnerable to ageing. The mobility and uptake of hydrogen, in a wet atmosphere, increases with the basicity of the oxygen lattice which leads to a higher sensitivity of the perovskite phase to chemical decomposition into hydroxides, or carbonates in CO_2 containing environments [16-18]. The thermodynamic nature of this chemical instability has been the main issue with the development of PCFCs.

Research efforts have focused on finding a compromise between hydrogen uptake, mobility and resistance to decomposition. Zirconates such as yttrium doped barium zirconates (BZY) and related compounds have attracted most of the interest in recent years [16, 19-26]. Although their synthesis is now mastered, their effective protonic conductivity is controversial [16, 27-28].

When looking to the scientific literature concerning high temperature protonic conductors (HTPC), a general issue seems to be the lack of control of microstructure. Numerous studies report conduction properties of distinct compositions without referring to it. An insufficient understanding of the implication of microstructural changes from one sample to another on the proton conductivity may lead to misinterpretations. Inter- and intra-granular defects can act as barriers for hydrogen diffusion. It has been demonstrated that local variations of the structure and oxygen vacancy concentration directly affect proton diffusion [29-30]. Microstructure induced limitations in hydrogen transport are usually evidenced via impedance measurements [31]. To obtain further information, it is crucial to have a direct access to local concentrations of hydrogen species.

2. ION BEAM ANALYSIS IN HTPC RESEARCH

2.1 Principle and motivations to use ion beam analysis

Ion Beam Analysis exploits the interactions of energetic light ions (MeV) with solid matter. Comprehensive overviews of IBA techniques can be found in several books and review

papers [32-34]. Among all of the possibilities presented, quantitative analysis of light elements is one of the most attractive uses, especially for hydrogen and its isotopes.

Hydrogen analysis can be done mostly by elastic recoil detection (ERD) and nuclear reaction analysis (NRA). In principle, ERD consists of collecting recoiled hydrogen nuclei produced under bombardment by heavier projectiles, usually ^{4}He. In the case of a thick target, both bombardment and detection must be done at a grazing incidence, Fig. 1.

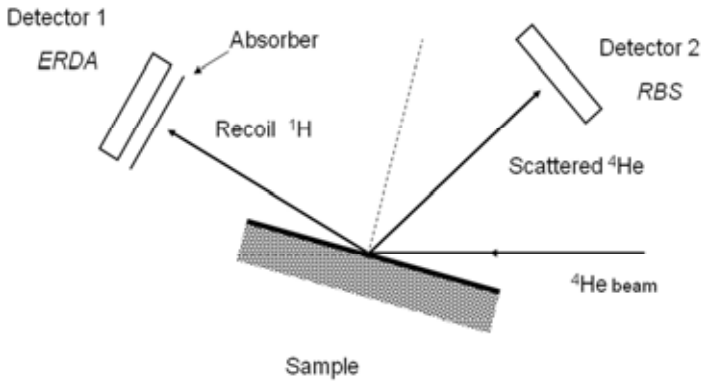

FIG. 1. Configuration of detectors for ERD experiments.

A thin absorber, typically a few microns thick aluminium foil, is placed before the particle detector to stop forward scattered ^{4}He projectiles. From the energy spectrum of recoiled protons, hydrogen depth concentration can be profiled up to a few 100 nm under the surface. Beyond its easy quantification, either from measurement of a standard or by means of a simulation code, the depth resolution of ERD enables contributions from both the bulk and surface to be distinguished. Accuracy is thus improved since deviations due to surface hydrolysis are not taken into account in the quantification process.

ERD is also suitable for deuterium analysis, but as spectra of mixtures of deuterium-hydrogen are sometimes difficult to deconvolute, NRA is often preferred. In these cases helium-3 induced nuclear reactions ^{2}H(^{3}He,p)^{4}He are used. As very energetic protons are emitted (greater than 10 MeV), the probed depth is much higher (a few microns), but to the detriment of depth resolution. NRA can also be used for hydrogen analysis with nitrogen-15 induced nuclear reaction: ^{1}H(^{15}N,αγ)^{12}C. Used in a resonant mode, especially with the 6.385 MeV resonance, this nuclear reaction is used to probe the near surface or interfacial hydrogen depth profiles.

2.2 Examples of the use of IBA

Other methods in use in the HTPC community for the determination of mass transport are Secondary Ion Mass Spectrometry (SIMS) [35-36] and RAMAN spectroscopy [37-39] with only MeV ion beam microanalysis techniques applied for studies of hydrogen transport. There are at least two motivations for using IBA, either to evidence unambiguously the presence of hydrogen or to quantify hydrogen gradients.

The first report of an extensive use of NRA goes back to the beginning of the 1990s [40]. Membranes of Yb doped $SrCeO_3$ were implanted with deuterium on one side and then annealed to investigate permeation through the ceramic disk. Whereas most experiments monitor the opposite side of the cell for possible atmospheric releases of D_2O or D_2 as a function of time and temperature, the nuclear reaction ^{2}H(^{3}He,p)^{4}He was used in this case to directly determine the diffusion of deuterium across the ceramic. In order to increase the

sensitivity of deuterium detection, the same concept was subsequently applied, associating with the membrane a hydrogen getter (e.g. Zr) on the exit side to concentrate deuterium. Deuterium was quantified in the getter using ERD [41-42]. The coupling of implantation and ERD analysis have often been considered as the most efficient approach to the study of hydrogen loading properties of HTPCs [43-44]. As an extension of plasma-material interaction research, conducted in the fusion community, studies of the kinetics and mechanisms of hydrogen-deuterium exchange of HTPC surfaces have made use of ERD. Both intrinsic properties [45-47] or ionic bombardment induced modifications [44, 48-49] have been investigated. The most striking finding has been a huge hydrogen-deuterium isotope effect which suggests a significant role of surface dissociation of water molecules in the hydrogen uptake process of HTPCs [50].

Since the understanding of mechanisms of hydrogen transport in HTPC has to be considered in a multi scale approach, long distance transport and influence of extended defects must also be studied. Impedance measurements enable determination of the respective contributions of bulk and grain boundaries to overall conductivity of the ceramic [30, 31, 51, 52]. Information on hydrogen transport relevant for the improvement of microstructure requires local methods for direct hydrogen concentration measurements [30]. Nuclear microanalysis, especially ERD, meets this demand when the beam size is reduced to the micron size. Measurement of long distance hydrogen concentration gradients gives a true insight into transport mechanisms since various diffusion and transport models can be directly assessed. An easy method consists of achieving incomplete hydrogen loading, either by exposing a dried ceramic to a wet atmosphere or unloading a fully hydrated one under vacuum or dry atmosphere, followed by ERD profiling of a cross section of the sample. Figure 2 shows an example of hydrogen profiles measured by ERD on cross-sections of $BaCe_{0.9}Y_{0.1}O_{3-\delta}$ perovskites [53]. Once again, ERD holds concurrently quantification and accuracy thanks to the weak sensitivity towards surface hydrolysis. As expected, the shape of the hydrogen concentration profiles is always a combination of a central plateau and near surface concentration gradients. With the help of a simple Fickian model, formal hydrogen diffusion coefficients can be deduced. Unexpectedly, the concentration of the plateau decreases rapidly with ageing which means that only a fraction of the hydrogen contained in these perovskites is strongly bonded, the remainder having a much greater mobility.

When an increase in sensitivity and probed depth is needed, Elastic Recoil Coincidence Spectroscopy (ERCS) can be used as a variant of ERD with a proton beam and a thin sample [54-58]. Each proton-proton collision leads to a simultaneous forward emission at 90° of the two protons, forward and scattered. By detecting them in coincidence, as seen in Fig. 3, hydrogen events can be distinguished from the large background of simple forward scattering events of heavier elements. The improvement of sensitivity comes from high cross-sections of scattering events at forward angles. The drawback of ERCS is that the quantification process is no longer straightforward because of multiple scattering effects.

ERCS has been applied with a micron size proton beam to study grain boundary hydrogen mobility in large grained melt-textured $BaCe_{0.9}Y_{0.1}O_{3-\delta}$ ceramics synthesized by laser assisted oriented growth [59]. Figure 4a shows a map of the microstructure obtained by scanning the microbeam in STIM mode (Scanning Transmission Ion Microscopy) which images lateral contrast in energy losses of the ions of the microbeam across the thin sample. Due to the presence of an intergranular secondary phase, black lines are an image of grain boundaries. Figure 4b presents the corresponding ERCS image which shows that hydrogen is mainly localized in grain boundaries. As envisioned from impedance measurements, grain boundaries trap hydrogen and lower their overall mobility. Since ERCS is depth resolved, microbeam ERCS has the potential to offer full 3D microcopy of fuel cell materials at the micron scale.

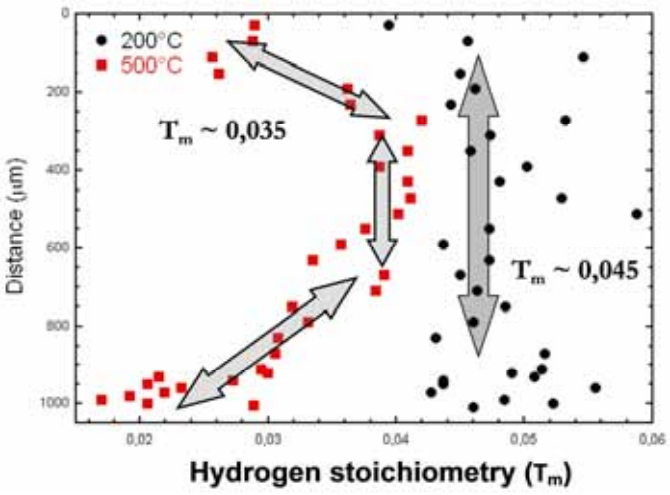

FIG. 2. Hydrogen concentration profiles measured by ERD on cross sections of vacuum annealed Y doped $BaCeO_3$ (from Ref. [53].

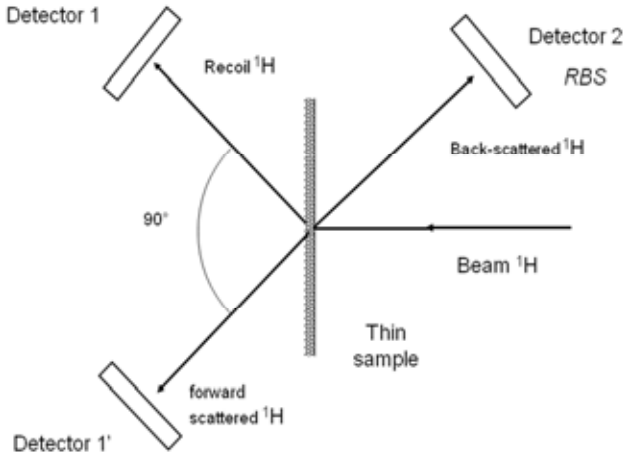

FIG. 3. Configuration of detectors for ERCS experiments.

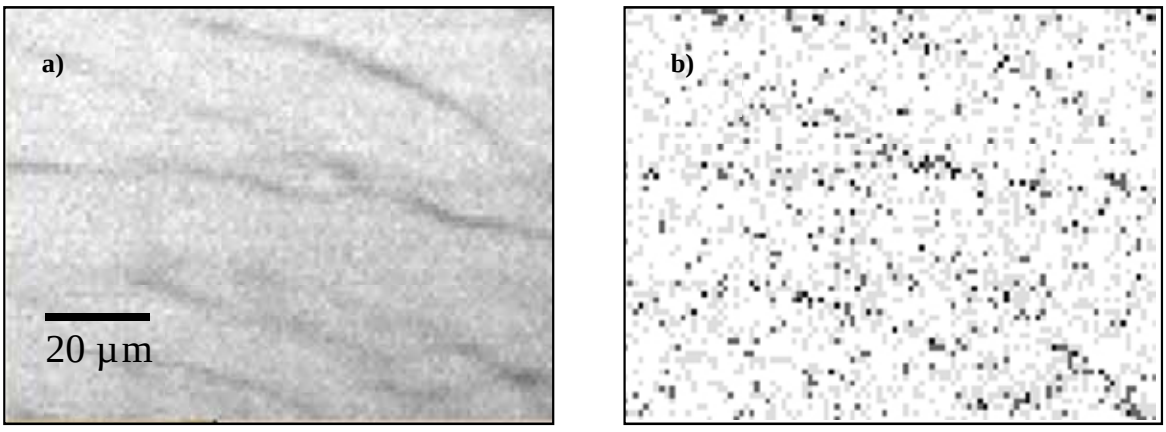

FIG. 4. a) Image in STIM mode of grain boundaries of a BaCeYO ceramic. b) Corresponding ERCS image of hydrogen concentration.

3. CONCLUSIONS

In materials science, quantitative, accurate hydrogen profiling is remains a significant challenge and ion beam microanalysis can be considered to potential solution. High temperature protonic conductors represent an ideal field of use. However, it is essential to consider that elucidating hydrogen transport mechanisms in HTPCs is a multi-scale problem from the nanometer to millimeter scale. The contribution of IBA is unique whilst also only a part of the whole understanding.

REFERENCES

[1] IWAHARA, H., ESAKA, T., UCHIDA, H., MAEDA, N., Solid State Ionics **3/4** (1981) 359.
[2] IWAHARA, H., UCHIDA, H., MAEDA, N., J. Power Sources **7** (1982) 293.
[3] UCHIDA, H., MAEDA, N., IWAHARA, H., Solid State Ionics **11** (1983) 117.
[4] IWAHARA, H., UCHIDA, H., TANAKA, S., Solid State Ionics **9/10** (1983) 1021.
[5] IWAHARA, H., UCHIDA, H., ONO, K., OGAKI, K., J. Electrochem. Soc. **135** (1988) 529
[6] LEE, W., NOWICK, A.S., Solid State Ionics **18/19** (1986) 989
[7] KREUER, K.D., Solid State Ionics **97** (1997) 1
[8] BONANOS, N., ELLIS, B., KNIGHT, K.S., MAHMOOD, M.N., Solid State Ionics **35** (1989) 179
[9] BONANOS, N., Solid State Ionics **53/56** (1992) 967.
[10] BONANOS, N., J. Phys. Chem. Solids **54** (1993) 867.
[11] IWAHARA, H., UCHIDA, H., MORIMOTO, K., J. Electrochem. Soc. **137** (1990) 462.
[12] SHIMA, D., HAILE, S.M., Solid State Ionics **97** (1997) 443.
[13] KREUER, K.D., FUCHS, A., MAIER, J., Solid State Ionics **77** (1995) 157.
[14] MUNCH, W., SEIFERT, G., KREUER, K.D., MAIER, J., Solid State Ionics **86/88** (1996) 647.
[15] MUNCH, W., SEIFERT, G., KREUER, K. D., MAIER, J., Solid State Ionics **97** (1997) 39.
[16] KREUER, K.D., Solid State Ionics **125** (1999) 285.
[17] SHIMADA, T., WEN, C., TANIGUCHI, N., J. Power Sources **131** (2004) 28.
[18] BONANOS, N., KNIGHT, K.S., ELLIS, B., Solid State Ionics **79** (1995) 161.
[19] KREUER, K.D., Ann. Rev. Mater. Res. **33** (2003) 333.
[20] YAMAZAKI, Y., BABILO, P., HAILE, S.M., Chem. Mater. **20** (2008) 6352.
[21] RICOTE, S., BONANOS, N., CABOCHE, G., Solid State Ionics **180** (2009) 990
[22] RYU, K.H., HAILE, S.M., Solid State Ionics **125** (1999) 355
[23] KATAHIRA, K., KOHCHI, Y., SHIMURA, T., IWAHARA, H., Solid State Ionics **138** (2000) 91.
[24] AZAD, A.K., IRVINE, J.T.S., Solid State Ionics **178** (2007) 635.
[25] ZUO, C., ZHA, S., LIU, M., HATANO, M., UCHIYAMA, M., Adv. Mater. **18** (2006) 3318
[26] KATAHIRA, K., KOHCHI, Y., SHIMURA, T., IWAHARA, H., Solid State Ionics **138** (2000) 91.
[27] SCHOBER, T., KRUG, F., SCHILLING, W., Solid State Ionics **97** (1997) 369.
[28] IWAHARA, H., Solid State Ionics **86–88** (1996) 9.
[29] BERGER, M.H., SAYIR, A., BERGER, P., J. Hydrogen Energy **31** (2006) 1103.
[30] BERGER, M.H., SAYIR, A., DYNYS, F., BERGER, P., Solid State Ionics **177** (2006) 2339.

[31] HAILE, S.M., STANEFF, G., RYU, K.H., J. Mater. Sci. **36** (2001) 1149.
[32] ALFASSI, Z.B., PEISACH, M., CRC Press Elemental analysis by particle accelerators Boca Raton FL (1991).
[33] TESSMER, J.R., NASTASI, M., Handbook of Modern Ion Beam Materials Analysis, MRS, Pittsburgh PA (1995).
[34] TROCELLIER, P., BERGER, P., Encyclopedia of Analytical Chemistry John Wiley & Sons (2009).
[35] ISHIGAKI, T., YAMAUCHI, S., Kishio, K., FUEKI, K., IWAHARA, H. Solid State Ionics. **21** (1986) 239.
[36] DE SOUZA, R.A., KILNER, J.A., JEYNES, C., Solid State Ionics **97** (1997) 409.
[37] GLERUP, M., POULSEN, F.W., BERG, R.W., Solid State Ionics **148** (2002) 83.
[38] HIBINO, T., MIZUTANI, K., YAJIMA, T., IWAHARA, H., Solid State Ionics **58** (1992) 85.
[39] SLODCYK, A., et al., J. Ram. Spectros. **40** (2009) 513.
[40] MATSUNAMI, N., YAJIMA, T., IWAHARA, H., Nucl. Inst. Meth. B **65** (1992) 278.
[41] ARAI , T., KUNIMATSU, A., TAKAHIRO, K., NAGATA, S., YAMAGUCHI, S., AKIYAMA, Y., SATA, N., ISHIGAME, M., Solid State Ionics **121** (1999) 263.
[42] HORIIKE, S., KUNIMATSU, A., TAKAHIRO, K., NAGATA, S., YAMAGUCHI, S.**,** J. Alloys and Comp. **293-295** (1999) 838.
[43] TSUCHIYA, B., SODA, K., YUHARA, J., MORITA, K., IWAHARA, H., Solid State Ionics **117** (1999) 311.
[44] TSUCHIYA, B., NAGATA, S., TOH, K., SHIKAMA, T., Nucl. Inst. Meth. B **242** (2006) 588.
[45] TSUCHIYA, B., MORITA, K., NAGATA, S, TOH, K., SHIKAMA, T., Nucl. Inst. Meth. B **257** (2007) 541.
[46] MORITA, K., et al.,. Solid State Ionics **179** (2008) 793.
[47] MORITA, K., SUZUKI, H., SODA, K., Nucl. Inst. Meth. B **206** (2003) 228.
[48] KIM, J.H., TSUCHIYA, B, NAGATA, S, SHIKAMA, T., Solid State Ionics **180** (2009) 271.
[49] SODA, K., IIZUKA, E., TSUCHIYA, B., MORITA, K., IWAHARA, H., J. Nucl. Sci. Technol. **39** (2002) 359.
[50] TSUCHIYA, B., IIZUKA, E., SODA, K., MORITA, K., IWAHARA, H., J. Nucl. Mater. **258-263** (1998) 555.
[51] REICHEL, U., ARONS, R.R., SHILLING, W., Solid State Ionics **86/88** (1996) 639.
[52] DE VRIES, K.J., Solid State Ionics **100** (1997) 193.
[53] SORIEUL, S., et al., Nucl. Inst. Meth. B **266** (2008) 1430.
[54] COHEN, B.L., FINK, C.L., DEGNAN, J.H., J. Appl. Phys. **43** (1972) 19.
[55] HOFSÄSS, H.C., PARIKH, N.R., SWANSON, M.L., CHU, W., Nucl. Inst. Meth. B **45** (1990) 151.
[56] DUJMIC, D., JACSIC, M., SOIC, N., TADIC, T., BOGDANOVIC, I., Nucl. Inst. Meth. B **111** (1996) 126.
[57] FURUNO, K., et al., Nucl. Inst. Meth.B **210** (2003) 459.
[58] REICHART, P., DATZMANN, G., HAUPTNER, A., Hertenberger, R., Wild. C., Dollinger, G., Science **306** (2004) 1537.
[59] BERGER, P, et al., Solid State Ionics **177** (2006) 1655.

INFLUENCE OF REACTOR IRRADIATION ON STRUCTURE AND PROPERTIES OF HIGH TEMPERATURE PROTON CONDUCTORS

I.V. KHROMUSHIN, K. KADYRZHANOV, ZH. ZHOTABAEV, T. AKSENOVA, K. MUNASBAEVA
Institute of Nuclear Physics, National Nuclear Centre of the Republic of Kazakhstan, Kazakhstan
khromushin@mail.ru

Abstract: Influence of reactor irradiation on the structure and properties of high temperature proton conductors was studied. It was shown that oxide irradiation at 100^{o}C results in additional intercalation of oxygen, water and carbon dioxide molecules in the oxides. Further, reactor irradiation of barium and strontium cerates at 620^{o}C in contrast to low temperature irradiation results in both quantitative and qualitative changes in these oxides. Phase transformation in the oxide irradiated at 620^{o}C was observed to be a result of sample heating after irradiation.

1. INTRODUCTION

Complex oxides with the perovskite structure are very interesting both from the scientific and applied points of view because of their unique properties such as high temperature protonic conductivity [1], for example. This makes it possible to use them in hydrogen fuel cells for energy production. The results of our previous research on gas-proton conductor exchange processes are reported in [2-4].

High temperature proton conducting oxides can be used in a number of applications including hydrogen isotope separation devices, fuel cells, hydrogen sensors and others [5]. Of prominence has been the discovery of fast proton conduction in the Ba and Sr cerate perovskites at modest temperatures (<700^{o}C). Several issues have been reported with these materials, such as their instability in CO_2 containing atmospheres [6,7]. However, through further substitution with Zr, for instance, higher performance materials can been produced. In this paper we report recent progress in the investigation of the influence of reactor irradiation on the structure and properties of both barium and strontium cerates.

2. EXPERIMENTAL

Samples of $BaCeO_3$ and $SrCeO_3$ doped with neodymium and yttrium were fabricated by solid-state reaction and inductive melting technologes. After synthesis, the samples were annealed in air at 650^{o}C. Samples were then sealed in ampoules and were irradiated at 100 and 620^{o}C in ‘wet’ and ‘dry’ channels of the WWR-K reactor of the Institute of Nuclear Physics RK to achieve different total doses. The neutron flux during irradiation was ~3×10^{13} n/cm^{2}c. After irradiation some samples were annealed in laboratory conditions at 620^{o}C. Gas thermodesorption and X ray analysis were used to characterise these materials.

The experimental setup used for gas thermodesorption studies is depicted schematically in Fig. 1. This setup allowed the partial pressure of gases in the working chamber to be measured during heating at a known ramp rate. To achieve an acceptable vacuum (~10^{-5} Pa) the entire vacuum system, including the vacuum chamber was heated prior to the experimental programme. During the system bake-out, samples were placed in a cooler part of the chamber which was maintained at approximately 30^{o}C by circulating cooling water through the vessel. The temperature of the samples was measured using a W-Re thermocouple placed next to the sample position The samples (up to a total of 7) were successively placed in the heating device and thermodesorption spectrums of the gases of interest were measured.

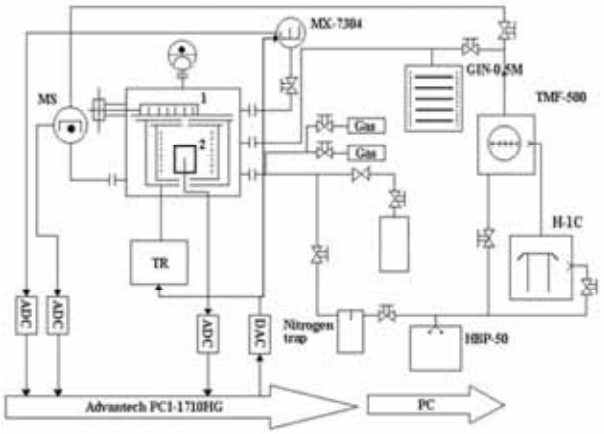

FIG. 1.Schematic of the device used for gas thermodesorption measurments: 1 - cell for samples; 2 – heater; MX-7304 – radio frequency mass-spectrometer; MS – static mass-spectrometer; TR – high current temperature regulator; PC – personal computer.

A personal computer with an Advantech PCI-1710HG module was used to select and control sample heating, choice of gas masses to be monitored, temperature and thermodesorption spectrum measurement. This automation scheme allows up to 6 desorption spectra of different gases to be measured simultaneously. The samples heating rate was 42 K/min in all cases. X ray powder diffraction data were collected from irradiated and initial samples using a Bruker 'D8 advance' diffractometer.

3. RESULTS

Spectra of oxygen and water molecule release from Nd-doped barium cerate samples irradiated in the reactor to different doses at 100°C are shown in Fig.s 2. It can be seen that additional intercalation of water and oxygen molecules takes place after sample irradiation and the amount of desorbed gases increases with irradiation dose. This can be explained by defect formation during irradiation, which can serve as additional centers of gas intercalation in the oxides.

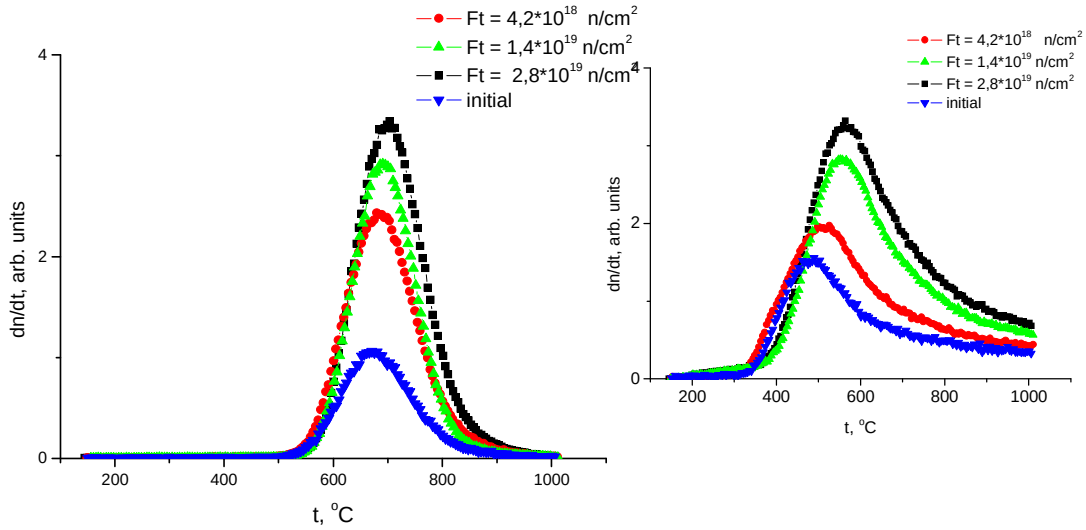

FIG. 2. Dose dependence of (a) O_2 desorption and (b) H_2O desorption from ceramic $BaCe_{0.9}Nd_{0.1}O_{3-\delta}$.

Previous work has shown that oxygen desorption of barium cerates is described by second order kinetics, no oxygen is released from the undoped samples and the amount of desorbed oxygen increases with doping level [2]. This suggests that doping increases the oxygen vacancy concentration and this leads to mobile oxygen that is easily desorbed, suggesting thatstructural defects are responsible for desorption processes from barium cerates. Effect of irradiation dose on the oxygen desorption process is similar to the effect of sample doping level therefore it is concluded that structural defects generated during irradiation are responsible for additional intercalation of oxygen and water molecules in these oxides.

A significant increase in carbon dioxide content in these samples was also observed with increasing irradiation dose in Fig. 3. These results confirm previous work [8] that indicated that barium cerate can interact with carbon oxides resulting in the formation of $BaCO_3$. Since the presence of any $BaCO_3$ impurities in these materials leads to a deterioration of the oxide (stability and conductivity), it is necessary to avoid contact of cerates with carbon oxides, including during reactor irradiation.

Investigation of the low temperature irradiation effect on both strontium and barium cerates is interesting to aid in the understanding of gas desorption, but for practical purposes, it is more important to understand the gas desorption of these oxides under irradiation at high temperatures. Therefore, the influence of high temperature reactor irradiation on barium and strontium cerates was also studied.

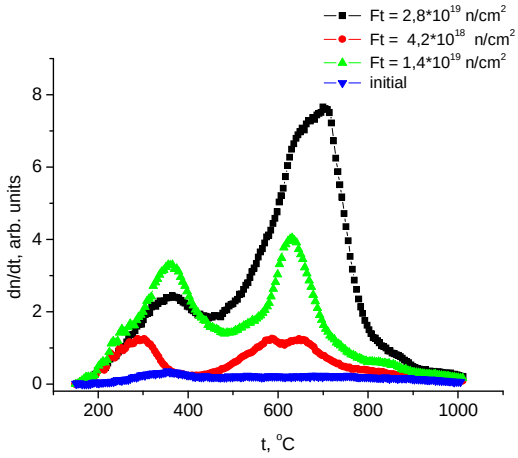

FIG. 3. Dose dependence of CO_2 desorption from ceramic $BaCe_{0.9}Nd_{0.1}O_{3-\delta}$.

It was found that high temperature reactor irradiation (620°C), in contrast to low temperature irradiation, results in both quantitative and qualitative changes in the gas thermodesorption spectra from barium and strontium cerates. The quantity of oxygen molecules released from the samples irradiated at 620°C is significantly higher than observed at low temperature (100°C). An additional sharp oxygen desorption peak appeared at 540°C which disappears after the samples were post irradiation annealed in laboratory conditions in air at 620°C in Fig. 4.

An additional shoulder in the water molecule desorption spectrum shown in Fig. 5 was observed to coincide with the temperature of the sharp oxygen peak, 540°C. This shoulder in the water desorption spectrum was not observed in the initial samples or in the samples annealed in laboratory conditions at 620°C after irradiation.

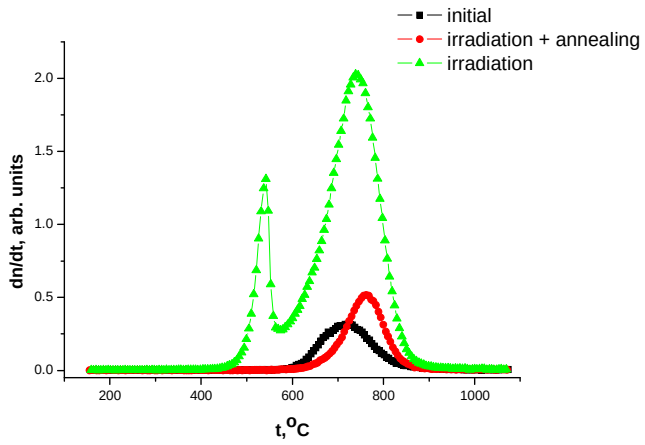

FIG. 4. O_2 desorption from $BaCe_{0.9}Nd_{0.1}O_{3-\delta}$ samples. (t_{irr} ~ 620°C, Ft=7.6×10^{18} n/cm^2) highlighting changes in the desoroption with post irradiation annealing.

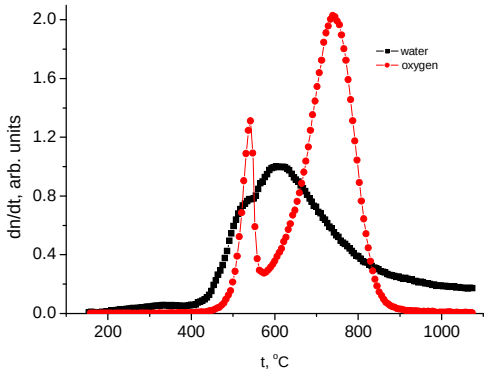

FIG. 5. Oxygen and water molecule release from $BaCe_{0.9}Nd_{0.1}O_{3-\delta}$ samples (tirr ~ 620 °C, Ft=7.6×10^{18} n/cm^2).

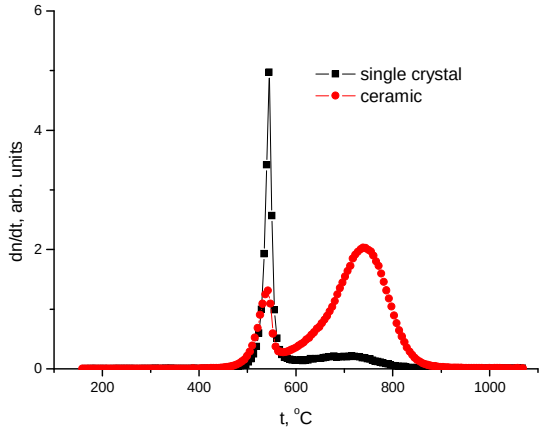

FIG. 6. Oxygen molecule release from polycrystalline and single crystal $BaCe_{0.9}Nd_{0.1}O_{3-\delta}$ samples. (t_{irr} ~ 620°C, Ft=7.6×10^{18} n/cm^2).

The intensity of the sharp oxygen peak observed at 540°C in samples fabricated by the inductive melting method (single crystals) was significantly higher than in samples synthesized by solid-state reaction as shown in Fig. 6. The shape of the oxygen desorption peak, together with changes in the desorption spectra of water, indicate that a phase transformation takes place in the samples during heating.

By contrast here was no evidence for oxygen release from either the doped or undoped strontium cerate samples after annealing in different oxidizing-reducing conditions or after low temperature reactor irradiation. A sharp peak of in the oxygen release spectrum was also observed after reactor irradiation of strontium cerates at 620°C see Fig. 7.

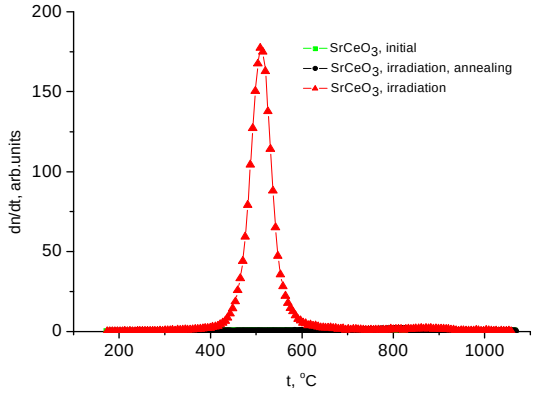

FIG. 7. Oxygen molecule release from $SrCe_{0.95}Y_{0.05}O_{3-\delta}$ samples (t_{irr} ~ 620°C, $Ft=7.6\times10^{18}$ n/cm^2).

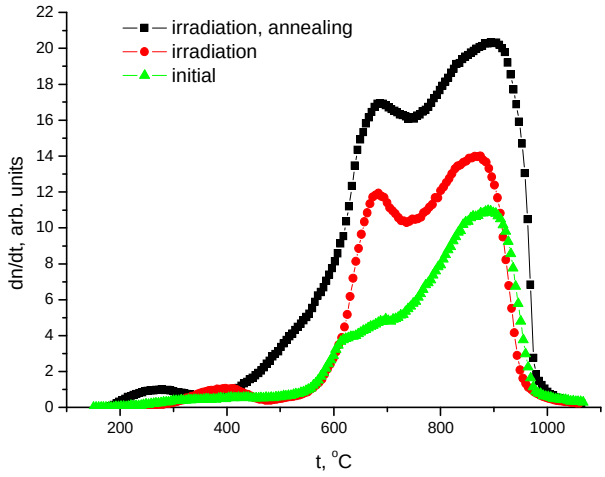

FIG. 8. Carbon dioxide molecule release from $BaCe_{0.9}Nd_{0.1}O_{3-\delta}$ samples. (t_{irr} ~ 620°C, $Ft=7.6\times10^{18}$ n/cm^2).

X ray analysis of the cerates, reported elsewhere, has confirmed our suggestion of phase transformation in the samples during heating. It appears that partial disordering in the lattice of the oxides irradiated at high temperatures occurred. Annealing of the oxides under laboratory conditions, after irradiation, re-orders the structure and is accompanied by crystallization of a secondary CeO_2 phase. This phase transformation is likely to be the origin of the sharp peak observed in the oxygen molecule desorption spectra.

High temperature reactor irradiation also results in an increase of the carbon dioxide signal originating from the desorption from these oxides. Annealing of the irradiated samples results in a further increase of the CO_2 released by these samples (Fig. 8).

4. CONCLUSIONS

Using an irradiation technique it has been demonstrated that the release of oxygen and of CO_2 from both Ba and Sr cerates is a dose and temperature dependent process. We suggest that the irradiation at higher temperatures and doses causes a partial disordering of the crystal lattice. With further reannealing the crystalline nature of the phase is recovered. Significantly differences between the Sr and Ba cerates were observed, indicating that at low temperatures oxygen realease is not observed from the cerate samples. Further studies to probe these phenomena are under way.

REFERENCES

[1] IWAHARA, H., UCHIDA, H., TANAKA, S., Appl. Electrochem. **16** (1986) 663-668.
[2] AKSENOVA, T.I., et al., Solid State Ionics **162-163** (2003) 31-36.
[3] KHROMUSHIN, I.V., AKSENOVA, T.I., ZHOTABAEV, ZH.R., Solid State Ionics **162-163**(2003) 37-40.
[4] BAIKOV, YU.M., Ionics **9** (2003) 1-9.
[5] SHOBER, T., Ionics **9** (2003) 1-9.
[5] SHOBER, T., Solid State Ionics **162-163** (2003) 277-281.
[6] KREUER, K.D., Annu. Rev. Mater. Res., **33** (2003) 333-359
[7] XIE, K., YAN, R., LIU, X., J. Alloys Compounds 479 (2009) 36-39.
[8] RYU, K.H., HAILE, S.M., Solid State Ionics, **125** (1999) 355-367.

LIST OF PARTICIPANTS

Soraia Pirfo BARROSO	KFKI Atomic Energy Research Institute (AEKI) Fuel and Reactor Materials Department 1121 Budapest Hungary sbarroso@aeki.kfki.hu
Pascal BERGER	CEA/CNRS Laboratoire Pierre SÜE/CEA-SACLAY GIF sur Yvette F-91191 France pascal.berger@cea.fr
Roberto COPPOLA	ENEA-Casaccia FPN-FISNUC CP 2400 00100 Rome Italy roberto.coppola@enea.it
Horacio CORTI	Centro Atómico Constituyentes, Comisión Nacional de Energía Atómica (CNEA) Buenos Aires Argentina hrcorti@cnea.gocv.ar
Francesco DOLCI	Institut of Energy Joint Researche Centre Petten The Netherlands francesco.dolci@ec.europa.eu
Helmut W. FRITZSCHE	National Research Council Canada Chalk River Laboratories building 459 P.O. Box: station 18 Chalk River K0J 1J0 Canada helmut.fritzsche@nrc.gc.ca
Bjorn C. HAUBACK	Institute for Energy Technology Instituttveien 18 P.O. Box: P.O. Box 40 Kjeller No-2027 Norway bjorn.hauback@ife.no

Jacques HUOT
Université du Québec à Trois-Rivières
3351 des Forges
Trois-Rivières G9A 5H7
Quebec
Canada
jacques.huot@uqtr.ca

Igor KHROMUSHIN
National Nuclear Center of Kazakhstan Republic
Ibragimov St. 1,
050032 Almaty
Kazakhstan
khromushin@mail.ru

Sabrina SARTORI
Institute for Energy Technology
Instituttveien 18
P.O. Box: P.O. Box 40
Kjeller NO-2027
Norway
sabrinas@ife.no

Zdravko SIKETIC
Ruder Boskovic Institute
Zagreb 10000
P. O. Box 180
Croatia
zsiketic@irb.hr

Stephen SKINNER
Imperial College
Exhibition Road
London
UK
s.skinner@imperial.ac.uk

Marc STEEN
Clean Energy Unit
Institut of Energy
Joint Researche Centre
Petten
The Netherlands
marc.steen@ec.europa.eu

Eveline WEIDNER
JRC
Westerduinweg 3
Petten 1755 LE
The Netherlands
eveline.weidner-ronnefeld@ec.europa.eu

Ye YIMING
China Institute of Atomic Energy
Beijing
China
yym@ciae.ac.cn

Alexez ZOLOTARENKO
I.M. Frantsevich
Institute for Problems of Materials Sciences of NASU
Kiev - 142
Ukraine
lab67@ipms.kiev.ua

Marco ZOPPI
CNR-Istituto Sistemi Complessi
Via Madonna del Piano, 10
Sesto Fiorentino 50019
Italy
marco.zoppi@isc.cnr.it

IAEA
International Atomic Energy Agency

Where to order IAEA publications

In the following countries IAEA publications may be purchased from the sources listed below, or from major local booksellers. Payment may be made in local currency or with UNESCO coupons.

AUSTRALIA
DA Information Services, 648 Whitehorse Road, MITCHAM 3132
Telephone: +61 3 9210 7777 • Fax: +61 3 9210 7788
Email: service@dadirect.com.au • Web site: http://www.dadirect.com.au

BELGIUM
Jean de Lannoy, avenue du Roi 202, B-1190 Brussels
Telephone: +32 2 538 43 08 • Fax: +32 2 538 08 41
Email: jean.de.lannoy@infoboard.be • Web site: http://www.jean-de-lannoy.be

CANADA
Bernan Associates, 4501 Forbes Blvd, Suite 200, Lanham, MD 20706-4346, USA
Telephone: 1-800-865-3457 • Fax: 1-800-865-3450
Email: customercare@bernan.com • Web site: http://www.bernan.com

Renouf Publishing Company Ltd., 1-5369 Canotek Rd., Ottawa, Ontario, K1J 9J3
Telephone: +613 745 2665 • Fax: +613 745 7660
Email: order.dept@renoufbooks.com • Web site: http://www.renoufbooks.com

CHINA
IAEA Publications in Chinese: China Nuclear Energy Industry Corporation, Translation Section, P.O. Box 2103, Beijing

CZECH REPUBLIC
Suweco CZ, S.R.O., Klecakova 347, 180 21 Praha 9
Telephone: +420 26603 5364 • Fax: +420 28482 1646
Email: nakup@suweco.cz • Web site: http://www.suweco.cz

FINLAND
Akateeminen Kirjakauppa, PO BOX 128 (Keskuskatu 1), FIN-00101 Helsinki
Telephone: +358 9 121 41 • Fax: +358 9 121 4450
Email: akatilaus@akateeminen.com • Web site: http://www.akateeminen.com

FRANCE
Form-Edit, 5, rue Janssen, P.O. Box 25, F-75921 Paris Cedex 19
Telephone: +33 1 42 01 49 49 • Fax: +33 1 42 01 90 90
Email: formedit@formedit.fr • Web site: http://www. formedit.fr

Lavoisier SAS, 145 rue de Provigny, 94236 Cachan Cedex
Telephone: + 33 1 47 40 67 02 • Fax +33 1 47 40 67 02
Email: romuald.verrier@lavoisier.fr • Web site: http://www.lavoisier.fr

GERMANY
UNO-Verlag, Vertriebs- und Verlags GmbH, Am Hofgarten 10, D-53113 Bonn
Telephone: + 49 228 94 90 20 • Fax: +49 228 94 90 20 or +49 228 94 90 222
Email: bestellung@uno-verlag.de • Web site: http://www.uno-verlag.de

HUNGARY
Librotrade Ltd., Book Import, P.O. Box 126, H-1656 Budapest
Telephone: +36 1 257 7777 • Fax: +36 1 257 7472 • Email: books@librotrade.hu

INDIA
Allied Publishers Group, 1st Floor, Dubash House, 15, J. N. Heredia Marg, Ballard Estate, Mumbai 400 001,
Telephone: +91 22 22617926/27 • Fax: +91 22 22617928
Email: alliedpl@vsnl.com • Web site: http://www.alliedpublishers.com

Bookwell, 2/72, Nirankari Colony, Delhi 110009
Telephone: +91 11 23268786, +91 11 23257264 • Fax: +91 11 23281315
Email: bookwell@vsnl.net

ITALY
Libreria Scientifica Dott. Lucio di Biasio “AEIOU”, Via Coronelli 6, I-20146 Milan
Telephone: +39 02 48 95 45 52 or 48 95 45 62 • Fax: +39 02 48 95 45 48
Email: info@libreriaaeiou.eu • Website: www.libreriaaeiou.eu

JAPAN
Maruzen Company, Ltd., 13-6 Nihonbashi, 3 chome, Chuo-ku, Tokyo 103-0027
Telephone: +81 3 3275 8582 • Fax: +81 3 3275 9072
Email: journal@maruzen.co.jp • Web site: http://www.maruzen.co.jp

REPUBLIC OF KOREA
KINS Inc., Information Business Dept. Samho Bldg. 2nd Floor, 275-1 Yang Jae-dong SeoCho-G, Seoul 137-130
Telephone: +02 589 1740 • Fax: +02 589 1746 • Web site: http://www.kins.re.kr

NETHERLANDS
De Lindeboom Internationale Publicaties B.V., M.A. de Ruyterstraat 20A, NL-7482 BZ Haaksbergen
Telephone: +31 (0) 53 5740004 • Fax: +31 (0) 53 5729296
Email: books@delindeboom.com • Web site: http://www.delindeboom.com

Martinus Nijhoff International, Koraalrood 50, P.O. Box 1853, 2700 CZ Zoetermeer
Telephone: +31 793 684 400 • Fax: +31 793 615 698
Email: info@nijhoff.nl • Web site: http://www.nijhoff.nl

Swets and Zeitlinger b.v., P.O. Box 830, 2160 SZ Lisse
Telephone: +31 252 435 111 • Fax: +31 252 415 888
Email: infoho@swets.nl • Web site: http://www.swets.nl

NEW ZEALAND
DA Information Services, 648 Whitehorse Road, MITCHAM 3132, Australia
Telephone: +61 3 9210 7777 • Fax: +61 3 9210 7788
Email: service@dadirect.com.au • Web site: http://www.dadirect.com.au

SLOVENIA
Cankarjeva Zalozba d.d., Kopitarjeva 2, SI-1512 Ljubljana
Telephone: +386 1 432 31 44 • Fax: +386 1 230 14 35
Email: import.books@cankarjeva-z.si • Web site: http://www.cankarjeva-z.si/uvoz

SPAIN
Díaz de Santos, S.A., c/ Juan Bravo, 3A, E-28006 Madrid
Telephone: +34 91 781 94 80 • Fax: +34 91 575 55 63
Email: compras@diazdesantos.es, carmela@diazdesantos.es, barcelona@diazdesantos.es, julio@diazdesantos.es
Web site: http://www.diazdesantos.es

UNITED KINGDOM
The Stationery Office Ltd, International Sales Agency, PO Box 29, Norwich, NR3 1 GN
Telephone (orders): +44 870 600 5552 • (enquiries): +44 207 873 8372 • Fax: +44 207 873 8203
Email (orders): book.orders@tso.co.uk • (enquiries): book.enquiries@tso.co.uk • Web site: http://www.tso.co.uk

On-line orders
DELTA Int. Book Wholesalers Ltd., 39 Alexandra Road, Addlestone, Surrey, KT15 2PQ
Email: info@profbooks.com • Web site: http://www.profbooks.com

Books on the Environment
Earthprint Ltd., P.O. Box 119, Stevenage SG1 4TP
Telephone: +44 1438748111 • Fax: +44 1438748844
Email: orders@earthprint.com • Web site: http://www.earthprint.com

UNITED NATIONS
Dept. I004, Room DC2-0853, First Avenue at 46th Street, New York, N.Y. 10017, USA
(UN) Telephone: +800 253-9646 or +212 963-8302 • Fax: +212 963-3489
Email: publications@un.org • Web site: http://www.un.org

UNITED STATES OF AMERICA
Bernan Associates, 4501 Forbes Blvd., Suite 200, Lanham, MD 20706-4346
Telephone: 1-800-865-3457 • Fax: 1-800-865-3450
Email: customercare@bernan.com · Web site: http://www.bernan.com

Renouf Publishing Company Ltd., 812 Proctor Ave., Ogdensburg, NY, 13669
Telephone: +888 551 7470 (toll-free) • Fax: +888 568 8546 (toll-free)
Email: order.dept@renoufbooks.com • Web site: http://www.renoufbooks.com

Orders and requests for information may also be addressed directly to:

Marketing and Sales Unit, International Atomic Energy Agency
Vienna International Centre, PO Box 100, 1400 Vienna, Austria
Telephone: +43 1 2600 22529 (or 22530) • Fax: +43 1 2600 29302
Email: sales.publications@iaea.org • Web site: http://www.iaea.org/books

INTERNATIONAL ATOMIC ENERGY AGENCY
VIENNA
ISBN 978–92–0–125410–8
ISSN 1011–4289